2022

Assessing Machine Learning Utility in Predicting Hydrologic and Nitrate Dynamics in Karst Agroecosystems

Timothy McGill

University of Kentucky, timothy.mcgill@uky.edu
Author ORCID Identifier:
 https://orcid.org/0000-0002-6980-5064
Digital Object Identifier: https://doi.org/10.13023/etd.2022.114

Right click to open a feedback form in a new tab to let us know how this document benefits you.

Recommended Citation

Assessing Machine Learning Utility in Predicting Hydrologic and Nitrate Dynamics in
Karst Agroecosystems

_____

THESIS

_____

A thesis submitted in partial fulfillment of the
requirements for the degree of Master of Science in Biosystems and Agricultural
Engineering in the College of Agriculture and Engineering
at the University of Kentucky

By

Timothy McGill

Lexington, Kentucky

Director: Dr. William Ford, Professor of Biosystems and Agricultural Engineering

Lexington, Kentucky

2022

ABSTRACT OF THESIS

Assessing Machine Learning Utility in Predicting Hydrologic and Nitrate Dynamics in
Karst Agroecosystems

Seasonal hypoxia in the Gulf of Mexico and harmful algal blooms experienced in many inland freshwater bodies is partially driven due to excessive nitrogen loading seen from agricultural watersheds. Within the Mississippi/Atchafalaya River Basin, many areas are underlain with karst features, and efforts to reduce nitrogen contributions from these areas have had varying success, due to lacking a complete understanding of nutrient dynamics in karst agricultural systems. To improve the understanding of nitrogen cycling in these systems, 35 months of high resolution in situ water quality and atmospheric data were collected and fed into a two-hidden layer extreme learning machine (TELM) to predict discharge and nitrate exports from a karst agroecosystem in the Inner Bluegrass region, to improve the understanding of nitrate dynamics in karst and determine the variables of influence driving nitrate loading in karst systems. Including atmospheric and soil moisture and temperature records to 100 cm in modeling resulted in the TELM providing accurate estimates of both nitrate concentration and flowrate (NSE=0.9328 and NSE=0.9363 respectively) and represented short term storm event hysteresis and diurnal signals in model predictions. The TELM also showed the variables most influential in training were the soil moisture and temperature parameters levels, pointing to the importance of focusing future work on understanding how temperature influences matrix-macropore interactions in the temperate karst environment. Finally, the ELM showed the fertilizer application data was not influential in model training, indicating that, at this study site, the fertilizer application has little control over nitrate loading. This should be studied further in other landscapes with higher rates of fertilizer application where alternative hysteretic patterns have been observed.

KEYWORDS: karst agroecosystem, nitrate dynamics, machine learning, water resources

Timothy McGill

01/25/2022

Assessing Machine Learning Utility in Predicting Hydrologic and Nitrate Dynamics in
Karst Agroecosystems

By

Timothy Andrew McGill, Jr

Dr. William Ford
Director of Thesis

Dr. Donald Colliver
Director of Graduate Studies

01/25/2022
Date

ACKNOWLEDGMENTS

TABLE OF CONTENTS

LIST OF TABLES

LIST OF FIGURES

CHAPTER 1. **INTRODUCTION**

1.1   Overview and Research Need

Karst regions cover an estimated 7-10% of the Earth's land surface and are a drinking water source for 25% of the world's inhabitants (Ford, 1989). Karst landscapes are widely used for agricultural production across the world (van Beynen, 2011). In the United States, 18% of landscapes are underlain by soluble rocks having karst or the potential for the development of karst features. Food-producing states underlain with these features include Kentucky, Tennessee, Nebraska, Kansas, Mississippi, Wisconsin, and several other states that lie within the Mississippi/Atchafalaya River Basin (MARB) (Robertson & Saad, 2021; Weary & Doctor, 2014). Further, it is estimated 60 to 73% of the total nitrogen contributed to the MARB results from agricultural practices, specifically fertilizers, manure, and fixation, with much of this ending up in the Gulf of Mexico (Robertson & Saad, 2021). These contributions result in eutrophication of aquatic systems and can lead to toxic algal blooms and hypoxic (dead) zones. This problem is not isolated to the Gulf of Mexico, as there have been over 400 dead zones recorded globally, although the Gulf of Mexico is consistently one of the largest (NAE, 2017; NOAA, 2021).

There is widespread recognition that fertilization practices impact the concentration and loading of nitrate in karst agroecosystems. In cultivated landscapes, the use of industrially produced inorganic fertilizers have increased in recent years to meet food production needs (Robert & Rutger, 2008). Studies have shown strong increases in nitrate concentrations in subsurface drainage following inorganic fertilizer application (e.g., Ford et al., 2018). Additionally, organic sources, such as livestock

1

waste, are also major contributors to NO_3^- leaching to groundwater, with several studies showing a direct link between livestock operations and elevated nitrate concentrations in groundwater seeps and conduits (Boyer & Pasquarell, 1996). This buildup of nitrate has been shown to create legacy effects, where decomposition of the manure is delayed, slowly releasing nitrate. These legacy sources can deliver high nitrate concentrations for many years after application, especially when applied at a regular schedule (Basu et al., 2012; Johnson & Stets, 2020). Timing, magnitude, and extent of organic and inorganic fertilizer applications make assessments of nitrate loadings a challenge at the watershed-scale.

Assessments of nitrate loading in karst systems is complicated by karst's heterogeneous structure, unique flow pathways, and in-stream processes. Karst systems are often characterized as a set of vertical zones, where the soil may retain much of the applied nitrate and release it to diffuse or concentrated flow paths within the epikarst and conduits following rain events (Opsal, 2017; Husic, 2019). This retention and release makes determining nitrate loading difficult in karst because it is highly variable depending on flow path activation, which can vary drastically based on time of year, weather patterns, and the structure of the karst system being study. Many studies characterizing karst systems as zones do not recognize the vertical variability seen in the soil matrix, particularly in soil moisture levels, which may have a substantial impact in exports due to the karst features that connect subsurface layers. Further in-stream process downstream of springs and seeps are hotspots for biochemical activity and thus strongly alter nitrate concentrations at the watershed-scale (Ford et al., 2019).

With the improvements in high resolution in situ sensing capabilities, water quality monitoring now results in extensive datasets for analysis. This influx of big data requires improved analysis procedures such as machine learning to create predictive models. Conventional information retrieval and processing methods typically require vast amounts of human labor and expertise because they require tuning and adjusting of the parameters on a case-by-case basis. Machine learning solves some of these issues by providing researchers the ability to leverage computational advancements to elucidate patterns in data and identify correlations that may otherwise go unnoticed (Shen, 2018). Several studies in environmental and watershed science have employed machine learning techniques to improve modeling and forecasting with promising results (Prasad, 2018; Shen, 2018; Fijani, 2019; Wen, 2019) with others calling for increased implementation of the technology in hydrologic and environmental studies (Lary, 2016; Shen, 2018; Moreido, 2021). Few studies to our knowledge use machine learning approaches for water quality assessments in karst agroecosystems, despite the recognized importance of these landscapes.

1.2   Objectives

The overarching objective of this study was to improve understanding of ag fertilization practices and soil hydrologic connectivity on nitrate concentration and loading dynamics in karst agroecosystems. To meet the overarching objective, the specific objectives of this thesis were to:

1. Collect and analyze a novel high-frequency database of surface water nitrate concentrations in a karst agricultural watershed to model governing dynamics.

2. Assess the utility of machine learning to predict flowrate and nitrate concentrations in the karst agroecosystem and determine the relative importance of atmospheric, soil moisture and temperature, and agricultural fertilization practices on nitrate concentrations.

3. Assess the utility of machine learning models to account for hysteresis and in-stream processes impacting nitrate concentrations in watersheds.

1.3   Thesis Contents

Chapter 1: Introduction. Provides an overview of the importance of nitrate loading from karst agroecosystems to regional water quality problems in the MRB, identifies the objectives and defines the contents of this thesis.

Chapter 2: Literature Review. Provides a review of karst hydrology, soil nitrate dynamics in karst, and big data applications in karst.

Chapter 3: Methodology. Outlines methodology for the data collection and analysis, and analytical methodologies to address the objectives of this thesis.

Chapter 4: Results and Discussion. Details the results of the high-frequency dataset, machine learning model performance and evaluation, and nitrate loading analysis results. The utility of machine learning to predict nitrate and flow in heterogenous karst agroecosystems, the impacts of perceived important environmental factors, and implications for management are discussed.

Chapter 5: Conclusions and Future Work. Summarizes the major findings of this thesis and highlights future research needs.

Chapter 6: References Cited. Lists the details of works cited in this thesis.

CHAPTER 2.   **LITERATURE REVIEW**

2.1   Karst Hydrological Processes

Karst topography is characterized by an expansive underground drainage network that includes caves, sinkholes, and other cracks and fissures in subsurface rocks. This type of topography is often found in areas with limestone, dolomite, or gypsum bedrocks and is formed through a process of dissolution, or karstification. Karstification creates heterogeneity within the subsurface through selective dissolution that initially develops at discontinuities, fractures, joints, bedding planes or macropores within the bed (Bakalowicz, 2005). As the process advances these small imperfections in the bedrock develop into fissures and fractures which develop into larger conduits. Based on dissolution mechanics for calcite, the karstification process shows positive feedback, creating a hierarchical organizational structure analogous to fluvial systems (Bakalowicz, 2005; Hartmann et al., 2014). This structure creates an interconnectedness between hydrologic zones that gives karst its unique hydrologic properties.

The hydrologic regions of karst watersheds can be characterized by three main zones; the soil, epikarst, and phreatic, which have been conceptualized as distinct reservoirs differentiated by the groundwater's residence time and behavior within the zone (Bakalowicz, 2005; Hartmann et al., 2014; Husic et al., 2019). The soil is the topmost layer of the subsurface and acts as a large reservoir for storage and transmission during rain events, releasing the entrained water into the epikarst, adjacent quick flow pathways, and through evapotranspiration (Husic et al., 2019). The epikarst, also known as the skin of karst, is the uppermost region of the karst network and can begin at either the land surface or from the soil bedrock interface, extending downward for several to

tens of meters (Jones, 2013). Several studies have determined stored water within the epikarst is pushed out and replaced by newer water during storm events, showing the large storage and transfer potential the epikarst maintains (Buda & DeWalle, 2009; Jones, 2013). The phreatic zone is characterized as the area below the vadose zone and is always saturated and in karst landscapes is often comprised of well-developed conduits with a high hydraulic conductivity (Bakalowicz, 2005). These conduits do not act as storage for the watershed, but instead transfer the groundwater to large regional aquifers or local tributaries (Reed et al., 2010).

Hydrologic pathway dynamics in karst watersheds heavily influence movement of contaminants to subsurface springs and seeps. Flow pathways are often discretized into quick, intermediate, and slow flow pathways (Hartmann et al., 2014; Husic et al., 2019). The quick flow pathways reflect rapid connectivity water sources to surface and subsurface pathways, primarily *via* overland flow, or sinkholes and swallets that are directly connected to subsurface conduits in the epikarst and phreatic zones (Hartmann et al., 2014; White, 2002). Many karst systems experience much of their groundwater recharge through intermediate and slow flow pathways, with some systems estimated at over 80% (Husic et al., 2019). The intermediate flow paths reflect transport through vertical conduits and fractures in the epikarst which transmit water deeper into the phreatic zone during high flow conditions, while tertiary or less developed flow paths act as a bottleneck for infiltrating water, slowing and retaining water, or moving it laterally through the epikarst. The slow flow pathways exist within the micropores in the soil and very small diffuse fissures and cracks in the epikarst, and their dynamics are heavily dependent on the conditions experienced above ground, typically draining into the more

developed karst network following heavy rains (Aquilina et al., 2006). This dynamic relationship between the karst features and the soil matrix emphasizes the impact soil process have in karst hydrology.

Soil water stored in the vadose zone prior to storm events may become connected to surface waters through preferential flow pathways activated at variable depths in the soil profile or reconnection of perched aquifers deeper in the vadose zone. Preferential flows are often associated with flow through macropores created by earthworm borrows, root penetration, and fingering paths which often do not penetrate through the complete soil column into the subsoil, resulting in variable activation within the soil profile. Klaus and McDonnell (2013) showed new infiltrating water enters through macropores and disperses into the matrix, which results in new water mixing with the old, stored water, and once the soil reaches saturation the mixed water is mobilized and pushed deeper into the soil through preferential flow paths. The authors found that the soil layer from 0.2 to 0.4 m was found to account for much of the flow contributing to the preferential flow paths, due to the extensive earthworm channels at their tile-drained study site. Others have also highlighted the role of macropores in driving recharge of matrix water before saturation is reached, at which point the macropores act like fissures and cracks, channeling infiltrating water to surface streams or into karst fissures and conduits (Chen et al., 2021; Germer & Braun, 2015). Further, if conditions remain dry for extended periods, perched aquifers within the vadose zone may become isolated until the water table returns to an elevated state (Williams, 1983). Some studies show that only in high soil saturation conditions within the vadose zone, when the karst system network of fissures and cracks are hydraulically connected, will you see the mobilization of

entrained water (Kogovšek & Petrič, 2012; Klaus et al., 2013; Wang et al., 2018). Cumulatively, these studies illustrate a need to account for soil moisture variability both spatially and temporally to accurately predict karst discharge and flow pathway dynamics.

Given the complexities of karst hydrology, numerical models are often utilized to understand system behavior and develop predictive tools, however existing approaches do not account for within-profile soil moisture variability. In many hydrologic models of karst systems, the various zones (soil matrix, epikarst, phreatic zone, and quick flow paths) are treated as reservoirs, each with their own storage and contribution characteristics (Tzoraki & Nikolaidis, 2007; Husic et al., 2019). These types of models have been shown to accurately reflect multiple pathways (Fleury et al., 2007; Tritz et al., 2011), however, concerns regarding model suitability and equifinality have been raised, requiring more rigorous evaluation of the model's process-representation capability (Hartmann et al., 2013, 2017; Hartmann, 2017). Husic et al., 2019 showed the lumped reservoir model was effective at elucidating complex pathways, processes, and timing of nitrogen in karst systems, although they also pointed to the relative dominance of the slow flow paths in karst being an underdeveloped topic in water science. This is evident because these lumped reservoir models tend to treat the soil matrix as a single reservoir or combine it with the epikarst rather than isolating different depths of the soil matrix to elucidate the effects different layers of the soil profile have on nitrate exports and loading. Due to the role the soil plays in the attenuation of contaminant transport into groundwater (Russo et al., 2013), this lack of recognition on the impacts of variable soil

conditions in the model parameters may be a weakness of lumped reservoir models and is an ongoing research need.

2.2   Nitrate dynamics in Karst Agroecosystems

Studies of nitrate dynamics in karst landscapes have shown recurring trends regarding flow pathways and hydrologic zone connectivity. During storm events, studies investigating nitrate concentrations in karst landscapes have found a dilution effect during peak flow, which coincides with precipitation waters that are transported through quick flow pathways (Baran et al., 2008; Buda & DeWalle, 2009; Ford et al., 2019; Husic et al., 2019). Following quickflow of precipitation waters, epikarst and soil drainage waters become connected through quick and intermediate flow paths, resulting in peak event nitrate concentrations (Husic et al., 2019). Later in the event, recession of soil and epikarst zones and increases in phreatic contributions result in more moderate nitrate concentrations, given that nitrate concentration of the phreatic base flow has been observed to fall between the diluted event dominated flow and the high concentration soil matrix waters (Ford et al., 2019; Rusjan et al., 2008). To illustrate the impact of this conceptual model on nitrate loading, results from Husic et al. (2019) estimated quickflow accounted for 19% of total water contribution while only exporting 11% of total nitrate, intermediate flow (soil and epikarst) accounted for 42% of total water and 49% of total nitrate, and the phreatic pathway accounted for 39% of exported water while accounting for 40% of exported nitrate.

Deviations from the conceptual model are likely in fertilized agroecosystems, particularly for the quickflow pathway in systems with commercial fertilizer applications. Inorganic industrial fertilizers are engineered to have high water solubility to promote

9

availability to the crops/vegetation, especially nitrogenous fertilizers. Due to this high water solubility, nitrate fertilizers can easily be transported by runoff or infiltration resulting in shallow and/or karst aquifers being contaminated with excess levels of nitrate (Robertson and Saad, 2021; Zhang et al., 2020: Katz, 2019; Buda and DeWalle, 2009; Zhu, 2009; Alexander et al., 2008). Livestock and animal husbandry operations may impact nitrate leaching as elevated nitrate concentrations have been detected in groundwater due to runoff from fields, paddocks, and housing structures during heavy rains (Boyer & Pasquarell, 1995). Slurries and manure are often spread across pastures to add nutrients to ensure a healthy food source for grazing animals as well as controlling waste buildup (van Beynen, 2011). Organic fertilizer must be broken down by soil microbes, through a process called mineralization, which has been shown to reduce build-up of nitrate when compared to inorganic sources (Zhang et al., 2012; Meng et al., 2005). Despite their slower release times, organic fertilizers can still elevate nitrate levels in surface and groundwater beyond safe and approved levels (Yang et al., 2017; Meng et al., 2005).

Soil hydrologic and biochemical processes have been found to cause temporal variability in nitrate concentrations of drainage waters in karst agroecosystems. Coupled evapotranspiration and mineralization of soil organic matter has been found to increase soil nitrate in between flushing events, leading to peak concentrations and loadings during wet seasons. For instance, these seasonal variations were observed in karst and non-karst agroecosystems in China (Yang et al., 2017; Yue et al., 2019), the Lake Erie basin (Tian et al., 2015), in Rhode Island and Vermont (Seybold et al., 2019), in southern Portugal (Yevenes and Mannaerts, 2011), and across the Mississippi River Basin (Donner

et al., 2004). These observations suggest soil moisture and biochemical processes are important for nitrate loading; however, we find few studies in these environments have directly assessed the impact of vertical variability in soil moisture dynamics on nitrate concentrations and loadings. Nevertheless, studies have demonstrated asymmetric profiles of nitrate concentrations at varying depths in the soil columns (Igbal and Krothe, 1994; Green et al., 2018), suggesting variable connectivity of soil layers within storm events will significantly impact drainage water concentrations and loadings.

Complex in-stream processes can also greatly impact the nitrate concentration and loading from a watershed. Dissolved inorganic nitrogen can be removed by aquatic vegetation such as algae and duckweed (Bunnell et al., 2020). Dissolved inorganic N may also be released back into surface waters when biota decompose (Korner & Vermaat, 1998; Peterson et al., 1997; Webster et al., 2003). These pools of detrital organic matter facilitate growth of heterotrophic bacteria communities that can transform nitrogen through nitrification and denitrification. Denitrification is an anaerobic process that has been seen to occur in these low-oxygen vegetative biomass pools, while the aerobic nitrification process can also occur at the boundaries of the biomass pools, being stimulated by turbulent advection and diffusion of oxygen (Korner & Vermaat, 1998; Eriksson, 2001; Arango & Tank, 2008). Hydrologic variables, such as flow rate, also impact nitrogen cycling through scour and vegetation washout, as well as conditions around the stream such as canopy cover (Park & Clough, 2012; Griffiths et al., 2013; Ford et al., 2017). Seasonal changes have also been shown to greatly reduce loading, particularly during summer, due to changes in nutrient uptake and flow conditions (Ford et al., 2019). Collectively, previous research has demonstrated the importance of

considering ag fertilization practices, soil profile connectivity variability, and in-stream processes on fluvial nitrate concentrations in drainage waters of karst agroecosystems. Models are needed that consider temporal gradients spanning these governing processes.

2.3   Big data applications for hydrologic and water quality studies

2.3.1   High-frequency sensing

Advances in sensing technology over the last few decades have enabled collection of *in situ* hydrologic and water quality data at higher frequencies, which has improved our understanding of pathways, sources and fate of contaminants in karst environments (Carey et al., 2014; Jensen & Ford, 2019; Pellerin et al., 2013). Precision and accuracy of contemporary *in situ* sensors has allowed researchers to confidently monitor variations in soil temperature and moisture (Bell et al., 2013; Diamond et al., 2013) and water parameters such as conductivity, temperature, and nitrate (Snyder et al., 2018), in addition to long-standing measurements of flowrate.   Many studies have used these sensing platforms to better understand how anthropogenic changes have impacted nitrate cycling in watershed studies (Aubert et al., 2016; Baker & Showers, 2019; Bunnell, 2020; Carey et al., 2014; Hansen & Singh, 2018; Jensen & Ford, 2019; Yang et al., 2020). Blaen et al. (2017) showed the utility of linking hydroclimatological variables with *in-situ* high resolution sensing of nutrients. Another study out of the Houzhai catchment in China used high resolution sensing to create a coupled hydrological-biogeochemical model to understand the sources and pathways for nitrogen within a karst landscape (Zhang et al., 2020). Several studies have also used high-frequency sensing to monitor in-stream processes. Kunz et al. (2016) demonstrated the use of high-frequency sensing in quantifying nitrogen uptake processes in higher order streams. Heffernan et al. (2010)

employed high-frequency nitrate measurements in combination with long-term chemical and hydrologic records and longitudinal sampling to describe spatial and temporal patterns in nitrogen input and removal in a spring fed study site. Burns et al. (2016) leveraged high-frequency data to quantify seasonal variations of diel nitrate loss and compared that to the total in-stream nitrate losses. Collectively studies have demonstrated the utility of high frequency data to provide insights into both upland and in-stream processes.

Concentration-discharge relationships for water quality parameters are now commonly applied to infer sources and pathways of contaminants. Specifically, nitrate hysteresis, or relationships between flow rate and nitrate concentration during and following a rain event, can be used to improve the understanding of source and connectivity dynamics (Liu et al., 2021; Blaen et al., 2017). A quantitative index is now commonly used that compares the normalized flow rate with the normalized constituent concentration during a storm event as they fluctuate overtime due to varying flow path activation (Clare et al., 2019). In many systems the maximum or minimum flow rate and maximum or minimum concentration are experienced at different times during the storm event which, when plotted against each other, creates a C-Q hysteresis loop. These loops, caused by the temporal lags between discharge and concentration, inform the rapidly changing hydrochemical conditions during rain events (Liu et al., 2021; Pellerin et al., 2014). The shape, direction, curvature, and trends of the hysteresis loops can all vary depending on the system, the land use, and the rain event itself. Recent studies have suggested using HI values to evaluate the efficacy of model simulations to represent

flow-concentration dynamics due to the rapid shifts seen during storm events, but is a metric that has rarely been utilized (Liu et al., 2021; Mehdi et al., 2021).

2.3.2   Machine Learning Applications for Hydrology and Water Quality

The large databases generated from high-frequency sensing has brought on a revolution of machine learning applications in hydrologic and water quality modeling, particularly regarding neural network-based approaches. Neural networks employ a network of layers consisting of an input layer, one or multiple hidden layers, and an output layer, each consisting of individual nodes or neurons (Figure 2.1). Each neuron has a weight associated with it and these neurons are connected to neurons in both adjacent layers, with a bias associated with each connection. The bias and weight determine how the neuron affects the next layer and ultimately the learning algorithm output. This structure (Figure 2.1) is modeled after the structure of neurons within the brain and allows the machine learning algorithm to process complex datasets with great efficiency and accuracy (Acharya et al., 2014; Yaseen et al., 2019). One type of machine learning algorithm is the extreme learning machine (ELM). ELMs have been employed in a variety of applications across many sectors to analyze data and generate representative models, due to their ability to achieve similar or better generalization performance, better scalability, and faster learning times than traditional support vector machines (Huang et al., 2012). ELM are used to train feedforward networks, removing the need for iteratively tuning each hidden node as seen in traditional feedforward neural networks (FNN) and support vector machines (SVM), resulting in improved efficiency (Huang et al., 2015).

In recent years, ELMs and other forms of machine learning have been used in several hydrologic and water quality studies (Tables and Figures

14

Table 2.1). Barzegar et al. (2018) demonstrated ELMs and adaptive neuro-fuzzy inference systems (ANFIS) can produce accurate groundwater risk maps with better performance than both M5 Tree and MARS models. Although the standard ELM performed poorly in predicting electrical conductivity (EC) due to the time-lag seen in the study system, a variant called a wavelet-extreme learning machine was able to account for the time-lag and produced an accurate forecast of EC. Heddam et al. (2017) used an extreme learning machine with a sigmoid activation function (S-ELM), ELM with radial based activation function (R-ELM), online sequential ELM (OS-ELM), and optimally pruned ELM (OP-ELM) to predict dissolved oxygen (DO) based on other water quality parameters and compared the results with those from a multiple linear regression (MLR) model and a multilayer perceptron neural network (MLPNN). The results showed all versions of the ELM outperformed the MLR and MLPNN, with the best results generated by the S-ELM, when using all water quality parameters as predictors. Ravinesh et al. (2016) produced an ELM used to predict monthly streamflow in three rivers in Queensland, Australia using hydrometeorological data, climate indices, and sea surface temperature and compared the results to those produced by a standard artificial neural network (ANN). The ELM provided better performance for all three rivers and required less manual preparation than the ANN. Prasad et al. (2018) employed an ELM and variations to predict soil moisture based on solar radiation, precipitation, minimum and maximum daily temperatures, and continental parameter maps such as soil characteristics and seasonal vegetative growth. They found an ELM integrated with ensemble empirical mode decomposition (EEMD-ELM) was highly efficient with great performance when forecasting both upper- and lower-layer soil moisture. More examples

15

of ELMs and other machine learning applications in hydrologic and water quality studies have been summarized in Tables and Figures

Table 2.1. As evidenced from this review, the use of machine learning in nitrate concentration and loading predictions at a watershed scale are lacking; however, collectively the referenced studies show the effectiveness of machine learning in processing large datasets in environmental studies, and have demonstrated, coupled with appropriate input data and processing, that they can also effectively model source and in-stream contaminant dynamics.

A common issue seen when implementing machine learning is overfitting. Overfitting can occur when the algorithm has a small training dataset or there are too many inputs included in the training set (Ying, 2019). When the dataset is too small, the noise has a high probability of being trained into the model and later being used to generate predictions. This can be mitigated by having a large enough dataset to represent a wide variety of conditions experienced within the study system. With a large number of inputs in training, model complexity is increased, and noise can be built into the model due to redundancy present with excess input parameters (Chen et al., 2020). Reducing the number of input variables by removing those that are redundant or are unimportant in training, known as pruning, can effectively reduce overfitting. This can either be done in practice by comparing a range of models having different numbers of hidden units or starting with a large network and pruning out the least significant connections, either by removing individual weights or removing complete units (Bishop, 1995). Several studies have tested methods of pruning, successfully demonstrating effectiveness at preventing

16

overfitting (Bishop, 1995; Chen et al., 2020; Hinton et al., 2012; Lai et al., 2020; Miche et al., 2011; Ying, 2020).

2.4   Tables and Figures

Table 2.1: Literature review of hydrologic and water quality studies implementing machine learning approaches.

Study	Study Location/ Site Description	Landscape	Application	Machine Learning Approaches	Major Findings
Heddam and Kisi, 2017	USA; 8 different river systems	1 Clackamas Basin, OR; 1 Willamette Basin, OR; 2 Umpqua Basin, OR; 2 Tualatin Basin, OR; 1 Delaware basin, NJ; 1 Cumberland Basin, TN; mostly non-karst	Water Quality; modeled Dissolved Oxygen in 8 river systems using water temp, specific conductance, turbidity, and pH	S-ELM, R-ELM, OS-ELM, OP-ELM	S-ELM had best performance, with every ELM outperforming the MLPNN and MLR
Barzegar et al, 2017	Aji-Chay River, Northwestern Iran	Iran's East Azerbaijan province; mostly non-karst	Water Quality; electrical conductivity (EC)	ELM, WA-ELM, ANFIS, WA-ANFIS	Demonstrated ELM and ANFIS models had low performance when forecasting EC but the boosted WA-ELM and WA-ANFIS performed well to account for time-lag
Barzegar et al, 2018	East Azerbaijan, Iran	Marand plain to the west of the Caspian Sea; non-karst basin with three aquifer system in the plain area	Water Quality; construct reliable and accurate groundwater risk maps to provide strategic measures for the protection and management of groundwater	ELM, MARS, M5 Tree, SVR	Showed the ELM and SVR performed better than the M5 Tree and MARS models, and when combined yielded high accuracy
Fijani et al., 2019	Small Prespa Lake, Western Macedonia, Greece	Some karst features causing sub-surface flow which is partially responsible for Small Prespa Lake's recharge	Water quality; Test a variety of low-cost modeling techniques to determine the optimal predictive model construction to be aid real-time water quality monitoring	ELM, LSSVM, CEEMDAN, VMD	The two-layer hybrid decomposition model improved performance with the VMD-CEEMDAN-ELM model showing the best performance
Ewusi, Ahenkorah, Aikins, 2020	Tarkwa, Western Region, Ghana	Mining community in Ghana with high water contamination, low intergranular permeability with some aquifer formation, water source is surface water and bore holes	Water quality; develop predictive model testing different constructions predicting TDS in groundwater, surface water, and drinking water in Tarkwa, Ghana, and evaluate the performance of the various models	GPR, BPNN, PCR	The advanced machine learning techniques, GPR and BPNN, are effective tools for predicting water quality indices and are a useful tool for future prediction and management of various water systems in mining communities
Ransom, Nolan, et al., 2021	Conterminous USA	Varied across the lower 48; Karst and Non-karst	Water Quality; employed three-dimensional extreme gradient boosting (XGB) machine learning model to predict nitrate based on several predictor variables within a network of 12,082 sampling wells	XGB	Showed XGB can be applied to three-dimensional national-scale groundwater quality modeling and provides a significant milestone in documenting nitrate in groundwater

Study	Study Location/Site Location	Landscape	Application	Machine Learning Approaches	Major Findings
Wunsch et al., 2021	Alpine/Mediterranean Region	Karst Around Mediterranean Sea	Use atmospheric and soil moisture levels to forecast flow from karst catchments in South Central Europe	CNN	The 2D-CNN (convolutional neural network) showed good performance in modeling the flow from the karst watershed
Ollivier et al., 2020	Fontaine de Vaucluse South-eastern France	Karst System	Used a reservoir-based model, complimented with multifactorial monitoring (neural network) to model flows from the karst catchment	Multifactorial monitoring	Demonstrated the effectiveness of machine learning at developing 2D and 3D modeling of the soil characteristics to aid in the accuracy produced by reservoir-based model of karst system
Ravinesh, Mehmet, 2016	Queensland, Australia	Eastern coast of Queensland; Gowrie Creek, Mary River, and Albert River	Flow prediction; predicting monthly streamflow based off hydrometeorological data, climate indices, and sea surface temp	ELM	Determined ELM offers an efficient approach for streamflow simulation and is practical for other hydrologic modeling
Yaseen; Sulaiman; et al., 2019	Malaysian Peninisula	Some karst features present on the Malaysian Peninsula	Flow prediction; assess the viability of the enhanced version of extreme learning machine (EELM) modeling of river flow	EELM	Shows utility in ELM variants to successfully model river flow based hydrologic variables and correlating lag times
Rezaie-Balf; Kisi; 2018	Tajan River, Iran	Some karst features in the area; due south of the Caspian Sea	Flow prediction; tested three soft computing methods in forecasting daily river flow	MLPNN, OP-ELM, EPR	Showed the EPR represented best performance in simulating peak flow compared to the other methods, while MLPNN significantly under or over estimated
Roushanger et al., 2017	Ajichay watershed, Northwest Iran	Mostly non-karst region	Rainfall-runoff, monthly river runoff	ELM, G-ELM, I-ELM, W-ELM	Showed the G-ELM model coupled with previous wavelet transformation produced an accurate representation of the study river flow
Yaseen et al., 2016	Tigris River, Iraq	Iraq has well known karst development	River/stream flow; Use of an ELM to forecast monthly stream-flow discharge rates in the Tigris River	ELM, SVR, GRNN	Found the ELM showed superior performance over the SVR and GRNN
Prasad et al., 2018	Australia	New South Wales where most Australia's agriculture is located, maintains a variety of geophysical conditions	Soil Moisture; Used an ELM integrated with ensemble empirical mode decomposition to forecast soil moisture	ELM, CEEMDAN, EEMD	EEMD-ELM proved to be highly efficient with better performance when forecast both upper and lower layer soil moisture
Feng et al., 2017	Shouyang, Shanxi Province, North China	Karst Region spread through Shanxi Province	Develop an ELM and generalized regression neural network models for maize evapotranspiration	ELM, GRNN	Showed the ELM and GRNN predicted well with meteorological and crop data, and generated acceptable predictions with just meteorological data
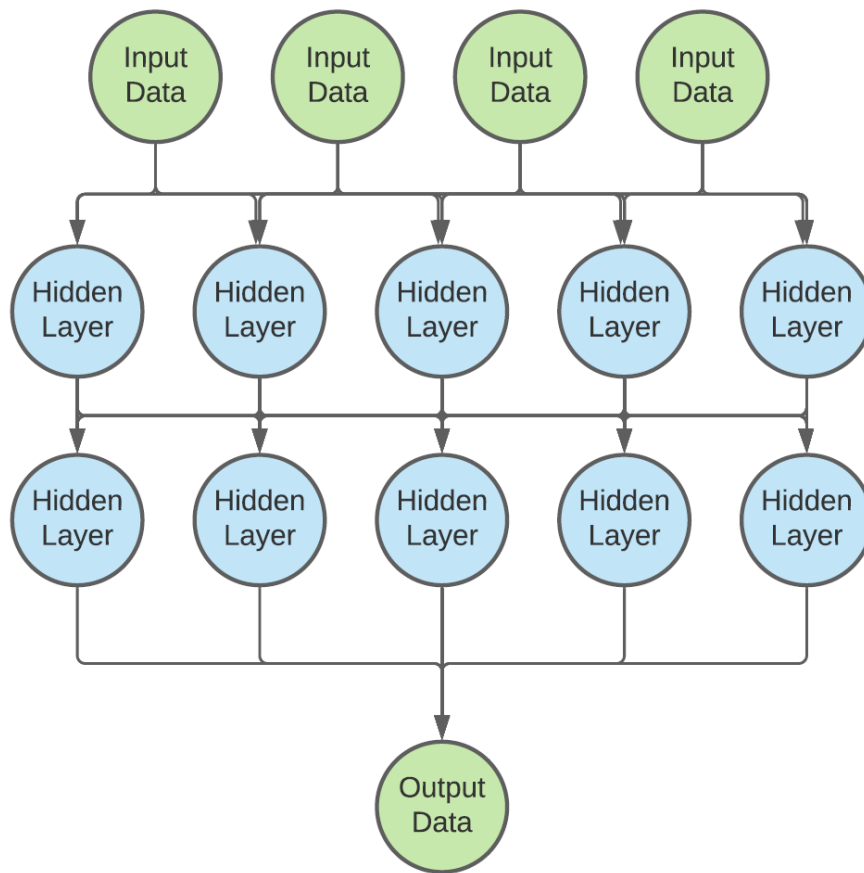
Figure 2.1: Structure of a feed forward neural network, such as an ELM. This shows how the data moves through the layers, with each neuron carrying a weight and a transfer function and each connection between neurons maintaining a bias. These weights and biases are randomly assigned and automatically adjusted during training.

CHAPTER 3.   **METHODOLOGY**

3.1   Study Site

To meet the objectives of this study, data collection and analysis efforts were conducted in the Camden Creek watershed within the Inner Bluegrass region of Kentucky, U.S.A (Figure 3.1). This watershed has a cumulative drainage area of 1,069 ha and drains a substantial portion of the University of Kentucky's 600 ha C. Oran Little Research Center (LRC). The LRC is the university's main animal research property, housing beef, swine, and sheep research facilities along with about 150 ha of row crops (Figure 3.1). The watershed is located within the Inner-Bluegrass physiographic region of central Kentucky which is characterized by a temperate Midwestern United States climate, maintaining four distinguishable seasons (Ford et al., 2019). The watershed is characterized by broad, shallow sinkholes; large valleys and ridges with low-relief; and sparse rock outcrops and thick, fertile soils (Ford et al., 2019). Over the past decade, the region has received an average annual rainfall of 1322 mm with an average temperature of 13.14°C (MRCC, 2021).

Heterogeneity has been observed in karst conduit maturity in the region and the Camden Creek watershed is reflective of heterogenous karst development (Ford et al., 2019; Mahoney et al., 2018; Reed et al., 2010). Local, ephemeral springs and seeps show high connectivity between the epikarst and the surface channel throughout the watershed. Further, the presence of a blue hole spring and cave spring show a more mature connection between the epikarst and phreatic zone in portions of the watershed. Fourteen individual springs have been identified on the LRC farm, including ephemeral, local perennial, and regional perennial springs (Ford et al., 2019). Dye traces elucidated

sinkhole connectivity and enabled delineation of springsheds, resulting in an estimated cumulative watershed drainage area extending well beyond the surface watershed (Ford et al., 2019). The complexity and heterogeneity of the karst features in the watershed makes process-based modeling a challenge and is an excellent testbed for assessing the utility of machine learning approaches for hydrologic and water quality modeling.

3.2   Data Collection and Analysis

To meet the objectives of this study, data collection efforts were focused on surface water quality and hydrologic data at the watershed outlet (Figure 3.1), along with the use of private and public databases maintaining data on meteorological variables, soil conditions, and fertilizer applications. Surface water measurements included flow depth and nitrate/nitrite concentration and were obtained from *in situ* water quality sondes that were validated using grab samples. Meteorological and soil variables including precipitation, wind speed, air temperature, solar radiation, soil moisture and temperature at depths of 10, 20, 50, and 100-cm were obtained from the National Centers of Environmental Information's climate reference network, which is operated through NOAA. Farm management data focused on the nitrogen fertilizer application rates in the watersheds and was estimated based on the pounds of inorganic nitrogen applied, and the volume of manure slurry applied to the fields. The types and duration of monitoring data are summarized in Table 3.1 and are further detailed in the following subsections.

3.2.1   Surface water measurements

Flowrates were estimated based on flow depths over a v-notch weir at the watershed outlet (Table 3.1). Pressure measurements were collected at a 15-minute interval, beginning on Aug. 29, 2018 through Aug. 4, 2021 (1070 days). Due to sensor

errors, research restrictions with the Covid-19 pandemic, and QAQC processing, some data is missing or was discarded. Of the 1070 days included in the collection period, 921 days are included for discharge data. Two YSI EXO2 sondes were used interchangeably throughout this project to collect flow depth data, with each unit requiring monthly calibration, battery replacement, and general maintenance consistent with manufacturer specifications (YSI Incorporated, 2014). Data was screened to check if points fell within maximum and minimum threshold values for the sensors per manufacturer specifications and were flagged if they fell outside of bounds. The data was then manually checked for any abnormalities or outliers and cross-referenced with field notes. Given the pressure sensor was not vented, corrections were needed to account for barometric pressure. The actual flow depth (YSI_{Depth}) was estimated using equation 1.

$$YSI_{Depth} = \left(YSI_{reading} + Baro_{DO} - Baro_{AP}\right) * 0.703 \frac{m}{psi} + Corr -$$

$$Offset \tag{1}$$

where, $YSI_{Reading}$ is the pressure value recorded by the YSI depth sensor in psi, $Baro_{DO}$ is the value entered for the barometric pressure (psi) during calibration of the DO sensor for each deployment of the YSI, $Baro_{AP}$ (psi) is the barometric pressure recorded at Bluegrass airport, *Corr* (m) is the correction for the height of the sensor above the bottom of the channel (0.282 m), and Offset (m) is the average difference between the corrected YSI depth measurements and the manual measurements taken during site visits. Barometric pressure values were obtained hourly from the Bluegrass Airport in Lexington, KY and was downloaded from the Midwestern Regional Climate Center. When the YSI EXO2 were swapped monthly, the depth in the channel was measured

using a meter stick with 1mm resolution. Measured values were compared with estimated

flow depths to ensure accuracy in measurements.

Flowrates (Q) at the watershed outlet were estimated based on flow depths over a

downstream weir. This weir was installed in August 2018 and included a 120° V-notch

with an invert 0.5 feet from the channel bed. The top of the weir was 1.5 ft from the bed

and was 14 feet wide to accommodate the width of the culvert. This construction resulted

in piecewise flow rate calculations depending on if flow was restricted within the v-notch

(equation 2a) or flowed over the broad crested weir (equation 2b).

$$Q = 4.330d^{2.5} \qquad \text{if d} < 1\text{ft} \tag{2a}$$

$$Q = 4.330 + 46.62(d - 1)^{1.5} \qquad \text{if d} > 1\text{ft} \tag{2b}$$

where d = height above the invert of the v-notch (ft) which was estimated based on the

total flow depth and distance of the weir crest from the channel bed.

High-frequency nitrate measurements at the watershed outlet were obtained using

a SUNA V2 sensor manufactured by Sea-Bird Scientific. The SUNA measures nitrate-

nitrite concentration using their intrinsic absorption of UV light at wavelengths less than

240 nm, with a resolution of approximately 1 nm. The SUNA contains a stable UV light

source, a straight-through quartz sampling chamber, and a precision spectrometer to

measure the UV absorption. There is an onboard absorption curve-fitting algorithm using

laboratory/manufacturer calibrated instrument-specific extinction coefficients for nitrate-

nitrite that resolve the measured absorption into a concentration (MacIntyre et al., 2009).

Values of nitrate-nitrite as N were reported as milligrams of nitrogen per liter, mgN/L.

Data was collected from Sept. 7, 2018 to Aug. 4, 2021 at 15-minute intervals. Similarly,

to the flow data, there are periods of missing nitrate data due to sensor errors, restrictions

to research from Covid-19 precautions, and data that failed QC protocols. The longest period of missing date fell from Nov. 20, 2019 until July 20, 2020 and this was a combination of problems that led to the SUNA needing to be sent to Sea-Bird for servicing and was returned to the university after Covid-19 work restrictions were in place. Reference spectrum updates were completed every one to three months based on weather conditions and lab access, although most updates were carried out every four to five weeks. The sensor was checked for debris or other possible fouling during site visits. The SUNA was powered externally and a data logger was used to store and offload data. The data collection platform consisted of a solar powered instrument panel consisting of a Hubbell-Wiegmann NEMA 12 JIC series enclosure which houses a Sutron X-link data logger, a voltage regulator, two fuse blocks, and three terminal blocks. The software used to communicate with the SUNA V2 was Sea-Bird Scientific's UCI 2.0.3 version software (Scientific, 2019). Quality control analyses were performed using an analogous approach to YSI sensors. Additionally, the SUNA reported an RMSE value with each measurement to estimate the goodness of the nitrate spectral fit. The SUNA values were noted and flagged if this RMSE value was reported as 0.001 or higher. Grab samples were used to validate SUNA measurements and ensure flagged values were still accurate. At least two samples were collected each month and were delivered to the Kentucky Geological Survey (KGS) for analysis of nitrate nitrogen (NO_3-N). KGS follows EPA method 9056A-Determination of Inorganic Anions by Ion Chromatography when determining the nitrate concentration of surface water samples (EPA, 2007). Linear regression was performed between measured nitrate values and surrogate nitrate estimates to check for accuracy and precision (Bunnell, 2020).

3.2.2 Meteorological and Soil moisture data

Soil and meteorological data were obtained from the Midwestern Regional Climate Center cli-MATE database (MRCC, 2021) and the US Climate Reference Network (Diamond et al., 2013). Soil and meteorological variables were collected by the automated weather observation system (AWOS) located on the LRC property (ID:63838). This station contains a Geonor T-200B series precipitation gauge and three sets of HydraProbe II sensors using SDI-12 connection mounted 120° off from each other (Figure 3.2), which are the standard mandated by NOAA (Geonor, 2016; Stevens, 2019; NOAA, 2021). The station latitude and longitude are 38.0944 and -84.7464, respectively (Figure 3.1). Soil moisture and temperature sensors were located at 10, 20, 50, and 100-cm depths at the monitoring station. Data was collected hourly and were interpolated to fifteen-minute data using linear interpolation. Atmospheric variables including precipitation, 1.5m windspeed, air and surface temperature, relative humidity, and solar radiation data were obtained at 5-minute intervals and were aggregated to 15-minute intervals. The meteorological and soil data was obtained for the entire monitoring period, starting on Aug. 29, 2018 and running through Aug. 4, 2021. There were also several periods when data was missing, with the longest period being the 100-cm data from August 29, 2018 to June 30, 2019. Data is also missing from December 31, 2018 19:15 (7:15 pm) until January 12, 2019 23:45 (11:45 pm) for air temperature, precipitation, surface temperature, and 1.5m wind speed. Portions of the 50-cm soil moisture data were also cleaned due to inconsistencies with the soil moistures at the other depths and precipitation data. During manual inspection it was determined there were irregular jumps in the 50 cm soil moisture data that resulted in a significant spike over an hour

period, with some spikes being 50% of the baseline value. These spikes were only seen for one to two hours (one or two data points) and quickly returned to the pre-spike level and occurred 18 times throughout the monitoring period. To ensure these were not trends in the soil moisture, the 50-cm values were compared with the 10, 20, and 100-cm soil moistures, as well as the precipitation data. If there were variations in any of these values within two hours of the suspect point that may have corresponded with changing conditions at the weather station the 50-cm soil moistures were not corrected. If these values were unchanging at or around the suspected time stamp the 50-cm soil moisture was assumed equal to levels before and after the jump. Due to unrealistic shifts in the 100-cm data through 2019 and early 2020, inclusion in the TELM training and evaluation began on July 29, 2020. This was to ensure a consistent, realistic representation of the dynamics within the deep soil was used.

3.2.3 Management Data

The study watershed receives several different fertilizer applications ranging from inorganic sources such as urea and urea ammonium nitrate to organic sources such as dairy and swine slurries. These fertilization periods typically occurred between March and June, which coincides with crop planting. All inorganic fertilizer inputs at the LRC were accessed through the cloud-based farm management software, Granular Business, that discretizes the farm into fields based on usage, allowing farm personnel to manage and record important events and treatments each field receives. The organic fertilization data was not available on the Granular database therefore it had to be acquired from farm managers directly. This application data was also broken down using the same discretized

27

fields used for the inorganic fertilizer application. The values reported were daily applications values and are summarized in Appendix B and C.

3.3   Analytical Methodology

To assess how temporal variability of soil moisture at various levels within the soil profile and fertilization impact nitrate loading dynamics in disturbed agroecosystems, a form of extreme learning machine (ELM) was utilized known as a two-hidden-layer ELM (TELM). The ELM was chosen due to its success in hydrologic and water quality studies and its ease of implementation, and the TELM has been shown to outperform the original ELM (Qu et al., 2016). ELMs are traditionally single hidden layer feed forward networks that assign the weights between the input layer and hidden layer and bias of the hidden layer randomly and then tune themselves to map the assigned input data to the defined output variable. In a TELM, like in an ELM, the weights and bias of the first hidden layer are randomly assigned with the output of the first hidden layer being the weight matrix of the second hidden layer, rather than being randomly initialized like the first. Qu et al., 2016 outlined the structure, function, and process. Next, we assessed the utility of the TELM models to reflect hysteresis patterns in nitrate concentration data, and diurnal variability (e.g., in-stream processes).   Finally, we assessed the impact of prevailing variables on nitrate loading in the karst agroecosystem watershed.

3.3.1   Extreme Learning Machines Model Setup and Evaluation

To build our TELM, an optimized tensor computation package known as PyTorch was employed to assist in model generation in Python. PyTorch is an open source project produced by Facebook, Inc. to be used for deep learning applications using graphics

processing units (GPUs) and central processing units (CPUs), with a strong history of recent use in academia (Chen et al., 2019; Steppa & Holch, 2019). PyTorch provides tools and library used across many sectors to call from, allowing for the creation and implementation of advanced machine learning application without requiring in depth knowledge on the intricacies of machine learning algorithms. PyTorch provided the framework to construct the neural network and designate the model characteristics such as number of hidden layers, number of neurons within the hidden layer, activation function contained within the hidden neurons, and structure to implement the other modules used in the models construction (torch.nn.Module, 2019; PyTorch, 2021). Many universities and other institutions of higher learning that are now offering courses which focus on using PyTorch in their machine/deep learning curriculum (Cornell, 2021; Devry, 2021; Maryland; Soylu, 2021).

Several other Python modules were used in the development with PyTorch. Pandas and NumPy are modules used for fast, powerful, flexible, and easy analysis and manipulation of data. These modules allow users to apply scientific computing to data by arranging the input data into arrays, quickly parse and remove any data based on user defined parameters and manipulate the shape and dimensions of the arrays for computation (pandas, 2021; NumPy, 2005). Sklearn or scikit-learn is a module that supports supervised and unsupervised learning and provides various tools for model fitting, data preprocessing, model selection and evaluation, among other uses (sci-kit learning, 2019). It was used to define specific parameters, in conjunction with those with PyTorch, within the learning model such as the splits for the training and testing datasets and the min/max scaler used to normalize the datasets after the training and testing sets

were defined. Captum is another module used in the development of the learning model and was used to determine the variables that carried the most influence throughout training. Due to the increasing complexity and lack of transparency in model interpretability, this module provides algorithms, like integrated gradients, that understand which features provide greater influence in the model output (Captum, 2021). The last two modules leveraged in the development of the TELM were OpenPyXL and Matplotlib. OpenPyXL allows for the easy reading and writing from Python to xlxs and xlsm formats (Gazoni et al., 2021). This was used to write output of the model such as the predictions and attributions, or variables of influence and their associated influence percentages to an Excel spreadsheet. Matplotlib is a comprehensive library for creating static, animated, and interactive visualization in Python (Hunter et al., 2021). This module was used to generate the plot and figures used during model training and the graphs that were associated with the attribution functions.

Variables used as inputs for the flowrate and nitrate concentration models were based on available long-term atmospheric, soil moisture and management data which were perceived to impact hydrologic and N cycles in the karst agroecosystem watershed. Inputs to both models included precipitation, air temperature, ground surface temperature, soil moisture and soil temperature at depths of 10, 20, 50, and 100-cm, solar radiation, 1.5m wind speed, and relative humidity. For the nitrate model, pounds of inorganic nitrogen applied, gallons of swine slurry applied, and gallons of dairy slurry applied were also included. The fertilizer application data was included as an input for the model due to its perceived impact on nitrate exports. By including the organic and inorganic fertilizer separately the impacts of the fertilizers from different sources can be

better elucidated, and by separating the organic sources between dairy and swine the impacts can be further refined. Both the inorganic and organic fertilizer data received from the Granular database and farm managers were in daily totals applied to the discretized fields, meaning, to be used as a model input, the total fertilizer applied per day was distributed uniformly at 15-minute applications over the eight-hour working period of the days applied, with all other fertilizer values being zero. In other words, each time that did not fall during the eight-hour working period of the days of fertilizer application had fertilization values of zero.

The initial model tested was a two hidden-layer extreme learning machine with 50 neurons in each hidden layer. This multi-layer construction was also tested with neuron counts of 40, 60, and 100. For the single layer construction, neuron counts of 40, 50, 60, 80, and 100 were tested. Each scenario was run at least four times with the construction that produced the lowest mean squared error (MSE) being the model chosen for all scenario analysis. Once the model construction was determined, multiple runs with differing sets of training data were tested to see the effects on the accuracy of the model predictions, giving insight on the effects of the different sets (scenarios) on the nitrate exports and flow discharge of the system. These sets included combinations of the atmospheric variables (precipitation, 1.5m windspeed, air and surface temperature, relative humidity, and solar radiation), soil moisture at 10-cm, 20-cm, 50-cm, and 100-cm, soil temperature at 10-cm, 20-cm, 50-cm, and 100-cm, and inorganic and organic fertilization, which are summarized in Table 3.1. Scenarios were identical for flow and nitrate, except nitrate had an additional run to consider the impact of fertilization. The 100-cm soil moisture data was not included in most of the model runs because there were

larger gaps in the database as compared with other datasets, however it was considered after determining influential parameters in the broader dataset.

For each of the aforementioned scenarios, the training datasets were used to predict nitrate concentrations and flowrates. At the beginning of each run, all the collected data for all variables within the system were loaded into the model. There is a set of user defined options, one of which allows the user to define which variables are then included in model training and testing. The other options include batch size, use the CPU or GPU to run the model (if a GPU is available), neuron count, learning rate, the loss warning threshold, the loss exit and save threshold, the model name to load, and the model name to save. Data was randomly divided into fifths in which four of the divided sets were used to train the model in batches and the last fifth was retained to validate the model's effectiveness. Within the model, each input is represented by a neuron in the input layer, and each of these neurons is connected to the neurons within the first hidden layer (Table 2.1). Each connection between the neurons of the different layers has a weight and when the model is initialized the weights between the input layer and first hidden layer are randomly assigned. This random assignment of weights at initialization differentiates extreme learning machines from other neural network applications and removes the need to iteratively tune the weights, reducing the time required to train the model. Each neuron in the hidden layer has an activation function which defines the output of the neuron, based on the inputs. The outputs of the first hidden layer are then passed to the second hidden layer, with each connection having its own weight which is assigned by the TELM based off the information passed between neurons. Each neuron in the second hidden layer has an activation function which behaves analogously to the first

hidden layer. The activation function used in this study was the Rectified Linear Unit activation function, which is a commonly cited and used activation function within deep learning (Agostinelli et al., 2014; Banerjee et al., 2020; Jin et al., 2015).

The output of the TELM model was then used to evaluate the performance of the model. The test data is then used to verify the model's accuracy and the model will reinitialize the training after each run until a user specified variation threshold is reached or a user specified number of epochs without variation is reached. Each iteration of training is called an epoch. At the completion of each epoch, a scatter plot showing the predicted regression and several test points is generated, as well as the percent of predicted values that fall within defined percentiles. This gives the operator an indication of the model's accuracy. Mean square error (MSE) was output directly from the model during training and testing to monitor the progress and performance while learning. This is the default loss function for most PyTorch regression models and is calculated as

$$loss\left(y_i^{obs}, y_i^{pred}\right) = (y_i^{obs} - y_i^{pred})^2 \tag{3}$$

where y_i^{obs} represents the *i*th observation of the measured value and y_i^{pred} represents the *i*th observation of the predicted value. Once model runs were completed, the predictions from each of the trained models were generated and exported to Excel to compare with the measured values and calculate the root mean squared error (RMSE) of each run.

$$RMSE = \sqrt{\frac{\sum_{i=1}^{N}(y_i^{obs} - y_i^{pred})^2}{N}} \tag{4}$$

where *N* represents the number of samples, y_i^{obs} represents the *i*th observation of the measured value, and y_i^{pred} represents the *i*th observation of the predicted value. Following the RMSE calculation, Nash-Sutcliffe Efficiency (NSE) was also used to

verify the TELM's effectiveness at capturing the nitrate variation. NSE is a widely used statistic for evaluating hydrologic and water quality models (Moriasi et al., 2007; McCuen et al., 2006).

$$NSE = 1 - \left[\frac{\sum_{i=1}^{N}\left(y_i^{obs} - y_i^{pred}\right)^2}{\sum_{i=1}^{N}\left(y_i^{obs} - y^{mean}\right)^2} \right] \tag{5}$$

where y_i^{obs} represent the ith observation of the measured constituent being evaluated, y_i^{pred} represents the ith observation of the predicted constituent being evaluated, y^{mean} represents the mean of the observed data for the constituent being evaluated, an N is the total number of observations (Moriasi et al., 2007).

3.3.2   Impact of variables on flowrates and nitrate concentrations

Using the Captum module, the impact each of the variables has on the model training was performed with the intention of understanding how the system interacts holistically, while also giving a representation of the most important data to collect in future studies at different locations. The feature of the Captum module used for this study was integrated gradients (IG). Gradients of the output with respect to the input within the model are a natural analog of the model coefficients for a deep network, meaning they are a good starting point for defining the attribution, or relevance, of inputs to the output (Sundararajan et al., 2017). IG recognizes these gradients within the trained model and integrates them across the entire sample to determine the average importance each variable carried during the training process, see Sundararajan et al., 2017 for full explanation of integrated gradients. By using these integrated gradients, each variable's perceived effect on the system can be represented. For this reason, determining the variables of influence driving nitrate exports within karst agroecosystems was an

important consideration to enable the most accurate model generation with the least number of variables, therefore requiring the fewest sensors. These values were reported as a decimal summing to 1. This attribution function was run three times for each model run to ensure an accurate estimate was made due to the use of Riemann Sum to determine the IG. Once generated from each model run, the IG were averaged, giving a composite IG for each run. The composite IGs from each run were then averaged to give an IG for each scenario.

3.3.3 Overfitting

Overfitting due to a small training dataset was not a concern because the different scenarios contained between roughly 35,000 to 75,000 datapoints. To ensure our ELM does not suffer from overfitting due to the use of a large number of inputs, variables were pruned from the full dataset to reduce the complexity of the neural network. This post-pruning method used the attribution scores generated from the scenarios testing variable influence to determine which variables were least important in training and removed them to prevent redundancy, as described in Bishop, 1995. The first scenarios used only the six atmospheric variables in scenario 3 for nitrate and scenario 2 for discharge, designated as nitrate overfitting (OF) scenario 1 and discharge OF scenario 1. Trials were also conducted using only six soil condition parameters (moisture level and temperature at 10-cm, 20-cm, and 50-cm) for the full monitoring period and eight soil condition parameters (moisture level and temperature at 10-cm, 20-cm, 50-cm, and 100-cm) for the portion of the monitoring period with reliable 100-cm data for both nitrate concentration and discharge modeling (Table 3.2). To determine if overfitting occurred in the original model scenarios due to redundant variables, NSEs were calculated for the overfitting

35

scenarios and compared to those generated for the variable analysis. If overfitting occurs due to redundant variables, all NSEs calculated would be lower regardless of the combination of variables; however, if the NSEs calculated from the OF scenarios using the variables with the highest attributions scores (soil conditions) are similar to the scenarios using all variables, the ELM does not overfit due to the inclusion of redundant variables.

3.3.4   Hysteresis and Diel variability Analysis

Evaluating predictive models' performance at predicting concentration-discharge relationships, is particularly important to accurately estimate loading dynamics and how changes in environmental variables may alter loading. To evaluate the ability of the machine learning model to predict nitrate hysteresis, a hysteresis index (HI) for specific storm events during the monitoring period were selected. The index was determined by first normalizing the flow and concentration data for each event. This was accomplished using the equations

$$Q_{norm} = \frac{Q_i - Q_{min}}{Q_{max} - Q_{min}} \tag{6}$$

where Q_i is the measured flow at the ith time step, Q_{min} is the minimum flow measured during the event period, and Q_{max} is the maximum flow measured during the event period, and

$$C_{norm} = \frac{C_i - C_{min}}{C_{max} - C_{min}} \tag{7}$$

where, C_i is the measured nitrate concentration at the ith time step, C_{min} is the minimum nitrate concentration measured during the event period, and C_{max} is the maximum nitrate concentration measured during the event period. With data normalized, the HI can be

36

determined by relating C_{norm} with the same values of Q_{norm} before and after the peak flow during the event and applying the equation

$$HI_{i\%} = C_{i\%\ before\ max} - C_{i\%\ after\ max} \tag{8}$$

where, $HI_{i\%}$ is the hysteresis index for the ith percent, $C_{i\%\ before\ max}$ is the normalized concentration at $Q_{i\%\ before\ max}$, and $C_{i\%\ after\ max}$ is the normalized concentration at the $Q_{i\%\ after\ max}$. For example, for $HI_{90\%}$, $C_{i\%\ before\ max}$ equals the C_{norm} that coincides with $Q_{90\%\ before\ max}$ and $C_{i\%\ after\ max}$ equals the C_{norm} that coincides with $Q_{90\%\ after\ max}$. This was performed for the range of flows experienced during the rain event. The intention was to have one small, one medium, and one large event represented during each of the four seasons and compare the observed hysteresis (using the measured nitrate concentration and observed discharge), with the modeled hysteresis (using the predicted nitrate concentration and observed discharge). Nevertheless, a large event was not captured during the summer months within the monitoring period. The sizes within each category varied slightly between the seasons, with the small events having a peak Q_{obs} less than 0.3 cms, medium events between 0.3 and 0.9 cms, and large events greater than 1 cms. The seasons were defined as winter being December 21st through March 19th, spring being March 20th through June 20th, summer being June 21st through September 21st, and fall being between September 22nd and December 20th. In total, eleven storm events were selected for analysis. These events chosen are summarized in Table 3.3: Summary of the rain events chosen to perform the hysteresis analysis. Three events of varying sizes were chosen from each season to evaluate the TELM's ability to capture storm event dynamics. No captured event during the summer met the criteria for a large event.

Daily fluctuations in nitrate data are likely due to in-stream aquatic vegetation and microbial processes (Yang et al., 2019). To evaluate the ability of the nitrate concentration model to reflect diel fluctuations, timeseries of measured and modeled results were compared visually for periods with and without pronounced diurnal flucutations. These periods were chosen based on the findings of Bunnell (2020), where diel variability in the nitrate signal was minimal during the late fall and winter months, and greater in spring and summer. These observation dates were also distributed throughout these respective seasons to further test the models ability to capture these variable diel fluctuations. The dates are summarized in Table 3.3.

3.4 Tables and Figures

Table 3.1: Summary of the variables included in each set of training scenarios. With the model construction determined, nitrate (green) and discharge (orange) were mapped to with different combinations of data. Each combination was trained three times to develop an average. The highlighted cells indicate which variables were included in each set of runs.

		Nitrate ELM modeling				Discharge ELM modeling		
		Scenario 1	Scenario 2	Scenario 3	Scenario 4	Scenario 1	Scenario 2	Scenario 3
Precipitation		▦	▦	▦	▦	▨	▨	▨
Wind Speed		▦	▦	▦	▦	▨	▨	▨
Solar Radiation		▦	▦	▦	▦	▨	▨	▨
Air Temp		▦	▦	▦	▦	▨	▨	▨
Surface Temp		▦	▦	▦	▦	▨	▨	▨
Relative Humidity		▦	▦	▦	▦	▨	▨	▨
Soil Moisture	10 cm	▦	▦		▦	▨		▨
	20 cm	▦	▦		▦	▨		▨
	50 cm	▦	▦		▦	▨		▨
	100 cm				▦			▨
Soil Temp	10 cm	▦	▦		▦	▨		▨
	20 cm	▦	▦		▦	▨		▨
	50 cm	▦	▦		▦	▨		▨
	100 cm				▦			▨
Inorganic Fertilizer		▦						
Swine Fertilizer		▦						
Dairy Fertilizer		▦						

Table 3.2: Summary of the variables included in the scenarios used to test the model does not overfit. Nitrate (green) and discharge (orange) were mapped to different datasets that were reduced based on attributions score. The highlight cells indicate which variables were included in each set of runs.

	Overfitting Nitrate ELM modeling			Overfitting Discharge ELM modeling		
	OF Scenario 1	OF Scenario 2	OF Scenario 3	OF Scenario 1	OF Scenario 2	OF Scenario 3
Precipitation	green			orange		
Wind Speed	green			orange		
Solar Radiation	green			orange		
Air Temp	green			orange		
Surface Temp	green			orange		
Relative Humidity	green			orange		
Soil Moisture 10 cm		green	green		orange	orange
Soil Moisture 20 cm		green	green		orange	orange
Soil Moisture 50 cm		green	green		orange	orange
Soil Moisture 100 cm			green			orange
Soil Temp 10 cm		green	green		orange	orange
Soil Temp 20 cm		green	green		orange	orange
Soil Temp 50 cm		green	green		orange	orange
Soil Temp 100 cm			green			orange
Inorganic Fertilizer						
Swine Fertilizer						
Dairy Fertilizer						

Table 3.3: Summary of the rain events chosen to perform the hysteresis analysis. Three events of varying sizes were chosen from each season to evaluate the TELM's ability to capture storm event dynamics. No captured event during the summer met the criteria for a large event.

Season	Size	Start Date	End Date	Max Q (cms)
Summer	Small	7/29/2020	8/9/2020	0.18
	Med	7/3/2019	7/13/2019	0.4013
	Large	None	None	None
Fall	Small	12/19/2020	12/23/2020	0.14
	Med	10/28/2020	11/10/2020	0.357
	Large	10/30/2019	11/7/2019	1.85
Winter	Small	2/10/2021	2/21/2021	0.2796
	Med	1/30/2021	2/10/2021	0.843
	Large	2/27/2021	3/14/2021	2.76
Spring	Small	4/23/2021	4/29/2021	0.081355
	Med	5/2/2021	5/22/2021	0.756
	Large	6/6/2021	6/13/2021	1.53

Table 3.4: Summary of the base-flow dates and seasonal distribution chosen to compare mesaured and predicted diel variablity to assess the TELM's ability to capture short terms seasonal dynamics observed in the study system.

Season	Start Date	End Date
Mid-Fall	15-Nov-20	29-Nov-20
Late-Fall	6-Dec-20	16-Dec-20
Mid-Winter	11-Jan-21	24-Jan-21
Early-Summer	25-Jun-21	30-Jun-21
Mid-Summer	24-Jul-21	4-Aug-21
Late-Summer/Early-Fall	17-Sep-20	1-Oct-20
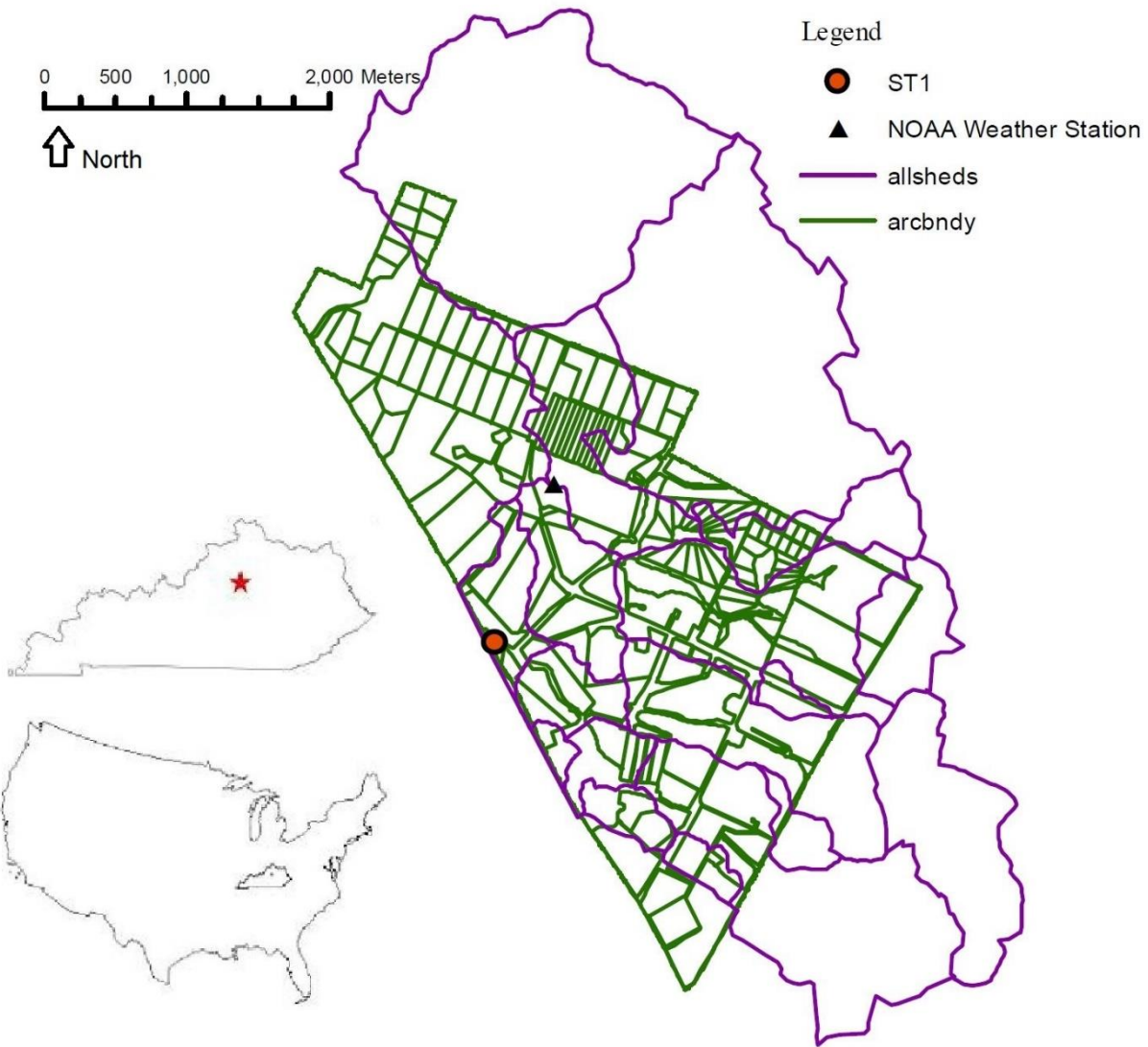
Figure 3.1: The LRC property lines with the discretized fields based on usage and fertilization; the basin and overall watershed boundaries; the stream network on the watershed; the ST1 monitoring site; and the NOAA weather station.

Figure 3.2: The AWOS on the LRC property that collected the atmospheric and soil data.

CHAPTER 4. **RESULTS**

4.1   In-stream and soil data results

Comparison of laboratory analysis of grab samples and SUNA V2 in situ measurements showed that the SUNA V2 is an accurate and unbiased estimator of nitrate-N concentrations (Figure 4.1-4.2). The best-fit linear regression equation between laboratory and SUNA V2 measurements had a slope of 0.96 and an intercept of 0.07. The regression was performed on 80 grab samples and resulted in an R^2 value of 0.98 (Figure 4.1). A perfect relationship between the in situ and laboratory measurements would result in a slope of 1, intercept of 0, and R^2 value of 1. Therefore, it is evident the SUNA does an excellent job of capturing the range of concentrations, especially considering the potential uncertainties associated with both the *in-situ* measurements and the analytical errors for the laboratory method.

Timeseries of the nitrate and discharge data highlighted the impacts of flow pathway dynamics, seasonality, and in-stream processes on nitrate concentrations throughout the monitoring period (Figure 4.2). The three-year timeseries of flow and nitrate data (Figure 4.2a) illustrates seasonality of nitrate concentrations in the karst agroecosystem watershed. During summer, (July-September) concentrations were lowest on average with concentrations often dropping below 2 mg/L. Low concentrations coincided with lower flow conditions. Conversely, during the higher flow conditions of late fall and winter, concentrations were substantially higher, often exceeding 4 mg/L. During rain events (Figure 4b-e) a dilution in the nitrate concentration is observed on the rising limb of the hydrograph, although this dilution is much more prominent in winter months as compared to summer months, likely reflecting the gradients observed in pre-

event concentrations between the seasons. On the falling limb of the hydrograph, nitrate concentrations increased and often met or exceeded pre-event levels. The rebound of nitrate concentrations reflected the magnitude of the event as evidenced by the delayed rebound of nitrate in the small winter event (4.2b) as compared to the larger winter and summer events (4.2c-d). Strong diurnal variations were also commonly observed during the summer months in between storm events (Figure 4.2d and 4.2e) but were often not prominent in winter months (Figure 4.2b and 4.2c) likely reflecting in-stream aquatic vegetation and microbial production and respiration processes which result in increased concentrations during the night when respiration is prominent and decreased concentrations during the day when primary production is prominent (Pellerin, 2021; Bunnell, 2020).

Findings from our study site are reflective of upland connectivity, seasonal, and in-stream processes that are typical of karst and agricultural watersheds, excluding findings from heavily fertilized agricultural landscapes (Baran et al., 2008; Blaen et al., 2017; Buda & DeWalle, 2009; Liu et al., 2007; Husic et al., 2019; Jackson et al., 2020; Yue et al., 2019). Storm event hysteresis patterns observed in the data reflect hydrologic connectivity pathways that have been commonly described during events in karst landscapes. Lui et al. (2007) and Jackson (2020) showed similar seasonal trends and storm event dilution and recharge characteristics in their karst study sites when analyzing biogeochemical process such as CO_2 production in soils, specific conductance (SC), and dissolved inorganic carbon (DIC). Likewise, numerous studies have highlighted the impact of wet seasons on enhanced nitrate concentration and loading (e.g., fall through early spring for our study site) due to the enhanced connectivity and flushing of nitrate

rich pore waters in the soil (Basu et al., 2010; Husic et al., 2019; Yang et al., 2017; Yue et al., 2019). Further, our results showed a decrease in nitrate concentrations during the day and an increase during the night in warm periods of late spring-early fall. Results from Bunnell (2020) demonstrated that these diurnal patterns in nitrate are correlated with diurnal fluctuations in dissolved oxygen saturation. Maximum values of dissolved oxygen saturation during the day are recognized to be governed by growth of aquatic vegetation that release oxygen into the water column, and minimum values at night reflect prominence of the endogenous and microbial respiration processes in the stream ecosystem (Grace et al., 2015). The impacts of in-stream processes on fluvial nitrogen budgets has been broadly recognized (Alexander et al., 2009; Bernhardt et al., 2005; Ford et al., 2017; Griffiths et al., 2013; Mulholland et al., 2008) and has been increasingly observed in high-frequency nitrate measurements (Carey et al., 2014; Pellerin et al., 2013; Rode et al., 2016; Yang et al., 2019). Contrary to findings from heavily fertilized agricultural fields and watersheds, we did not find flushing of nitrate-rich waters during the rising limb or peak of the hydrograph (Ford et al., 2018; Kennedy et al., 2012; Rusjan et al., 2008). Collectively, the findings suggest the study site is a representative testbed to evaluate the ability of machine learning algorithms to represent hydrologic connectivity processes of N sources, as well as in-stream processes; although its ability to reflect fluvial fertilizer losses may be limited.

Comparison of the nitrate measurements with soil moisture data illustrates that the magnitude and variable response of soil moisture layers with depth influence nitrate concentrations at the watershed outlet (Table 4.4). The measured nitrate concentrations were typically low during periods of low soil moisture and concentrations were elevated

during periods of high soil moisture (Figure 4.3a). Generally, larger changes in soil moisture levels corresponded with larger shifts in the nitrate concentrations measured at the watershed outlet. Furthermore, when looking at events during seasonal transitions from dry to wet periods, particularly summer to late fall (Figure 4.3b), the variable soil moisture responses within different layers of the soil profile corresponded with a variable response in nitrate concentration fluctuations. When the shallower depths of the soil profile (10 and 20-cm depths) had increasing soil moisture contents without a response in deeper soil layers (e.g., Aug 25-26, 2019), some increase in nitrate concentration were observed, although responses were often relatively small (1.26 to 1.86 mg/L). Conversely, as deeper layers of the soil profile (e.g., 50-cm) had increasing soil moisture content, larger shifts were observed in nitrate concentrations. For instance, the event seen on Oct 6, 2019 impacted the 50-cm depth with an increase in VWC from 0.1325 to 0.1875, and a subsequent increase nitrate concentration, from 0.357 to 2.53 mg/L, was measured (Figure 4.3b). There is also a lag in activation between the layers of the soil profile seen when all measured layers are activated during events (Figure 4.3c). This shows the deeper layers begin to activate and reach their peak levels later in the event that the shallower layers, with the 100-cm layers showing activation following all other layer's peak activation.

The coupled response of soil moisture and nitrate exports emphasize the importance of matrix-macropore interaction in soils on controlling nitrate loading. As the soil moisture increases, the stored matrix water becomes more connected with the macropore pathways and is transported to the karst features, ultimately being conveyed out of the watershed. This has been reported in several studies (Donner et al., 2004;

48

Yevenes and Mannaerts, 2011; Tian et al., 2015; Husic et al., 2019), and some studies have shown asymmetric profiles in nitrate concentrations at varying depths within the soil column (Igbal and Krothe, 1994; Green et al., 2018), however these studies did not specifically link soil moisture variations based on depth and the impact this has on nitrate loading in karst agroecosystems. The visual connection between the different depths within the soil column and their perceived effects on the nitrate concentration measured at the watershed outlet were evident, with activation due to rain events within the 10 and 20-cm zone corresponding with smaller, storm event associated nitrate dynamics, and the deeper reaches of the soil profile, corresponding with the large, seasonal fluctuations associated with the flushing events that drive overall nitrate loading from these karst agroecosystems. This is likely due to the deeper regions of the soil profile becoming disconnected from the macropores and karst network during the vegetative growth season resulting from the higher water usage at the surface. During these periods, water and nutrients are pulled from the active root zone and used for plant growth. The study system is predominantly used for cattle grazing and is therefore pastureland. This means the prevailing vegetation is Bluegrass with an average effective root depth of approximately 46-cm, while the other cultivated crops on the property (soybeans, corn, and wheat) having an average effective root depth zone of 61-cm (Staff, 2005). As a rule of thumb, the effective root depth accounts for about 70% of the moisture extracted by the root. This indicates most of the vegetation growing at the LRC is extracting much of the required water and nutrients from the regions of the soil profile shallower than 50-cm during the main growth season. This results in the 50-cm and deeper regions of the soil becoming disconnected, leading to a buildup of nitrate and other nutrients during the

49

warmer summer months. Following the growth season and the deeper regions of the soil matrix become connected to the macropores and karst pathways, a flushing of nitrate occurs from these karst agroecosystems, resulting in elevated nitrate exports throughout the wetter, winter months. The impacts of ET on nitrate concentration and flow are supported by a reservoir-style modeling approach recently applied in a nearby mature karst watershed (Husic et al., 2019).

4.2 Extreme Learning Machine Models for Flow and Nitrate concentrations

4.2.1 Flowrate ELM modeling

The results of the three discharge modeling scenarios showed the importance of including vertical soil profile variability in predicting flowrate dynamics in karst agroecosystem watersheds. Scenario 2 (which only used atmospheric variables) had the lowest performance with the calculated Nash-Sutcliff Efficiency (NSE), ranging from 0.1511 to 0.1549 with the average being 0.1551. For scenario 1 the NSE values fell between 0.5974 and 0.6558 with the average of the runs being 0.6519. The NSE values showed great improvement for scenario 3, with NSE ranging from 0.9228 to 0.9363, with the average of the runs being 0.9328. These results are summarized in Table 3.1. Moriasi et al. (2015) outlined ranges to interpret NSE for flow values at the watershed scale at a daily, monthly, and annual time step, with $0.80 < NSE \leq 1$ being considered very good, $0.70 < NSE \leq 0.80$ being good, $0.50 < NSE \leq 0.70$ being satisfactory, and below 0.50 being not satisfactory; however, it is often suggested that ranges should be relaxed for higher frequency measurements. Nevertheless, under this criterion, the findings for scenario 1 are satisfactory and scenario 3 are very good. Visually, scenario 2 reacts to overall baseflow but does not capture any response beyond seasonal changes, and these

are subtle. Scenarios 1 and 3 capture the seasonal trends and storm event changes well; however, scenario 1 does not capture the extremes in the flow response. Scenario 3 shows a strong ability to recognize the magnitude of the events and successfully captures the extremes, especially the peaks, well.

Integrated gradients analysis highlighted the importance of soil moisture and temperature data (see appendix G) for accurately predicting discharge from the karst agroecosystem watershed. The integrated gradients for scenarios 1 and 3 returned the 50-cm moisture level being the most important with an attribution score of 0.3287 for scenario 1 and 0.1995 for scenario 3. For both scenarios 1 and 3, multiple soil temperatures were also assigned attribution scores above .08. For scenario 1 the second highest score reported in training was assigned to 50-cm temperature at 0.1416 and scenario 3 reported the second highest score as 20-cm temperature at 0.1858. The remaining top five variables of influence for both scenarios were also soil profile data. Scenario 2 returned surface temperature as the most influential variable in training. The attribution scores for each of the scenarios are summarized in Table 4.2. These results show the importance of understanding soil dynamics, when accurately determining discharge characteristics from heterogenous karst systems and incorporating the time lag associated with soil layers. By representing the moisture levels and temperature at the different depths within the soil profile, the variable activation time of the different soil layers within the soil matrix and macropores is represented which directly determines the flow contributions from that depth.

Results of our model support a growing body of evidence that representing vertical variability of soil moisture is important for predicting karst hydrologic

variability, but also suggests the importance of soil temperature. Recent studies have used machine learning approaches to represent the impact of spatial and vertical variability of soil moisture in karst hydrologic predictions. Ollivier et al. (2020) reported NSE values between 0.88 and 0.92 using a distributed-reservoir model that employed a form on neural network known as multifactorial modeling to estimate spatial variability within the soil reservoir. Wunsch et al (2021) reported NSE values of 0.73 and 0.87 for a Convolution Neural Network modeling approach where volumetric water content at four different levels within the soil column were used to generate flow predictions and showed improved modeling ability when compared to the results from models not including the soil moisture variability. Similar to our study, both of these studies provided vastly improved NSE values as compared to reservoir-style modeling approaches that are commonly employed (Tritz et al., 2011; Tzoraki and Nikolaidis, 2007; Husic et al., 2019). Unique to our study was the highlighted importance of soil temperature, which was found to have a prominent influence on hydrologic predictions based on the IG analysis. The importance of the soil temperature in the attribution scores may be associated with improved representation of mixing of various sources of water, given water temperature can be used as a tracer when delineating flow components in a karst watershed (Doucette and Peterson, 2014; Kurylyk et al., 2017). Alternatively, this finding may suggest that temperature is an important regulator in matrix-macropore interaction, which has been highlighted recently in frozen soils (Mohammed et al., 2018). Cumulatively these findings highlight the utility of machine learning methods to predict karst hydrologic processes and suggest further work is needed to determine the physical mechanisms governing soil temperature impacts on flowrate.

4.2.2 Nitrate concentration ELM modeling

Results for the four nitrate modeling scenarios outlined in Table 3.1 also highlighted the importance of accounting for soil moisture variability in predicting nitrate concentration dynamics in the karst agroecosystem watershed (Table 4.1; Figure 4.5). The Nash-Sutcliffe Efficiency (NSE) for scenario 3 (which focused on only atmospheric parameters) were found to provide the poorest predictions of nitrate concentration, with NSEs for model runs falling between 0.3630 and 0.3924 and averaging 0.3820. Visually, the results show the TELM represents the general trends across the seasons, with an average increase during the wetter winter month when baseflow is elevated and an average decrease during the summer months when baseflow is reduced. This scenario does not perform well when capturing the short-term dynamics within the seasons and storm events, reducing its viability for expanded application. Conversely, the model results from scenarios 1, 2 and 4 (which included soil moisture and temperature parameters) indicated improved ability to reflect within event and daily variability in nitrate concentrations (Figures 4.5a-b,d). Visually, these model scenarios predict both the large increases in nitrate concentration seen during the seasonal flushing events and the short-term event dynamics that many models have difficulty capturing. They also appear to capture the extremes with decent accuracy, especially scenario 4. Further, Nash-Sutcliff values for scenarios 1,2 and 4 were 2-3-fold greater, with averages of 0.92, 0.89, and 0.94, respectively. Moriasi et al. (2015) also outlined ranges to interpret NSE for nitrogen predictions at the watershed scale at a monthly time step, with $0.65 < NSE \leq 1$ being considered very good, $0.50 < NSE \leq 0.65$ being good, $0.35 < NSE \leq 0.50$ being satisfactory, and below 0.35 being not satisfactory; however, it is often suggested that

ranges should be relaxed for higher frequency measurements. These findings therefore suggest exceptional performance of the model for Scenarios 1, 2 and 4 considering the 15-minute model evaluation timestep, and the high temporal variability in the concentrations at the watershed outlet.

Results from the integrated gradients analysis suggested high importance of soil moisture variables, moderate influence of atmospheric variables, and limited impact of fertilization variables in model training (Table 4.2). For the three scenarios that included soil parameters in training, all returned combinations of the soil variables being the most impactful on training for nitrate. For scenarios 1 and 2, the soil moisture at 50-cm was returned as the most influential parameter, receiving a score of 0.2151 and 0.2291, respectively. Scenario 4 returned the soil moisture at 20-cm to be the most influential variable in training. Scenario 3, which excluded both soil moisture and fertilizer from training and evaluation, returned surface temp as the most influential variable in training. Interestingly, the three types of fertilization data included in scenario 1 were ranked as three of the four least important variables in model training, with precipitation being the fourth. Their scores were inorganic fertilizer 0.00054, swine fertilizer 0.00028, precipitation 0.00011, and dairy fertilizer 0.00010. The attribution scores for each scenario training to nitrate are summarized in Table 4.2.

The results from the different scenarios' performance and the IG analysis show the model captures the variability in the hydrologic connectivity and the variability of nitrate source composition in the various soil layers. The soil moisture and temperatures at various depths within the soil profile received the highest attribution scores in scenarios 1, 2, and 4. As described with the visual comparison and flowrate results, the

soil moisture and temperature at the various levels drive the overall discharge from the watershed due to the connection between the different layers of the soil profile with the macropores and karst features, which has a strong influence on the nitrate loading. This underscores the importance of hydrologic source connectivity of soil sources to the watershed nitrate concentrations. Further, several studies have linked the importance of soil temperature and moisture to nitrogen mineralization rates within the soil (De Neve et al., 2003; Guntinas et al., 2012; Miller and Geisseler, 2018) indicating these properties strongly regulate the microbial processes governing nitrate composition in the soil layers. The IG results indicate the TELM is accounting for the time-varying impacts of both connectivity and upland biochemical processes.

Our findings suggest fertilization in agricultural practices had limited impact on nitrate concentrations which likely reflect the low application rates of both inorganic and organic fertilizers within the study watershed, although legacy N contributions are likely important. Roughly 150 ha of the more than 1000 ha watershed are dedicated to row crop production, with most of the watershed being used for pasture/grazing which might explain why limited impact of nitrate-based fertilizers were observed during the events and why the IG analysis was not significant. While the organic fertilizers did not provide a direct source of nitrate, they likely contributed to legacy contributions. These legacy contributions have been reported to persist for several decades, with nearly 30% of total applied organic N still residing in soil organic matter or leaking into the hydrosphere over a 30-year period (Sebilo et al., 2013). The IG analysis showed that near surface temperatures and soil moisture were important for nitrate concentration predictions (even

moreso than for flowrate), which could reflect the sensitivity of mineralization of legacy N in these layers upper soil layers.

4.2.3 Overfitting Analysis

The results of the overfitting (OF) scenarios show the scenarios including all available data are not overfit due to redundant variables present in training and evaluation. When comparing the NSEs for the nitrate overfitting scenarios, scenario 1 had a value of 0.3820, scenario 2 had a value of 0.9028, and scenario 3 had a value of 0.9569. The discharge OF scenario 1 had an NSE value of 0.1551, scenario 2 had an NSE value of 0.6351, and scenario 3 had an NSE value of 0.9382 (). These NSEs are consistent with the initial analysis looking at the effect of the different input parameters on model performance which shows the inclusion of a large set of possibly redundant variables did not improve model performance due to overfitting. This also further illustrates the importance of representing the vertical variability within the soil profile. By excluding the atmospheric variables, the complexity of the model is reduced, decreasing the processing demand and time of training, while also not impacting model performance because of the heavy importance seen in representing the vertical variability within the soil profile to understanding flow and nitrate export dynamics.

4.3   Capturing Hysteresis and In-stream Process Dynamics

A hysteresis index was generated for eleven events between 2019 and 2021 using the observed flow and prediction results from nitrate scenarios 2, and nine events using the observed flow and predicted results from scenario 4 (Table 4.3; Figure 4.7). Scenario 1 was excluded from the hysteresis analysis because the addition of fertilization data

showed little impact in improving NSE values and the attribution scores showed it carried the least impact in model training. For the eleven observed events, all hysteresis indices were calculated as negative and fell between -0.2035 and -0.6340, with the average HI being -0.3914 (Table 4.3a-c). Scenario 2 resulted in the small fall and small spring events having positive HI and the nine other events negative HI, ranging from -0.5231 to 0.3193 (Table 4.3a). For scenario 3, the HI for the small spring and small and medium summer events were positive, with the rest being negative, and all HI ranged between -0.4380 and 0.1276 (Table 4.3b). For the nine events generated for scenario 4, the HI values were all negative and fell between -0.5654 and -0.1881, with the average being -0.3331, which is compared to an average observed HI for the nine events of -0.4132 (Table 4.3c). This means the difference between the average observed HI and average predicted HI for scenario 2 was 0.2881, for scenario 3 was 0.2358, and for scenario 4 was 0.0801. The hysteresis loops were also generated for the measured nitrate, scenario 2 predicted nitrate, and scenario 4 predicted nitrate (Figures 4.6) to better understand how well the TELM modeled in event dynamics and timing. Clear improvement in modeling these dynamics was seen for seven of the nine events that were modeled between scenario 2 and 4. This improvement is especially visible in the December 20-21, 2020 and May 4-5, 2021 events. For the December event, scenario 2 shows a clockwise hysteresis with concentration increases early in the event, leveling off during most of the rising limb, and slowly decreasing during the falling limb of the hydrograph. Scenario 4 more closely tracks the observed trends, with slightly overpredicting but mirroring the trends for most of the rising limb. It also predicts an increase in concentration resulting in a negative hysteresis index, like what was observed. For the May event, both scenarios and the

57

observed hysteresis indices were negative, and the rising limbs of both the scenario predictions showcased similar magnitude and trends. Scenario 4 did show more accurate predictions for the falling limb, tracking the trends of the observed falling limb with higher accuracy than scenario 2. These comparisons show the improved rain event prediction performance with the inclusion of the 100-cm soil condition data and further underscore the importance of soil moisture and temperature variability when understanding nitrate dynamics in karst systems.

Diurnal variations were also visually compared between the measured nitrate concentrations and modeled nitrate concentrations for scenarios 2 and 4 and highlighted the importance of 100 cm soil moisture data to successfully capture diurnal variation in the nitrate signal (Figure 4.7). These figures show Scenario 4 generally provides better representation than scenario 2, particularly during the summer months when aquatic vegetation is recognized to have prominent impact on N (Bunnell et al., 2020). Figure 4.7e shows this difference between the scenarios well, with scenario 4 tracking both timing and magnitude of the variations with much greater accuracy than scenario 2 during summer. During the winter months, both scenarios appear to predict some diurnal variability that was not observed in the measured data; however, these variations are small in comparison to the summer months. These findings emphasize that the model generally captures time-varying in-stream process dynamics.

Through the hysteresis analysis and assessment of diurnal variations, the TELM shows good performance at modeling cumulative watershed processes that impact N fluxes in the karst agroecosystem. The hysteresis patterns are well represented because time lags associated with hydrologic connectivity of soil layers is well represented in

input data layers. The diel variability is likely well represented because of the representation of soil water temperature as well as atmospheric conditions which are governing inputs to deterministic models of in-stream N cycle models (Bunnell et al., 2020; Ford et al., 2017). Specifically, inclusion of soil water temperature at 100 cm was likely more reflective of ambient surface water temperatures and thus improved the diurnal predictions in Scenario 4 as compared to Scenario 2. This analysis also emphasized the importance of accounting for hysteresis analysis in model performance, as traditional metrics such as NSE did not show major differences between model scenarios 1,2, and 4 for the nitrate ELM modeling analysis. While studies have previously emphasized the importance of hysteresis in model evaluation in future studies (Liu et al., 2021), few studies have also suggested quantitative metrics for diel variations associated with in-stream processes. Quantitative metrics such as those presented for riverine nitrate uptake in Yang et al. (2019) may also be beneficial to include in calibration and optimization routines in future work.

4.4   Implications of findings for modeling nitrate exports in karst agroecosystems

This study highlighted the effectiveness of machine learning, specifically the extreme learning machine, at modeling hydrologic and hydro-chemical fluxes in complex systems like karst agroecosystems. Using accepted metrics like Nash-Sutcliffe Efficiency and hysteretic patterns, this study showed the two-hidden-layer extreme learning machine variant was able to model the system complexity with high accuracy. The hysteresis analysis showed the TELM also performed well when assessing the short-term rain event predictions when the time lag associated with variable soil moisture layer responses was

represented in the training data; however, poor performance of hysteretic patterns was observed when this time lag was not captured in the training data, which may create issues in data sparse regions where only atmospheric variables are available. In the absence of soil moisture data, recent innovations have suggested time lags between input and response variables can be represented using transformations and decomposition of input and response variable signal including approaches such as wavelet transforms (Barzegar et al. 2017), particle swarm optimization (Zhu et al., 2020; Surahki, 2021), or empirical mode decomposition (Prasad et al., 2018). For instance, Prasad et al., 2018 employed a hybrid ELM integrated with ensemble empirical mode decomposition to forecast upper and lower layer soil moisture using meteorological data (solar radiation, precipitation, minimum and maximum daily temperatures) along with continental parameter maps (albedo, soil characteristics, and seasonality of vegetation), reporting an R^2 of 0.966 between the observed and predicted soil moisture. An adaptation to the ELM that incorporates one of these methods could prove to be an effective tool in developing models that can accurately represent and predict the nitrate exports when soil moisture data is lacking, or sparse, and thus serve as a predictive tool.

The findings of this study highlight the importance of inclusion of soil moisture variability for representing nitrate exports in process-based or conceptual modeling frameworks. The results show regions of the soil profile below the effective root zone can play a substantial role in nitrate loading, and in some case can be the region of the soil that dominates the loading. Existing modeling approaches for water quality simulations in karst utilize reservoir-style models that lump the entire soil matrix or the soil matrix and epikarst into a single reservoir (e.g., Husic et al., 2019). Our findings suggest that root

zone, and deeper soil moisture dynamics (and subsequent matrix-macropore exchange), should be more robustly represented given the gradients observed in nitrate concentrations between these zones and throughout the year. This may be accomplished through incorporating more process-based, distributed models of soil hydrologic and biochemical processes at the watershed-scale (e.g., SWAT) with reservoir models often used to represent epikarst and phreatic zones in karst hydrologic and water quality models. Alternatively, more discretization of reservoirs for the soil layer (e.g., surface, root zone, and deeper layers) may be sufficient, and would significantly reduce parameterization requirements over spatially distributed models such as SWAT.

Given the importance of nitrate loading from deeper portions of the soil layer, our results support that treatment strategies at springheads and headwater tributaries are likely needed to decrease downstream nitrate contributions. Treatment strategies could include the construction of pools and wetlands at the spring outlets that slow the flow to allow for sites of high nitrogen uptake and denitrification. Small, slower moving pools that allow for the growth of vegetation like duckweed or floating aquatic macrophytes (Bunnell et al., 2020) may provide a suitable location for high nitrogen removal, but this is only an effective strategy during the warmer months. To control the bulk of the nitrate loading, measures to address the contributions seen during the winter months must be implemented to handle the seasonal flushing that occurs during the periods of elevated soil water content, when there is a reconnection of the deeper soil matrix with the macropores and karst network in these agroecosystems. At the very least, these findings indicate treatment strategies should be implemented alongside improved management practices. Through this combined approach, the legacy nitrate that is present within the

deeper reaches of the soil profile can be buffered and removed from the surface waters, while application is regulated at a responsible level to promote crop growth while not increasing the levels retained within the deep soils.

4.5 Tables and Figures

Table 4.1: The three scenarios used to test the ELMs ability to model the study system using different sets of variables.

Scenario	Inputs	Response Variable	NSE
1	Atmospheric; Soil Data at 10, 20, and 50 cm; Fertilization data	NO_3	0.9196
2	Atmospheric; Soil Data at 10, 20, and 50 cm	NO_3	0.8851
3	Atmospheric	NO_3	0.3820
4	Atmospheric; Soil Data at 10, 20, 50, and 100 cm	NO_3	0.9363
1	Atmospheric; Soil Data at 10, 20, and 50 cm	Discharge	0.6519
2	Atmospheric	Discharge	0.1551
3	Atmospheric; Soil Data at 10, 20, 50, and 100 cm	Discharge	0.9328

Table 4.2: The average attribution values assigned to each of the variables used in the tested scenarios. Each set represents the averaged results from at least three runs of the specified scenario for both the nitrate and discharge models.

Attributions for Nitrate Models

Scenario	Variable	IG
Scenario 1	Avg Soil Mstr 50-cm	0.2151
	50-cm Temp	0.1861
	20-cm Temp	0.1651
	10-cm Temp	0.1336
	Avg Soil Mstr 10-cm	0.0865
	Avg Soil Mstr 20-cm	0.0700
	Air Temp	0.0632
	Sur Temp	0.0427
	Avg Rel Hum	0.0191
	Sol Rad	0.0100
	1.5m Wind Speed	0.0075
	lbs inorganic N	0.0005
	Swine Gallons	0.0003
	Precip	0.0001
	Dairy Gallons	0.0001
Scenario 2	Avg Soil Mstr 50-cm	0.2291
	20-cm Temp	0.2079
	50-cm Temp	0.1724
	Avg Soil Mstr 10-cm	0.0846
	Air Temp	0.0720
	Avg Soil Mstr 20-cm	0.0719
	Sur Temp	0.0626
	10-cm Temp	0.0573
	Avg Rel Hum	0.0271
	1.5m Wind Speed	0.0108
	Sol Rad	0.0041
	Precip	0.0001
Scenario 3	Sur Temp	0.4936
	Avg Rel Hum	0.2367
	Air Temp	0.1676
	Sol Rad	0.0815
	1.5m Wind Speed	0.0206
	Precip	0.0001
Scenario 4	Avg Soil Mstr 20-cm	0.1610
	20-cm Temp	0.1349
	Avg Soil Mstr 10-cm	0.1175
	100-cm Temp	0.1099
	10-cm Temp	0.1018
	Avg Soil Mstr 100-cm	0.0791
	Avg Soil Mstr 50-cm	0.0647
	Sur Temp	0.0637
	Air Temp	0.0532
	Avg Rel Hum	0.0479
	50-cm Temp	0.0293
	Sol Rad	0.0190
	1.5m Wind Speed	0.0177
	Precip	0.0004

Attributions for Discharge Models

Scenario	Variable	IG
Scenario 1	Avg Soil Mstr 50-cm	0.3287
	50-cm Temp	0.1416
	Avg Soil Mstr 10-cm	0.1053
	20-cm Temp	0.0950
	Avg Soil Mstr 20-cm	0.0860
	Air Temp	0.0800
	10-cm Temp	0.0579
	Sur Temp	0.0397
	Avg Rel Hum	0.0365
	1.5m Wind Speed	0.0186
	Sol Rad	0.0107
	Precip	0.0002
Scenario 2	Sur Temp	0.5163
	1.5m Wind Speed	0.2196
	Avg Rel Hum	0.1400
	Air Temp	0.0809
	Sol Rad	0.0425
	Precip	0.0008
Scenario 3	Soil Mstr 50-cm	0.1995
	20-cm Temp	0.1858
	Soil Mstr 100-cm	0.1177
	50-cm Temp	0.0983
	10-cm Temp	0.0868
	Sur Temp	0.0738
	Soil Mstr 20-cm	0.0573
	Rel Hum	0.0524
	Air Temp	0.0401
	Avg Soil Mstr 10-cm	0.0309
	100-cm Temp	0.0257
	Sol Rad	0.0208
	1.5m Wind Speed	0.0106
	Precip	0.0002

Table 4.3: The Nash-Sutcliffe Efficiencies of the three scenarios used to test overfitting within the ELM.

Scenario	Inputs	Response Variable	NSE
OF 1	Atmospheric	NO_3	0.3820
OF 2	Soil Data at 10, 20, and 50 cm	NO_3	0.9028
OF 3	Soil Data at 10, 20, 50, and 100 cm	NO_3	0.9569
OF 1	Atmospheric	Discharge	0.1551
OF 2	Soil Data at 10, 20, and 50 cm	Discharge	0.6351
OF 3	Soil Data at 10, 20, 50, and 100 cm	Discharge	0.9382

Table 4.4: a) The results for the hysteresis analysis for a) Scenario 2 and b) Scenario 4.

a) Rain Event Hysteresis Scenario 2							
Season	Size	Start Date	End Date	Max Q (cms)	Predicted HI	Observed HI	Difference
Summer	Small	7/29/2020	8/9/2020	0.18	-0.1209	-0.6340	0.5131
	Med	7/3/2019	7/13/2019	0.4013	-0.0472	-0.3827	0.3355
	Large	None	None	None	None	None	None
Fall	Small	12/19/2020	12/23/2020	0.14	0.3193	-0.5484	0.8677
	Med	10/28/2020	11/10/2020	0.357	-0.5231	-0.2602	0.2629
	Large	10/30/2019	11/7/2019	1.85	-0.2021	-0.2035	0.0015
Winter	Small	2/10/2021	2/21/2021	0.2796	-0.1547	-0.2292	0.0745
	Med	1/30/2021	2/10/2021	0.843	-0.1888	-0.4100	0.2212
	Large	2/27/2021	3/14/2021	2.76	-0.0142	-0.3130	0.2988
Spring	Small	4/23/2021	4/29/2021	0.081355	0.1172	-0.3342	0.4514
	Med	5/2/2021	5/22/2021	0.756	-0.1607	-0.3957	0.2350
	Large	6/6/2021	6/13/2021	1.53	-0.1607	-0.5944	0.4338
				Average	-0.1033	-0.3914	0.2881

b) Rain Event Hysteresis Scenario 4							
Season	Size	Start Date	End Date	Max Q (cms)	Predicted HI	Observed HI	Difference
Summer	Small	7/29/2020	8/9/2020	0.18	-0.2626	-0.6340	0.3714
	Med	7/3/2019	7/13/2019	0.4013	None	None	None
	Large	None	None	None	None	None	None
Fall	Small	12/19/2020	12/23/2020	0.14	-0.4575	-0.5484	0.0909
	Med	10/28/2020	11/10/2020	0.357	-0.5654	-0.2602	0.3051
	Large	10/30/2019	11/7/2019	1.85	None	None	None
Winter	Small	2/10/2021	2/21/2021	0.2796	-0.3111	-0.2292	0.0819
	Med	1/30/2021	2/10/2021	0.843	-0.4013	-0.4100	0.0087
	Large	2/27/2021	3/14/2021	2.76	-0.3493	-0.3130	0.0363
Spring	Small	4/23/2021	4/29/2021	0.081355	-0.2098	-0.3342	0.1245
	Med	5/2/2021	5/22/2021	0.756	-0.2529	-0.3957	0.1428
	Large	6/6/2021	6/13/2021	1.53	-0.1881	-0.5944	0.4063
				Average	-0.3331	-0.4132	0.0801
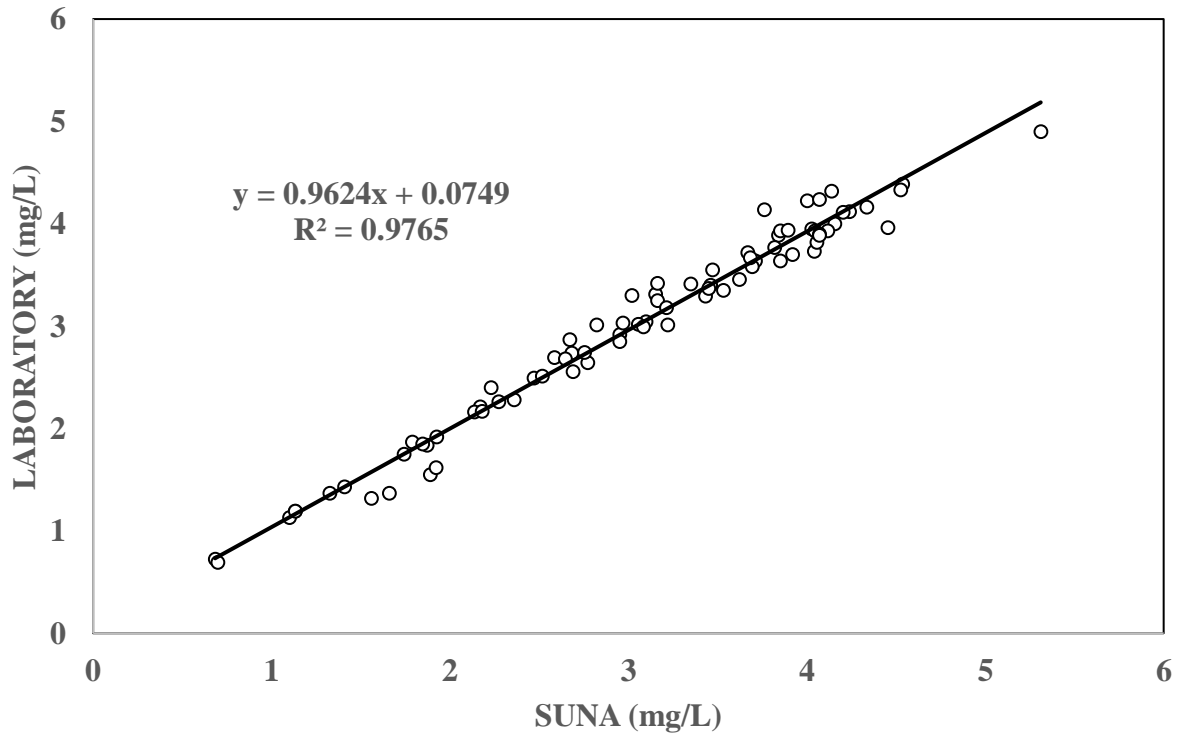
Figure 4.1: Linear regression comparison of laboratory measurements of grab samples and the observed SUNA V2 nitrate measurements for all samples.
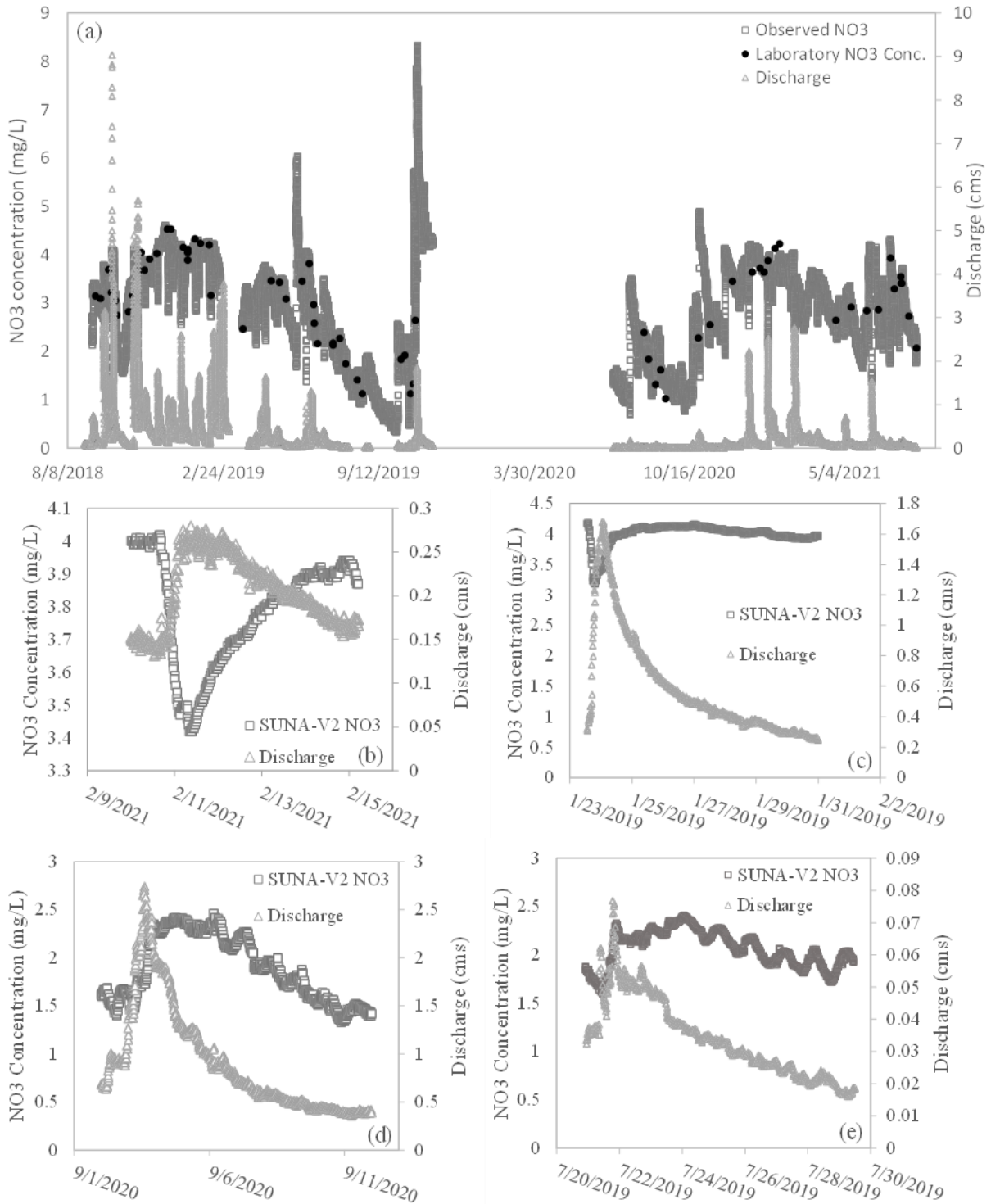
Figure 4.2: a) Timeseries for measured nitrate and discharge at the watershed outlet from Aug 29, 2018 through Aug 4, 2021. Storm events and subsequent recessions are provided for typical events in winter on b) Feb 10-11, 2021, and c) Jan 23-24, 2019. Storm events and subsequent recessions are also provided for typical events in summer on d) Sept 2-3, 2020 and e) July 21-22, 2019.
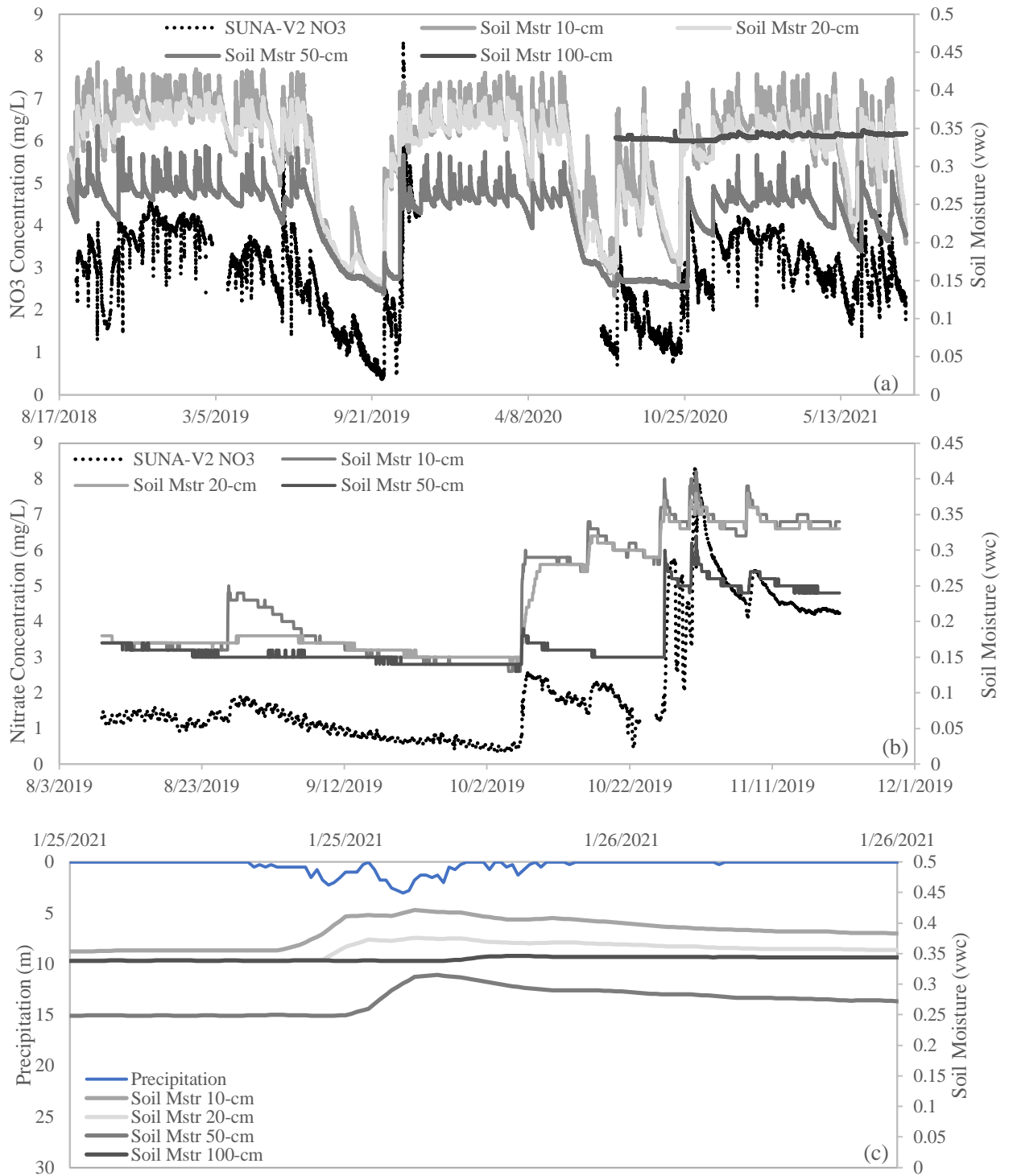
Figure 4.3: a) Measured nitrate concentrations are plotted against the volumetric water content measured at four different depths within the soil profile (10, 20, 50, and 100-cm) throughout the monitoring period of Aug 29, 2018 through Aug 4, 2021. b) Period from Aug 7 to Nov 20, 2019 is emphasized to demonstrate varied temporal response of soil moisture with depth and the associated impacts on nitrate concentrations. **c)** Rain event on Jan 25-26, 2021 showing the activation of the various layers within the soil profile and the time lag associated with this activation during a rain event.
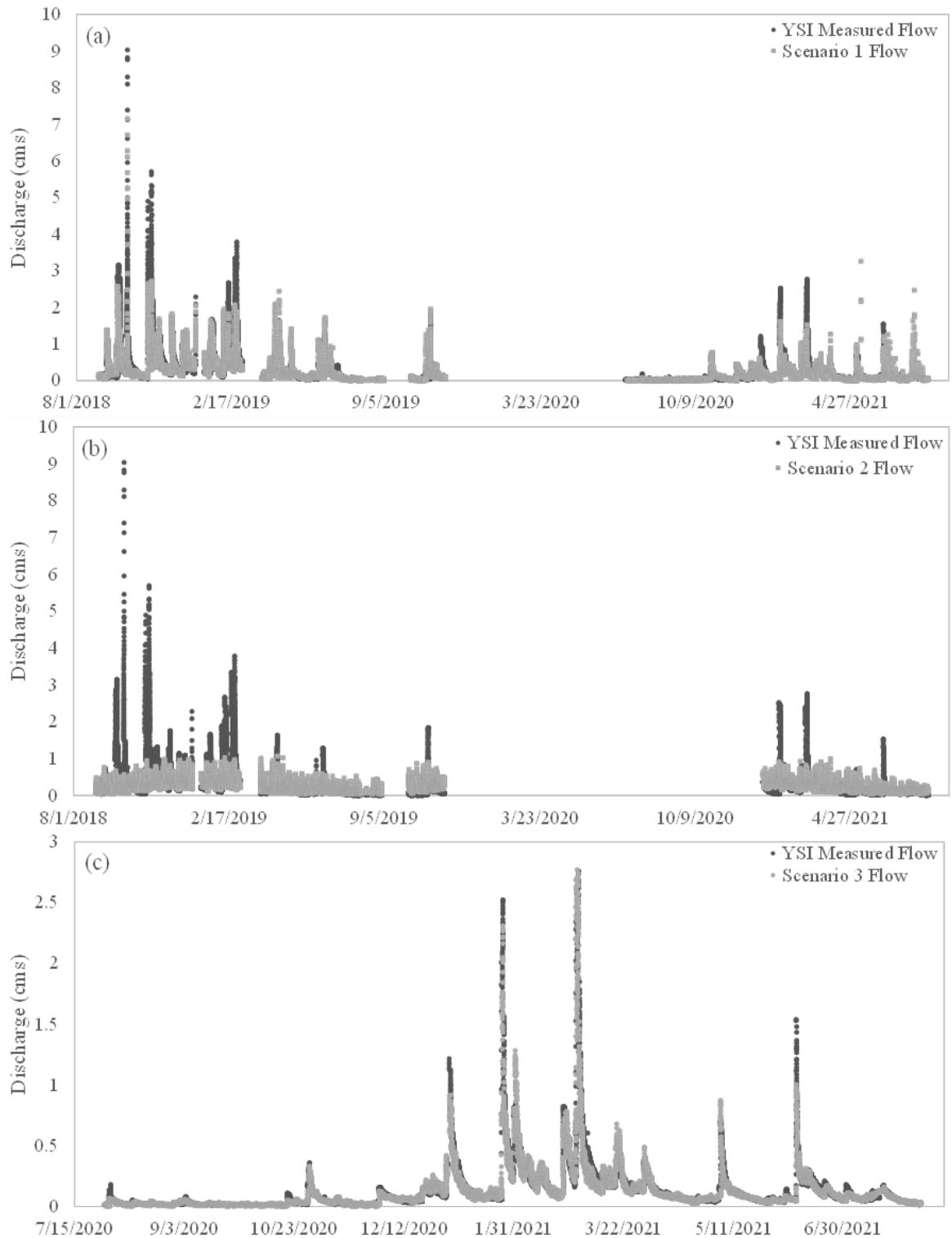
Figure 4.4: Timeseries of the measured vs. predicted flow measurements for the three input parameter scenarios, a) showing scenario 1 predictions, b) scenario 2 predictions, and c) scenario 3 predictions. Note scenario 3 falls within a shorter time period (July 29, 2020 through Aug 4, 2021).
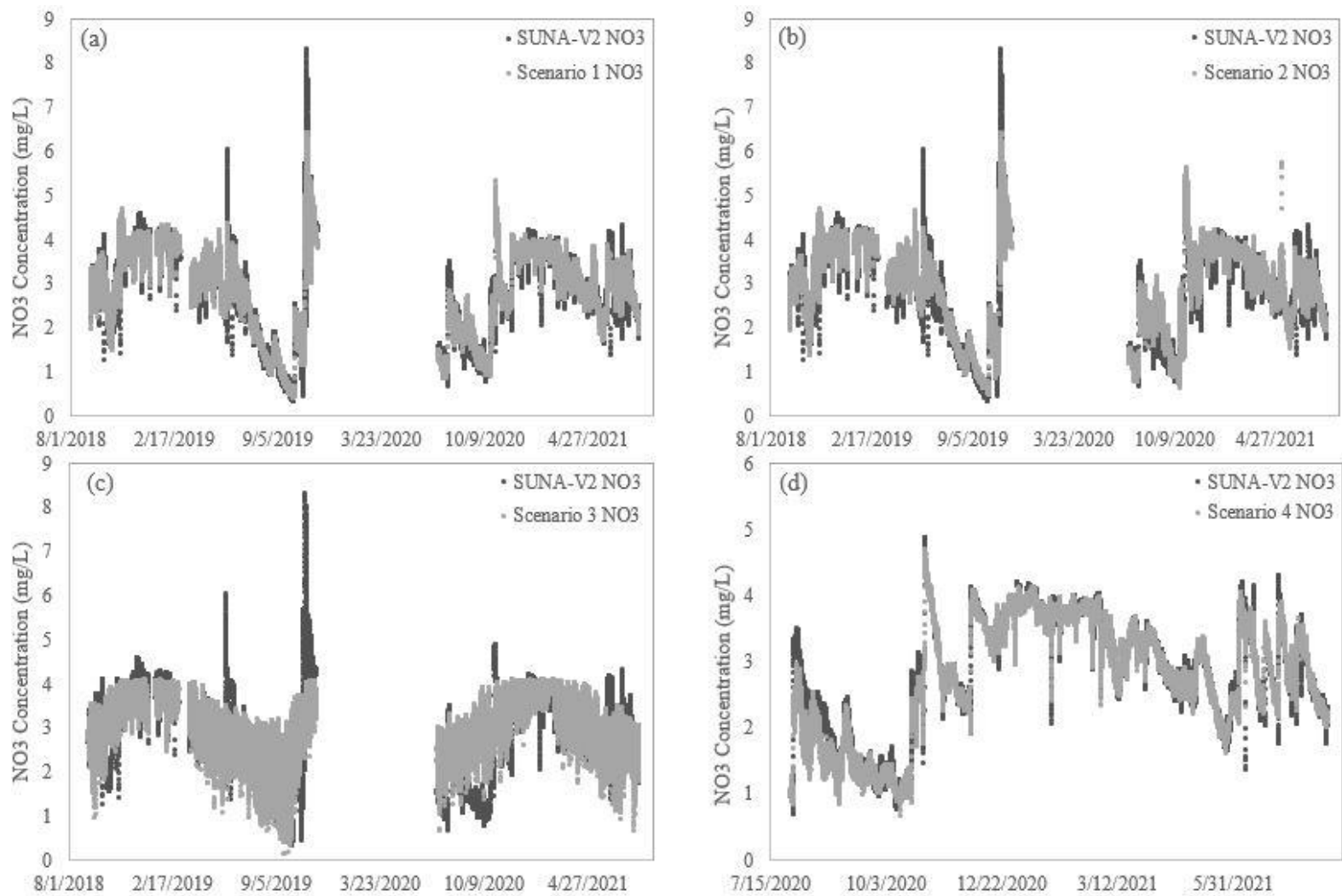
Figure 4.5: Timeseries of the measured vs. predicted nitrate concentration for the four input parameter scenarios, showing a) scenario 1 predictions, b) scenario 2 predictions, c) scenario 3 predictions, and d) scenario 4 predictions. Note scenario 4 falls within a shorter time period (July 29, 2020 through Aug 4, 2021).
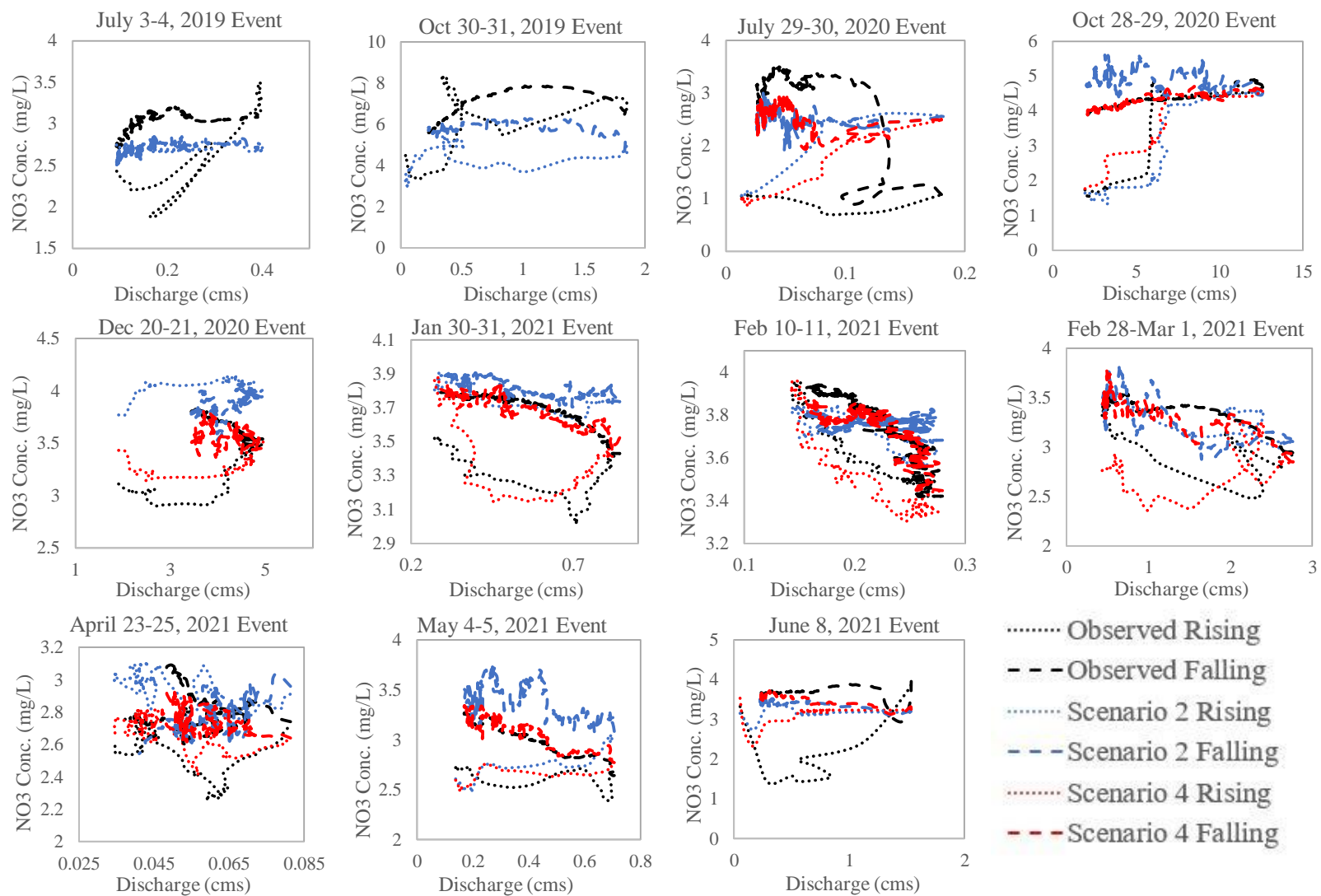
Figure 4.6: Hysteresis loops for the eleven rain events chosen for the hysteresis comparison. Note, only nine events occurred during the period included for scenario 4.
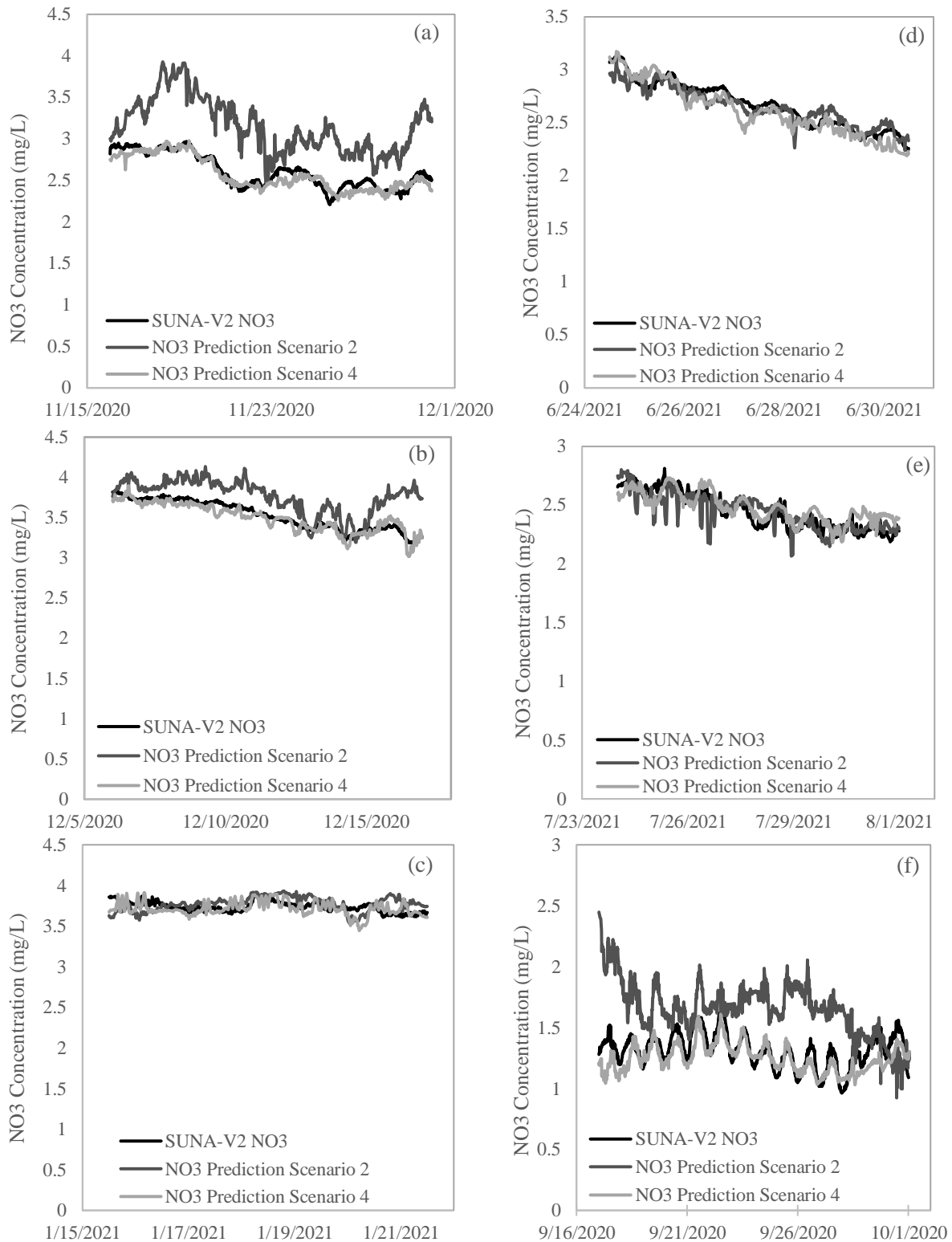
Figure 4.7: Comparison of the measured and predicted in-stream diurnal variations in nitrate concentration from scenarios 2 and 4 for periods following storm events in fall/winter and summer/early fall. Nov 16-29, 2020 (a); Dec 6-16, 2020 (b); Jan 16-21, 2021 (c); June 25-30, 2020 (d); July 24-31, 2021 (e); and Sept 17-30, 2020 (f).

CHAPTER 5. **CONCLUSIONS AND FUTURE WORK**

5.1   Conclusions

A two-hidden layer extreme learning machine was developed in this study using available libraries in Python from proven machine learning developers to assess the TELM's ability to model both flowrate and nitrate concentration exported from a heterogenous karst agroecosystem. The main conclusions are the following:

1. The TELM can successfully predict both flowrate and nitrate exports from these complex systems when the time lag associated with the soil conditions is appropriately represented in model training. Nash-Sutcliff efficiencies as high as 0.9328 for flow and 0.9363 for nitrate were observed when soil moisture and temperature at varying depths of the soil profile were included in training and evaluation show excellent effectiveness in the model's ability to capture flowrate and nitrate concentration.

2. The inclusion of deep soil profile moisture and temperature data (well below the effective root zone) in training and evaluating the TELM is important to accurately capturing the storm event and diurnal variations seen in the nitrate export signal in heterogenous karst agroecosystems. When 100-cm soil moisture and temperature data was included in training and evaluation (along with 10-cm, 20-cm, and 50-cm) the TELM successfully captured timing and magnitude of diurnal signals and storm event hysteresis indices for multiple periods evaluated.

3. In well-managed agroecosystems, fertilization inputs may not represent the main driver of nitrate exports. N stored within the soil matrix from past upland management may be a larger factor in nitrate exports than newly applied fertilizers. This can have reaching implications in adjusting nutrient loading management strategies to take a coupled

approach of treating fluvial exports, focusing on removal of excess nutrient through the construction of wetlands, while also regulating upland fertilizer application to levels that meet crop demand without over applying.

5.2   Future Work

While the result of this research provided insight into the importance of understanding how the variability within the soil matrix controls the flowrate and discharge from karst agroecosystems, more research is needed to fully understand aspects of the findings and build upon the work. The following recommendations stem from the findings.

1. Develop and implement new methods to process atmospheric input data to represent the time lag associated with the soil matrix buffering surface conditions. The methodology used in this research could be more widely applied if an effective technique for processing or transforming the climatological data collected by the NOAA maintained AWOS was implemented with some form of ELM. This would provide a much larger pool of data that could be used, in conjunction with in-situ nitrate and flow data, to elucidate trends in other watersheds and build predictive models to better understand loading from complex systems, whether karst or non-karst.

2. Applying these machine learning techniques in an agricultural karst watershed that experience higher rates of fertilization than that of the study watershed. One possible explanation for why the applied fertilizer data had such a low impact on model training is because the treated land only encompassed a small portion of the watershed. In more heavily fertilized watersheds, the export signal may experience a greater influence from the fertilizer application.

3. Apply these machine learning models to both hindcasts and future-casts to see trends in past nitrate loading and predict what loading trends may look like in relation to future climate projects. Using these models in conjunction with other predictive models used in future climate and landcover scenarios may aid in assessing the potential impacts of nitrate exports in the future.

4. Implementation of new management strategies focusing on treating spring exports for excess nutrients may be a more effective control on excess loading that upland management for agroecosystems that are well regulated in fertilizer inputs.

CHAPTER 6. APPENDIX

Appendix A: Periods of missing data during the monitoring period.

Data Type	Date Start Missing	Date End Missing	Complete Days Excluded	Date Included Start	Date Included End	Complete Days Included	Total
NO3	8/29/2018 12:00	9/7/2018 19:15	9.30	9/7/2018 19:30	2/19/2019 11:15	164.66	
	2/19/2019 11:30	3/20/2019 15:45	29.18	3/20/2019 16:00	10/23/2019 14:15	216.93	
	10/23/2019 14:30	10/25/2019 17:30	2.13	10/25/2019 17:45	11/20/2019 11:00	25.72	
	11/20/2019 11:15	7/10/2020 16:30	233.22	7/10/2020 16:45	2/2/2021 13:45	206.88	796.78
	2/2/2021 14:00	2/2/2021 14:45	0.03	2/2/2021 15:00	4/5/2021 12:45	61.91	
	4/5/2021 13:00	4/5/2021 13:45	0.03	4/5/2021 14:00	5/11/2021 16:00	36.08	
	5/11/2021 16:15	5/11/2021 18:00	0.07	5/11/2021 18:15	7/6/2021 11:00	55.70	
	7/6/2021 11:15	7/6/2021 11:30	0.01	7/6/2021 11:45	8/4/2021 9:45	28.92	

Data Type	Date Start Missing	Date End Missing	Complete Days Excluded	Date Included Start	Date Included End	Complete Days Included	Total
Discharge			0.00	8/29/2018 12:00	3/2/2019 15:15	185.14	
	3/2/2019 15:30	3/29/2019 12:30	26.87	3/29/2019 12:45	8/4/2019 18:15	128.23	
	8/4/2019 18:30	8/26/2019 6:45	21.51	8/26/2019 7:00	8/31/2019 22:45	5.66	
	8/31/2019 23:00	10/6/2019 19:45	35.86	10/6/2019 20:00	10/11/2019 7:45	4.49	
	10/11/2019 8:00	10/11/2019 21:00	0.54	10/11/2019 21:15	10/12/2019 11:00	0.57	921.46
	10/12/2019 11:15	10/16/2019 0:30	3.55	10/16/2019 0:45	10/19/2019 13:00	3.51	
	10/19/2019 13:15	10/21/2019 16:00	2.11	10/21/2019 16:15	10/22/2019 2:15	0.42	
	10/22/2019 2:30	10/22/2019 8:00	0.23	10/22/2019 8:15	10/24/2019 15:15	2.29	
	10/24/2019 15:30	10/26/2019 5:00	1.56	10/26/2019 5:15	4/3/2020 12:45	160.31	
	4/3/2020 13:00	5/30/2020 13:15	57.01	5/30/2020 13:30	8/4/2021 9:45	430.84	

Data Type	Date Start Missing	Date End Missing	Complete Days Excluded	Date Included Start	Date Included End	Complete Days Included	Total
Sp Cond			0.00	8/29/2018 12:00	3/2/2019 15:15	185.14	
	3/2/2019 15:30	3/29/2019 12:30	26.87	3/29/2019 12:45	4/3/2020 12:45	371.00	986.98
	4/3/2020 13:00	5/30/2020 13:15	57.01	5/30/2020 13:30	8/4/2021 9:45	430.84	

Data Type	Date Start Missing	Date End Missing	Complete Days Excluded	Date Included Start	Date Included End	Complete Days Included	Total
4 in Soil			0.00	8/29/2018 12:00	8/4/2021 9:45	1070.91	1070.91

Data Type	Date Start Missing	Date End Missing	Complete Days Excluded	Date Included Start	Date Included End	Complete Days Included	Total
8 in Soil			0.00	8/29/2018 12:00	8/4/2021 9:45	1070.91	1070.91

Data Type	Date Start Missing	Date End Missing	Complete Days Excluded	Date Included Start	Date Included End	Complete Days Included	Total
20 in Soil			0.00	8/29/2018 12:00	8/4/2021 9:45	1070.91	1070.91

Data Type	Date Start Missing	Date End Missing	Complete Days Excluded	Date Included Start	Date Included End	Complete Days Included	Total
40 in Soil	8/29/2018 12:00	6/30/2019 18:00	305.25	6/30/2019 18:15	8/4/2021 9:45	765.65	765.65

Data Type	Date Start	Date End Missing	Complete Days Excluded	Date Included Start	Date Included End	Complete Days Included	Total
4 in Soil Temp			0.00	8/29/2018 12:00	12/31/2018 19:45	124.32	
	12/31/2018 20:00	12/31/2018 23:00	0.13	12/31/2018 23:15	10/17/2019 7:00	289.32	1069.36
	10/17/2019 7:15	10/17/2019 12:00	0.20	10/17/2019 12:15	12/31/2020 19:00	441.28	
	12/31/2020 19:15	1/1/2021 23:00	1.16	1/1/2021 23:15	8/4/2021 9:45	214.44	

Data Type	Date Start Missing	Date End Missing	Complete Days Excluded	Date Included Start	Date Included End	Complete Days Included	Total
8 in Soil Temp			0.00	8/29/2018 12:00	12/31/2018 19:45	124.32	
	12/31/2018 20:00	12/31/2018 23:00	0.13	12/31/2018 23:15	10/17/2019 7:00	289.32	1069.36
	10/17/2019 7:15	10/17/2019 12:00	0.20	10/17/2019 12:15	12/31/2020 19:00	441.28	
	12/31/2020 19:15	1/1/2021 23:00	1.16	1/1/2021 23:15	8/4/2021 9:45	214.44	

Data Type	Date Start Missing	Date End Missing	Complete Days Excluded	Date Included Start	Date Included End	Complete Days Included	Total
20 in Soil Temp				8/29/2018 12:00	12/31/2018 19:45	124.32	
	12/31/2018 20:00	12/31/2018 23:00	0.13	12/31/2018 23:15	10/17/2019 7:00	289.32	1069.36
	10/17/2019 7:15	10/17/2019 12:00	0.20	10/17/2019 12:15	12/31/2020 19:00	441.28	
	12/31/2020 19:15	1/1/2021 23:00	1.16	1/1/2021 23:15	8/4/2021 9:45	214.44	

Data Type	Date Start Missing	Date End Missing	Complete Days Excluded	Date Included Start	Date Included End	Complete Days Included	Total
40 in Soil Temp			0.00	8/29/2018 12:00	7/16/2021 7:45	1051.82	1069.23
	7/16/2021 8:00	7/17/2021 23:45	1.66	7/18/2021 0:00	8/4/2021 9:45	17.41	

Data Type	Date Start Missing	Date End Missing	Complete Days Excluded	Date Included Start	Date Included End	Complete Days Included	Total
Solar Radiation			0.00	8/29/2018 12:00	8/4/2021 9:45	1070.91	1070.91

Data Type	Date Start Missing	Date End Missing	Complete Days Excluded	Date Included Start	Date Included End	Complete Days Included	Total
Relative Humidity			0.00	8/29/2018 12:00	12/31/2018 19:45	124.32	1069.36
	12/31/2018 20:00	12/31/2018 23:00	0.13	12/31/2018 23:15	10/17/2019 7:00	289.32	
	10/17/2019 7:15	10/17/2019 12:00	0.20	10/17/2019 12:15	12/31/2020 19:00	441.28	
	12/31/2020 19:15	1/1/2021 23:00	1.16	1/1/2021 23:15	8/4/2021 9:45	214.44	

Data Type	Date Start Missing	Date End Missing	Complete Days Excluded	Date Included Start	Date Included End	Complete Days Included	Total
Air Temp			0.00	8/29/2018 12:00	9/28/2018 11:30	29.98	1055.69
	9/28/2018 11:45	9/28/2018 11:45	0.00	9/28/2018 12:00	11/1/2018 11:00	33.96	
	11/1/2018 11:15	11/1/2018 12:00	0.03	11/1/2018 12:15	11/13/2018 6:00	11.74	
	11/13/2018 6:15	11/13/2018 7:00	0.03	11/13/2018 7:15	12/31/2018 19:00	48.49	
	12/31/2018 19:15	1/12/2019 23:45	12.19	1/13/2019 0:00	2/11/2019 8:00	29.33	
	2/11/2019 8:15	2/11/2019 9:00	0.03	2/11/2019 9:15	3/4/2019 12:00	21.11	
	3/4/2019 12:15	3/4/2019 13:00	0.03	3/4/2019 13:15	4/23/2019 12:00	49.95	
	4/23/2019 12:15	4/23/2019 13:00	0.03	4/23/2019 13:15	5/5/2019 8:00	11.78	
	5/5/2019 8:15	5/5/2019 9:00	0.03	5/5/2019 9:15	6/28/2019 19:00	54.41	
	6/28/2019 19:15	6/28/2019 20:00	0.03	6/28/2019 20:15	8/28/2019 8:00	60.49	
	8/28/2019 8:15	8/28/2019 8:15	0.00	8/28/2019 8:30	10/8/2019 9:30	41.04	
	10/8/2019 9:45	10/8/2019 10:00	0.01	10/8/2019 10:15	10/17/2019 7:00	8.86	
	10/17/2019 7:15	10/17/2019 12:00	0.20	10/17/2019 12:15	10/19/2019 7:00	1.78	
	10/19/2019 7:15	10/19/2019 8:00	0.03	10/19/2019 8:15	11/4/2019 15:00	16.28	
	11/4/2019 15:15	11/4/2019 16:00	0.03	11/4/2019 16:15	11/11/2019 8:00	6.66	
	11/11/2019 8:15	11/11/2019 9:00	0.03	11/11/2019 9:15	11/18/2019 2:00	6.70	
	11/18/2019 2:15	11/18/2019 3:00	0.03	11/18/2019 3:15	12/4/2019 10:00	16.28	
	12/4/2019 10:15	12/4/2019 11:00	0.03	12/4/2019 11:15	12/8/2019 8:00	3.86	
	12/8/2019 8:15	12/8/2019 9:00	0.03	12/8/2019 9:15	12/25/2019 11:00	17.07	
	12/25/2019 11:15	12/25/2019 12:00	0.03	12/25/2019 12:15	12/26/2019 13:00	1.03	
	12/26/2019 13:15	12/26/2019 14:00	0.03	12/26/2019 14:15	12/27/2019 8:00	0.74	
	12/27/2019 8:15	12/27/2019 9:00	0.03	12/27/2019 9:15	12/31/2019 19:00	4.41	
	12/31/2019 19:15	12/31/2019 23:45	0.19	1/1/2020 0:00	1/11/2020 21:00	10.87	
	1/11/2020 21:15	1/11/2020 22:00	0.03	1/11/2020 22:15	1/21/2020 9:00	9.45	

1/21/2020 9:15	1/21/2020 10:00	0.03	1/21/2020 10:15	1/25/2020 8:00	3.91
1/25/2020 8:15	1/25/2020 9:00	0.03	1/25/2020 9:15	2/10/2020 16:00	16.28
2/10/2020 16:15	2/10/2020 17:00	0.03	2/10/2020 17:15	3/11/2020 11:00	29.74
3/11/2020 11:15	3/11/2020 12:00	0.03	3/11/2020 12:15	4/22/2020 9:00	41.86
4/22/2020 9:15	4/22/2020 10:00	0.03	4/22/2020 10:15	4/27/2020 9:15	4.96
4/27/2020 9:30	4/27/2020 9:30	0.00	4/27/2020 9:45	6/9/2020 19:00	43.39
6/9/2020 19:15	6/9/2020 20:00	0.03	6/9/2020 20:15	6/26/2020 3:00	16.28
6/26/2020 3:15	6/26/2020 4:00	0.03	6/26/2020 4:15	7/6/2020 7:00	10.11
7/6/2020 7:15	7/6/2020 8:00	0.03	7/6/2020 8:15	8/15/2020 2:00	39.74
8/15/2020 2:15	8/15/2020 3:00	0.03	8/15/2020 3:15	9/30/2020 5:00	46.07
9/30/2020 5:15	9/30/2020 6:00	0.03	9/30/2020 6:15	11/19/2020 4:00	49.91
11/19/2020 4:15	11/19/2020 5:00	0.03	11/19/2020 5:15	12/5/2020 12:00	16.28
12/5/2020 12:15	12/5/2020 13:00	0.03	12/5/2020 13:15	12/12/2020 8:00	6.78
12/12/2020 8:15	12/12/2020 9:00	0.03	12/12/2020 9:15	12/13/2020 7:00	0.91
12/13/2020 7:15	12/13/2020 8:00	0.03	12/13/2020 8:15	12/31/2020 19:00	18.45
12/31/2020 19:15	12/31/2020 23:45	0.19	1/1/2021 0:00	1/7/2021 4:00	6.17
1/7/2021 4:15	1/7/2021 6:00	0.07	1/7/2021 6:15	1/20/2021 15:00	13.36
1/20/2021 15:15	1/20/2021 16:00	0.03	1/20/2021 16:15	2/5/2021 23:00	16.28
2/5/2021 23:15	2/6/2021 0:00	0.03	2/6/2021 0:15	3/17/2021 9:00	39.36
3/17/2021 9:15	3/17/2021 10:00	0.03	3/17/2021 10:15	3/27/2021 11:00	10.03
3/27/2021 11:15	3/27/2021 12:00	0.03	3/27/2021 12:15	3/27/2021 22:00	0.41
3/27/2021 22:15	3/27/2021 23:00	0.03	3/27/2021 23:15	4/7/2021 12:00	10.53
4/7/2021 12:15	4/7/2021 13:00	0.03	4/7/2021 13:15	4/23/2021 20:00	16.28
4/23/2021 20:15	4/23/2021 21:00	0.03	4/23/2021 21:15	5/16/2021 10:00	22.53
5/16/2021 10:15	5/16/2021 11:00	0.03	5/16/2021 11:15	6/29/2021 3:00	43.66
6/29/2021 3:15	6/29/2021 4:00	0.03	6/29/2021 4:15	7/15/2021 11:00	16.28
7/15/2021 11:15	7/15/2021 12:00	0.03	7/15/2021 12:15	7/21/2021 7:45	5.81
7/21/2021 8:00	7/21/2021 8:00	0.00	7/21/2021 8:15	7/28/2021 7:30	6.97
7/28/2021 7:45	7/28/2021 8:00	0.01	7/28/2021 8:15	8/4/2021 9:45	7.06

Data Type	Date Start Missing	Date End Missing	Complete Days Excluded	Date Included Start	Date Included End	Complete Days Included	Total
			0.00	8/29/2018 12:00	11/1/2018 11:00	63.96	
	11/1/2018 11:15	11/1/2018 12:00	0.03	11/1/2018 12:15	11/13/2018 6:00	11.74	
	11/13/2018 6:15	11/13/2018 7:00	0.03	11/13/2018 7:15	12/31/2018 19:00	48.49	
	12/31/2018 19:15	1/12/2019 23:45	12.19	1/13/2019 0:00	2/11/2019 8:00	29.33	
	2/11/2019 8:15	2/11/2019 9:00	0.03	2/11/2019 9:15	3/4/2019 12:00	21.11	
	3/4/2019 12:15	3/4/2019 13:00	0.03	3/4/2019 13:15	4/23/2019 12:00	49.95	
	4/23/2019 12:15	4/23/2019 13:00	0.03	4/23/2019 13:15	5/5/2019 8:00	11.78	
	5/5/2019 8:15	5/5/2019 9:00	0.03	5/5/2019 9:15	6/28/2019 19:00	54.41	
	6/28/2019 19:15	6/28/2019 20:00	0.03	6/28/2019 20:15	10/17/2019 7:00	110.45	
	10/17/2019 7:15	10/17/2019 12:00	0.20	10/17/2019 12:15	10/19/2019 7:00	1.78	
	10/19/2019 7:15	10/19/2019 8:00	0.03	10/19/2019 8:15	11/4/2019 15:00	16.28	
	11/4/2019 15:15	11/4/2019 16:00	0.03	11/4/2019 16:15	11/11/2019 8:00	6.66	
	11/11/2019 8:15	11/11/2019 9:00	0.03	11/11/2019 9:15	11/18/2019 2:00	6.70	
	11/18/2019 2:15	11/18/2019 3:00	0.03	11/18/2019 3:15	12/4/2019 10:00	16.28	
	12/4/2019 10:15	12/4/2019 11:00	0.03	12/4/2019 11:15	12/8/2019 8:00	3.86	
	12/8/2019 8:15	12/8/2019 9:00	0.03	12/8/2019 9:15	12/25/2019 11:00	17.07	
Surface Temp	12/25/2019 11:15	12/25/2019 12:00	0.03	12/25/2019 12:15	12/26/2019 13:00	1.03	1055.83
	12/26/2019 13:15	12/26/2019 14:00	0.03	12/26/2019 14:15	12/27/2019 8:00	0.74	
	12/27/2019 8:15	12/27/2019 9:00	0.03	12/27/2019 9:15	12/31/2019 19:00	4.41	
	12/31/2019 19:15	12/31/2019 23:45	0.19	1/1/2020 0:00	1/11/2020 21:00	10.87	
	1/11/2020 21:15	1/11/2020 22:00	0.03	1/11/2020 22:15	1/21/2020 9:00	9.45	
	1/21/2020 9:15	1/21/2020 10:00	0.03	1/21/2020 10:15	1/25/2020 8:00	3.91	
	1/25/2020 8:15	1/25/2020 9:00	0.03	1/25/2020 9:15	2/10/2020 16:00	16.28	
	2/10/2020 16:15	2/10/2020 17:00	0.03	2/10/2020 17:15	3/11/2020 11:00	29.74	
	3/11/2020 11:15	3/11/2020 12:00	0.03	3/11/2020 12:15	4/22/2020 9:00	41.86	
	4/22/2020 9:15	4/22/2020 10:00	0.03	4/22/2020 10:15	6/9/2020 19:00	48.36	
	6/9/2020 19:15	6/9/2020 20:00	0.03	6/9/2020 20:15	6/26/2020 3:00	16.28	
	6/26/2020 3:15	6/26/2020 4:00	0.03	6/26/2020 4:15	7/6/2020 7:00	10.11	
	7/6/2020 7:15	7/6/2020 8:00	0.03	7/6/2020 8:15	8/15/2020 2:00	39.74	
	8/15/2020 2:15	8/15/2020 3:00	0.03	8/15/2020 3:15	9/30/2020 5:00	46.07	
	9/30/2020 5:15	9/30/2020 6:00	0.03	9/30/2020 6:15	11/19/2020 4:00	49.91	
	11/19/2020 4:15	11/19/2020 5:00	0.03	11/19/2020 5:15	12/5/2020 12:00	16.28	
	12/5/2020 12:15	12/5/2020 13:00	0.03	12/5/2020 13:15	12/12/2020 8:00	6.78	
	12/12/2020 8:15	12/12/2020 9:00	0.03	12/12/2020 9:15	12/13/2020 7:00	0.91	
	12/13/2020 7:15	12/13/2020 8:00	0.03	12/13/2020 8:15	12/31/2020 19:00	18.45	

12/31/2020 19:15	12/31/2020 23:45	0.19	1/1/2021 0:00	1/7/2021 4:00	6.17
1/7/2021 4:15	1/7/2021 6:00	0.07	1/7/2021 6:15	1/20/2021 15:00	13.36
1/20/2021 15:15	1/20/2021 16:00	0.03	1/20/2021 16:15	2/5/2021 23:00	16.28
2/5/2021 23:15	2/6/2021 0:00	0.03	2/6/2021 0:15	3/17/2021 9:00	39.36
3/17/2021 9:15	3/17/2021 10:00	0.03	3/17/2021 10:15	3/27/2021 11:00	10.03
3/27/2021 11:15	3/27/2021 12:00	0.03	3/27/2021 12:15	3/27/2021 22:00	0.41
3/27/2021 22:15	3/27/2021 23:00	0.03	3/27/2021 23:15	4/7/2021 12:00	10.53
4/7/2021 12:15	4/7/2021 13:00	0.03	4/7/2021 13:15	4/23/2021 20:00	16.28
4/23/2021 20:15	4/23/2021 21:00	0.03	4/23/2021 21:15	5/16/2021 10:00	22.53
5/16/2021 10:15	5/16/2021 11:00	0.03	5/16/2021 11:15	6/29/2021 3:00	43.66
6/29/2021 3:15	6/29/2021 4:00	0.03	6/29/2021 4:15	7/15/2021 11:00	16.28
7/15/2021 11:15	7/15/2021 12:00	0.03	7/15/2021 12:15	8/4/2021 9:45	19.90

Data Type	Date Start Missing	Date End Missing	Complete Days Excluded	Date Included Start	Date Included End	Complete Days Included	Total
1.5m Wind Speed			0.00	8/29/2018 12:00	11/1/2018 11:00	63.96	
	11/1/2018 11:15	11/1/2018 12:00	0.03	11/1/2018 12:15	11/13/2018 6:00	11.74	
	11/13/2018 6:15	11/13/2018 7:00	0.03	11/13/2018 7:15	12/31/2018 19:00	48.49	
	12/31/2018 19:15	1/12/2019 23:45	12.19	1/13/2019 0:00	2/11/2019 8:00	29.33	
	2/11/2019 8:15	2/11/2019 9:00	0.03	2/11/2019 9:15	3/4/2019 12:00	21.11	
	3/4/2019 12:15	3/4/2019 13:00	0.03	3/4/2019 13:15	4/23/2019 12:00	49.95	
	4/23/2019 12:15	4/23/2019 13:00	0.03	4/23/2019 13:15	5/5/2019 8:00	11.78	
	5/5/2019 8:15	5/5/2019 9:00	0.03	5/5/2019 9:15	6/28/2019 19:00	54.41	
	6/28/2019 19:15	6/28/2019 20:00	0.03	6/28/2019 20:15	10/17/2019 7:00	110.45	
	10/17/2019 7:15	10/17/2019 12:00	0.20	10/17/2019 12:15	10/19/2019 7:00	1.78	1055.83
	10/19/2019 7:15	10/19/2019 8:00	0.03	10/19/2019 8:15	11/4/2019 15:00	16.28	
	11/4/2019 15:15	11/4/2019 16:00	0.03	11/4/2019 16:15	11/11/2019 8:00	6.66	
	11/11/2019 8:15	11/11/2019 9:00	0.03	11/11/2019 9:15	11/18/2019 2:00	6.70	
	11/18/2019 2:15	11/18/2019 3:00	0.03	11/18/2019 3:15	12/4/2019 10:00	16.28	
	12/4/2019 10:15	12/4/2019 11:00	0.03	12/4/2019 11:15	12/8/2019 8:00	3.86	
	12/8/2019 8:15	12/8/2019 9:00	0.03	12/8/2019 9:15	12/25/2019 11:00	17.07	
	12/25/2019 11:15	12/25/2019 12:00	0.03	12/25/2019 12:15	12/26/2019 13:00	1.03	
	12/26/2019 13:15	12/26/2019 14:00	0.03	12/26/2019 14:15	12/27/2019 8:00	0.74	
	12/27/2019 8:15	12/27/2019 9:00	0.03	12/27/2019 9:15	12/31/2019 19:00	4.41	
	12/31/2019 19:15	12/31/2019 23:45	0.19	1/1/2020 0:00	1/11/2020 21:00	10.87	
	1/11/2020 21:15	1/11/2020 22:00	0.03	1/11/2020 22:15	1/21/2020 9:00	9.45	

1/21/2020 9:15	1/21/2020 10:00	0.03	1/21/2020 10:15	1/25/2020 8:00	3.91
1/25/2020 8:15	1/25/2020 9:00	0.03	1/25/2020 9:15	2/10/2020 16:00	16.28
2/10/2020 16:15	2/10/2020 17:00	0.03	2/10/2020 17:15	3/11/2020 11:00	29.74
3/11/2020 11:15	3/11/2020 12:00	0.03	3/11/2020 12:15	4/22/2020 9:00	41.86
4/22/2020 9:15	4/22/2020 10:00	0.03	4/22/2020 10:15	6/9/2020 19:00	48.36
6/9/2020 19:15	6/9/2020 20:00	0.03	6/9/2020 20:15	6/26/2020 3:00	16.28
6/26/2020 3:15	6/26/2020 4:00	0.03	6/26/2020 4:15	7/6/2020 7:00	10.11
7/6/2020 7:15	7/6/2020 8:00	0.03	7/6/2020 8:15	8/15/2020 2:00	39.74
8/15/2020 2:15	8/15/2020 3:00	0.03	8/15/2020 3:15	9/30/2020 5:00	46.07
9/30/2020 5:15	9/30/2020 6:00	0.03	9/30/2020 6:15	11/19/2020 4:00	49.91
11/19/2020 4:15	11/19/2020 5:00	0.03	11/19/2020 5:15	12/5/2020 12:00	16.28
12/5/2020 12:15	12/5/2020 13:00	0.03	12/5/2020 13:15	12/12/2020 8:00	6.78
12/12/2020 8:15	12/12/2020 9:00	0.03	12/12/2020 9:15	12/13/2020 7:00	0.91
12/13/2020 7:15	12/13/2020 8:00	0.03	12/13/2020 8:15	12/31/2020 19:00	18.45
12/31/2020 19:15	12/31/2020 23:45	0.19	1/1/2021 0:00	1/7/2021 4:00	6.17
1/7/2021 4:15	1/7/2021 6:00	0.07	1/7/2021 6:15	1/20/2021 15:00	13.36
1/20/2021 15:15	1/20/2021 16:00	0.03	1/20/2021 16:15	2/5/2021 23:00	16.28
2/5/2021 23:15	2/6/2021 0:00	0.03	2/6/2021 0:15	3/17/2021 9:00	39.36
3/17/2021 9:15	3/17/2021 10:00	0.03	3/17/2021 10:15	3/27/2021 11:00	10.03
3/27/2021 11:15	3/27/2021 12:00	0.03	3/27/2021 12:15	3/27/2021 22:00	0.41
3/27/2021 22:15	3/27/2021 23:00	0.03	3/27/2021 23:15	4/7/2021 12:00	10.53
4/7/2021 12:15	4/7/2021 13:00	0.03	4/7/2021 13:15	4/23/2021 20:00	16.28
4/23/2021 20:15	4/23/2021 21:00	0.03	4/23/2021 21:15	5/16/2021 10:00	22.53
5/16/2021 10:15	5/16/2021 11:00	0.03	5/16/2021 11:15	6/29/2021 3:00	43.66
6/29/2021 3:15	6/29/2021 4:00	0.03	6/29/2021 4:15	7/15/2021 11:00	16.28
7/15/2021 11:15	7/15/2021 12:00	0.03	7/15/2021 12:15	8/4/2021 9:45	19.90

Data Type	Date Start Missing	Date End Missing	Complete Days Excluded	Date Included Start	Date Included End	Complete Days Included	Total
			0.00	8/29/2018 12:00	11/1/2018 11:00	63.96	
	11/1/2018 11:15	11/1/2018 13:00	0.07	11/1/2018 13:15	11/13/2018 6:00	11.70	
	11/13/2018 6:15	11/13/2018 8:00	0.07	11/13/2018 8:15	12/31/2018 23:45	48.65	
	1/1/2019 0:00	1/12/2019 23:45	11.99	1/13/2019 0:00	2/11/2019 8:00	29.33	
	2/11/2019 8:15	2/11/2019 10:00	0.07	2/11/2019 10:15	3/4/2019 12:00	21.07	
	3/4/2019 12:15	3/4/2019 14:00	0.07	3/4/2019 14:15	4/23/2019 12:00	49.91	
	4/23/2019 12:15	4/23/2019 14:00	0.07	4/23/2019 14:15	5/5/2019 8:00	11.74	
	5/5/2019 8:15	5/5/2019 10:00	0.07	5/5/2019 10:15	6/28/2019 19:00	54.36	
	6/28/2019 19:15	6/28/2019 21:00	0.07	6/28/2019 21:15	10/17/2019 7:00	110.41	
	10/17/2019 7:15	10/17/2019 12:00	0.20	10/17/2019 12:15	10/19/2019 7:00	1.78	
	10/19/2019 7:15	10/19/2019 9:00	0.07	10/19/2019 9:15	11/4/2019 15:00	16.24	
	11/4/2019 15:15	11/4/2019 17:00	0.07	11/4/2019 17:15	11/11/2019 8:00	6.61	
	11/11/2019 8:15	11/11/2019 10:00	0.07	11/11/2019 10:15	11/18/2019 2:00	6.66	
	11/18/2019 2:15	11/18/2019 4:00	0.07	11/18/2019 4:15	12/4/2019 10:00	16.24	
	12/4/2019 10:15	12/4/2019 12:00	0.07	12/4/2019 12:15	12/8/2019 8:00	3.82	
	12/8/2019 8:15	12/8/2019 10:00	0.07	12/8/2019 10:15	12/25/2019 11:00	17.03	
Precip	12/25/2019 11:15	12/25/2019 13:00	0.07	12/25/2019 13:15	12/26/2019 13:00	0.99	1055.84
	12/26/2019 13:15	12/26/2019 15:00	0.07	12/26/2019 15:15	12/27/2019 8:00	0.70	
	12/27/2019 8:15	12/27/2019 10:00	0.07	12/27/2019 10:15	1/11/2020 21:00	15.45	
	1/11/2020 21:15	1/11/2020 23:00	0.07	1/11/2020 23:15	1/21/2020 9:00	9.41	
	1/21/2020 9:15	1/21/2020 11:00	0.07	1/21/2020 11:15	1/25/2020 8:00	3.86	
	1/25/2020 8:15	1/25/2020 10:00	0.07	1/25/2020 10:15	2/10/2020 16:00	16.24	
	2/10/2020 16:15	2/10/2020 18:00	0.07	2/10/2020 18:15	3/11/2020 11:00	29.70	
	3/11/2020 11:15	3/11/2020 13:00	0.07	3/11/2020 13:15	4/22/2020 9:00	41.82	
	4/22/2020 9:15	4/22/2020 11:00	0.07	4/22/2020 11:15	6/9/2020 19:00	48.32	
	6/9/2020 19:15	6/9/2020 21:00	0.07	6/9/2020 21:15	6/26/2020 3:00	16.24	
	6/26/2020 3:15	6/26/2020 5:00	0.07	6/26/2020 5:15	7/6/2020 7:45	10.10	
	7/6/2020 8:00	7/6/2020 8:00	0.00	7/6/2020 8:15	8/15/2020 2:00	39.74	
	8/15/2020 2:15	8/15/2020 4:00	0.07	8/15/2020 4:15	9/30/2020 5:00	46.03	
	9/30/2020 5:15	9/30/2020 7:00	0.07	9/30/2020 7:15	11/19/2020 4:00	49.86	
	11/19/2020 4:15	11/19/2020 6:00	0.07	11/19/2020 6:15	12/5/2020 12:00	16.24	
	12/5/2020 12:15	12/5/2020 14:00	0.07	12/5/2020 14:15	12/12/2020 8:00	6.74	
	12/12/2020 8:15	12/12/2020 10:00	0.07	12/12/2020 10:15	12/13/2020 7:00	0.86	
	12/13/2020 7:15	12/13/2020 9:00	0.07	12/13/2020 9:15	8/4/2021 9:45	234.02	

Appendix B: Inorganic fertilizer applied to the watershed during the monitoring period.

Field Name	Task Start and End Dates	Partial, Full, or No Inclusion	Input Name	Area Applied (acres)	Area Applied (m²)	Portion of field on watershed	Rate Applied	Total Applied to full farm	Total Applied to Watershed		Pounds of nitrogen applied
LRC-CKF-J	27-Feb-19	Full	32-0-0 UAN	24.1	97527.4	1.000	10.19 gal/ac	245.50 gal	245.500	gal	867.302
LRC-CKF-K1	27-Feb-19	Full	32-0-0 UAN	49.9	201934.4	1.000	10.10 gal/ac	504.20 gal	504.200	gal	1781.238
LRC-CKF-R	27-Feb-19	No	32-0-0 UAN	7.8	31564.9	0.000	8.82 gal/ac	68.80 gal	0.000	gal	0.000
LRC-AS-Beef-Research Pastures	19-Mar-19	Partial	46-0-0 Urea	7.59	30715.1	0.748	108.00 lb/ac	0.41 ton	0.307	ton	257.725
LRC-AS-Beef-Research Pastures	19-Mar-19	Partial	46-0-0 Urea	7.49	30310.4	0.974	108.00 lb/ac	0.40 ton	0.390	ton	327.398
LRC-AS-Beef-Research Pastures	19-Mar-19	Full	46-0-0 Urea	7.42	30027.1	1.000	108.00 lb/ac	0.40 ton	0.400	ton	336.000
LRC-AS-Beef-Research Pastures	19-Mar-19	Full	46-0-0 Urea	7.61	30796.0	1.000	108.00 lb/ac	0.41 ton	0.410	ton	344.400
LRC-AS-Beef-Research	19-Mar-19	Partial	46-0-0 Urea	2.47	9995.5	0.835	108.00 lb/ac	0.13 ton	0.109	ton	91.155

Pastures											
LRC-AS-Beef-Research Pastures	19-Mar-19	Partial	46-0-0 Urea	2.53	10238.4	0.907	108.00 lb/ac	0.14 ton	0.127	ton	106.709
LRC-AS-Beef-Research Pastures	19-Mar-19	Partial	46-0-0 Urea	2.41	9752.7	0.984	108.00 lb/ac	0.13 ton	0.128	ton	107.458
LRC-AS-Beef-Research Pastures	19-Mar-19	Full	46-0-0 Urea	2.35	9509.9	1.000	108.00 lb/ac	0.13 ton	0.130	ton	109.200
LRC-AS-Beef-Research Pastures	19-Mar-19	Full	46-0-0 Urea	2.72	11007.2	1.000	108.00 lb/ac	0.15 ton	0.150	ton	126.000
LRC-AS-Beef-Research Pastures	19-Mar-19	Full	46-0-0 Urea	2.48	10036.0	1.000	108.00 lb/ac	0.13 ton	0.130	ton	109.200
LRC-AS-Beef-Research Pastures	19-Mar-19	Full	46-0-0 Urea	2.61	10562.1	1.000	108.00 lb/ac	0.14 ton	0.140	ton	117.600
LRC-AS-Beef-Research Pastures	19-Mar-19	Full	46-0-0 Urea	2.49	10076.5	1.000	108.00 lb/ac	0.13 ton	0.130	ton	109.200
LRC-AS-Beef-Research	19-Mar-19	Full	46-0-0 Urea	2.51	10157.4	1.000	108.00 lb/ac	0.14 ton	0.140	ton	117.600

Pastures											
LRC-AS-Beef-Research Pastures	19-Mar-19	Full	46-0-0 Urea	2.59	10481.2	1.000	108.00 lb/ac	0.14 ton	0.140	ton	117.600
LRC-AS-Beef-Research Pastures	19-Mar-19	Full	46-0-0 Urea	2.42	9793.2	1.000	108.00 lb/ac	0.13 ton	0.130	ton	109.200
LRC-AS-Beef-Research Pastures	19-Mar-19	Full	46-0-0 Urea	2.41	9752.7	1.000	108.00 lb/ac	0.13 ton	0.130	ton	109.200
LRC-AS-Beef-Research Pastures	19-Mar-19	Full	46-0-0 Urea	7.46	30189.0	1.000	108.00 lb/ac	0.40 ton	0.400	ton	336.000
LRC-AS-Beef-Research Pastures	19-Mar-19	Full	46-0-0 Urea	7.49	30310.4	1.000	108.00 lb/ac	0.40 ton	0.400	ton	336.000
LRC-CKF-J	22-Mar-19	Full	32-0-0 UAN	23.18	93804.4	1.000	10.36 gal/ac	240.10 gal	240.100	gal	852.451
LRC-CKF-K1	22-Mar-19	Full	32-0-0 UAN	50.67	205050.4	1.000	10.05 gal/ac	509.30 gal	509.300	gal	1808.219
LRC-CKF-R	22-Mar-19	No	32-0-0 UAN	7	28327.5	0.000	9.71 gal/ac	68.00 gal	0.000	gal	0.000
LRC-CKF-J	28-Mar-19	Full	32-0-0 UAN	24.52	99227.1	1.000	10.19 gal/ac	249.80 gal	249.800	gal	882.493
LRC-CKF-K1	28-Mar-19	Full	32-0-0 UAN	51.33	207721.3	1.000	10.09	517.90 gal	517.900	gal	1829.637

							gal/ac				
LRC-CKF-R	28-Mar-19	No	32-0-0 UAN	6.87	27801.4	0.000	9.74 gal/ac	66.90 gal	0.000	gal	0.000
LRC-AS-E	4-Apr-19	No	46-0-0 Urea	9.84	39820.3	0.000	108.70 lb/ac	0.53 ton	0.000	ton	0.000
LRC-AS-E	4-Apr-19	Partial	46-0-0 Urea	23.25	94087.7	0.038	108.70 lb/ac	1.26 ton	0.048	ton	40.671
LRC-AS-E	4-Apr-19	Partial	46-0-0 Urea	14.51	58718.8	0.153	108.70 lb/ac	0.79 ton	0.121	ton	101.792
LRC-AS-G	4-Apr-19	Partial	46-0-0 Urea	41.67	168629.4	0.902	108.70 lb/ac	2.26 ton	2.038	ton	1712.006
LRC-AS-Sheep-Lakebarn	4-Apr-19	Full	46-0-0 Urea	13	52608.2	1.000	163.04 lb/ac	1.06 ton	1.060	ton	890.400
LRC-CKF-I	4-Apr-19	Full	46-0-0 Urea	8.78	35530.7	1.000	163.04 lb/ac	0.72 ton	0.720	ton	604.800
LRC-CKF-I	4-Apr-19	Full	46-0-0 Urea	5.51	22297.8	1.000	163.04 lb/ac	0.45 ton	0.450	ton	378.000
LRC-CKF-Salad bowl	4-Apr-19	Full	46-0-0 Urea	7.59	30715.1	1.000	109.00 lb/ac	0.41 ton	0.410	ton	344.400
LRC-CKF-Uppercreek	4-Apr-19	Full	46-0-0 Urea	9.83	39779.9	1.000	163.04 lb/ac	0.80 ton	0.800	ton	672.000
LRC-Sheep-Desert	4-Apr-19	Full	46-0-0 Urea	2.57	10400.2	1.000	163.04 lb/ac	0.21 ton	0.210	ton	176.400
LRC-Sheep-Desert	4-Apr-19	Full	46-0-0 Urea	2.58	10440.7	1.000	163.04 lb/ac	0.21 ton	0.210	ton	176.400
LRC-Sheep-Desert	4-Apr-19	Full	46-0-0 Urea	2.5	10117.0	1.000	163.04 lb/ac	0.20 ton	0.200	ton	168.000

LRC-Sheep-Desert	4-Apr-19	Full	46-0-0 Urea	2.78	11250.1	1.000	163.04 lb/ac	0.23 ton	0.230	ton	193.200
LRC-Sheep-Desert	4-Apr-19	Full	46-0-0 Urea	2.95	11938.0	1.000	163.04 lb/ac	0.24 ton	0.240	ton	201.600
LRC-Sheep-Desert	4-Apr-19	Full	46-0-0 Urea	1.32	5341.8	1.000	163.04 lb/ac	0.11 ton	0.110	ton	92.400
LRC-Sheep-Desert	4-Apr-19	Full	46-0-0 Urea	1.43	5786.9	1.000	163.04 lb/ac	0.12 ton	0.120	ton	100.800
LRC-Sheep-Desert	4-Apr-19	Full	46-0-0 Urea	1.51	6110.6	1.000	163.04 lb/ac	0.12 ton	0.120	ton	100.800
LRC-Sheep-Desert	5-Apr-19	Full	46-0-0 Urea	1.84	7446.1	1.000	163.04 lb/ac	0.15 ton	0.150	ton	126.000
LRC-CKF-L	25-Apr-19	Full	46-0-0 Urea	38	153777.7	1.000	346.57 lb/ac	6.58 ton	6.580	ton	5527.200
LRC-CKF-L	25-Apr-19	Full	Agrotain Advanced	38	153777.7	1.000	0.36 qt/ac	3.46 gal	3.460	gal	0.000
LRC-CKF-R	29-Apr-19	Partial	46-0-0 Urea	32	129497.0	0.245	434.98 lb/ac	6.96 ton	1.707	ton	1433.817
LRC-CKF-R	29-Apr-19	Partial	Agrotain Advanced	32	129497.0	0.245	0.44 qt/ac	3.50 gal	0.858	gal	0.000
LRC-CKF-M	30-Apr-19	Full	46-0-0 Urea	27	109263.1	1.000	369.55 lb/ac	4.99 ton	4.990	ton	4191.600
LRC-CKF-M	30-Apr-19	Full	Agrotain Advanced	27	109263.1	1.000	0.37 qt/ac	2.51 gal	2.510	gal	0.000
LRC-CKF-P	1-May-19	Full	46-0-0 Urea	49.4	199911.0	1.000	360.08 lb/ac	8.89 ton	8.890	ton	7467.600
LRC-CKF-P	1-May-19	Full	Agrotain Advanced	49.4	199911.0	1.000	0.36 qt/ac	4.47 gal	4.470	gal	0.000

LRC-CKF-P	17-May-19	Full	46-0-0 Urea	49.4	199911.0	1.000	360.08 lb/ac	8.89 ton	8.890	ton	7467.600
LRC-CKF-P	17-May-19	Full	Agrotain Advanced	49.4	199911.0	1.000	0.36 qt/ac	4.47 gal	4.470	gal	0.000
LRC-CKF-M	21-May-19	Full	46-0-0 Urea	6.5	26304.1	1.000	347.23 lb/ac	1.13 ton	1.130	ton	949.200
LRC-CKF-M	21-May-19	Full	Agrotain Advanced	6.5	26304.1	1.000	0.35 qt/ac	0.57 gal	0.570	gal	0.000
LRC-CKF-M	21-May-19	Full	46-0-0 Urea	23	93076.0	1.000	347.23 lb/ac	3.99 ton	3.990	ton	3351.600
LRC-CKF-M	21-May-19	Full	Agrotain Advanced	23	93076.0	1.000	0.35 qt/ac	2.01 gal	2.010	gal	0.000
LRC-CKF-Q	21-May-19	Partial	46-0-0 Urea	19	76888.8	0.086	347.23 lb/ac	3.30 ton	0.285	ton	239.507
LRC-CKF-Q	21-May-19	Partial	Agrotain Advanced	19	76888.8	0.086	0.35 qt/ac	1.66 gal	0.143	gal	0.000
LRC-AS-Sheep-Lakebarn	14-Jun-19	Full	32-0-0 UAN	12.78	51717.9	1.000	10.10 gal/ac	129.08 gal	129.080	gal	454.775
LRC-CKF-K1	14-Jun-19	Full	32-0-0 UAN	4.03	16308.5	1.000	20.12 gal/ac	81.08 gal	81.080	gal	285.661
LRC-CKF-M	14-Jun-19	Full	32-0-0 UAN	0.99	4006.3	1.000	29.89 gal/ac	29.59 gal	29.590	gal	104.109
LRC-CKF-Uppercreek	14-Jun-19	Full	32-0-0 UAN	8.43	34114.4	1.000	10.20 gal/ac	85.99 gal	85.990	gal	302.960
LRC-J-Waterway	14-Jun-19	Full	32-0-0 UAN	5.31	21488.4	1.000	20.15 gal/ac	107.00 gal	107.000	gal	376.982
LRC-CKF-L	1-Mar-20	Full	32-0-0 UAN	34.93	141354.1	1.000	11.45	399.90 gal	399.900	gal	1412.767

							gal/ac				
LRC-CKF-M	1-Mar-20	Full	32-0-0 UAN	26.03	105337.7	1.000	10.04 gal/ac	261.40 gal	261.400	gal	923.474
LRC-CKF-M	1-Mar-20	Full	32-0-0 UAN	26.2	106025.7	1.000	10.08 gal/ac	264.00 gal	264.000	gal	932.659
LRC-CKF-P	1-Mar-20	Full	32-0-0 UAN	49.02	198373.2	1.000	10.06 gal/ac	492.90 gal	492.900	gal	1741.317
LRC-CKF-P	1-Mar-20	Full	32-0-0 UAN	49	198292.3	1.000	10.10 gal/ac	495.00 gal	495.000	gal	1751.904
LRC-CKF-L	5-Mar-20	Full	32-0-0 UAN	34.84	140989.8	1.000	10.59 gal/ac	368.90 gal	368.900	gal	1303.250
LRC-CKF-K	9-Mar-20	Full	32-0-0 UAN	29.64	119946.6	1.000	10.03 gal/ac	297.40 gal	297.400	gal	1050.655
LRC-CKF-K	9-Mar-20	Full	32-0-0 UAN	29.75	120391.7	1.000	10.04 gal/ac	298.60 gal	298.600	gal	1054.894
LRC-AS-Beef-Research Pastures	12-Mar-20	Partial	46-0-0 Urea	7.2	29136.8	0.748	108.69 lb/ac	0.39 ton	0.292	ton	245.153
LRC-AS-Beef-Research Pastures	12-Mar-20	Partial	46-0-0 Urea	7.24	29298.7	0.974	108.69 lb/ac	0.39 ton	0.380	ton	319.213
LRC-AS-Beef-Research Pastures	12-Mar-20	Full	46-0-0 Urea	6.86	27760.9	1.000	108.69 lb/ac	0.37 ton	0.370	ton	310.800
LRC-AS-Beef-Research	12-Mar-20	Full	46-0-0 Urea	7.22	29217.8	1.000	108.69 lb/ac	0.39 ton	0.390	ton	327.600

Pastures											
LRC-AS-Beef-Research Pastures	12-Mar-20	Partial	46-0-0 Urea	2.47	9995.5	0.835	108.69 lb/ac	0.13 ton	0.109	ton	91.155
LRC-AS-Beef-Research Pastures	12-Mar-20	Partial	46-0-0 Urea	2.53	10238.4	0.907	108.69 lb/ac	0.14 ton	0.127	ton	106.709
LRC-AS-Beef-Research Pastures	12-Mar-20	Partial	46-0-0 Urea	2.41	9752.7	0.984	108.69 lb/ac	0.13 ton	0.128	ton	107.458
LRC-AS-Beef-Research Pastures	12-Mar-20	Full	46-0-0 Urea	2.35	9509.9	1.000	108.69 lb/ac	0.13 ton	0.130	ton	109.200
LRC-AS-Beef-Research Pastures	12-Mar-20	Full	46-0-0 Urea	2.72	11007.2	1.000	108.69 lb/ac	0.15 ton	0.150	ton	126.000
LRC-AS-Beef-Research Pastures	12-Mar-20	Full	46-0-0 Urea	2.48	10036.0	1.000	108.69 lb/ac	0.13 ton	0.130	ton	109.200
LRC-AS-Beef-Research Pastures	12-Mar-20	Full	46-0-0 Urea	2.61	10562.1	1.000	108.69 lb/ac	0.14 ton	0.140	ton	117.600
LRC-AS-Beef-Research	12-Mar-20	Full	46-0-0 Urea	2.49	10076.5	1.000	108.69 lb/ac	0.14 ton	0.140	ton	117.600

Pastures											
LRC-AS-Beef-Research Pastures	12-Mar-20	Full	46-0-0 Urea	2.51	10157.4	1.000	108.69 lb/ac	0.14 ton	0.140	ton	117.600
LRC-AS-Beef-Research Pastures	12-Mar-20	Full	46-0-0 Urea	2.59	10481.2	1.000	108.69 lb/ac	0.14 ton	0.140	ton	117.600
LRC-AS-Beef-Research Pastures	12-Mar-20	Full	46-0-0 Urea	2.42	9793.2	1.000	108.69 lb/ac	0.13 ton	0.130	ton	109.200
LRC-AS-Beef-Research Pastures	12-Mar-20	Full	46-0-0 Urea	2.41	9752.7	1.000	108.69 lb/ac	0.13 ton	0.130	ton	109.200
LRC-AS-Beef-Research Pastures	12-Mar-20	Full	46-0-0 Urea	7.46	30189.0	1.000	108.69 lb/ac	0.41 ton	0.410	ton	344.400
LRC-AS-Beef-Research Pastures	12-Mar-20	Full	46-0-0 Urea	7.49	30310.4	1.000	108.69 lb/ac	0.41 ton	0.410	ton	344.400
LRC-AS-Sheep Barn Pastures	12-Mar-20	Full	46-0-0 Urea	2.83	11452.4	1.000	76.00 lb/ac	0.11 ton	0.110	ton	92.400
LRC-AS-Sheep Barn Pastures	12-Mar-20	Full	46-0-0 Urea	2.62	10602.6	1.000	76.00 lb/ac	0.10 ton	0.100	ton	84.000

LRC-AS-Sheep Barn Pastures	12-Mar-20	Full	46-0-0 Urea	2.49	10076.5	1.000	76.00 lb/ac	0.09 ton	0.090	ton	75.600
LRC-AS-Sheep Barn Pastures	12-Mar-20	Full	46-0-0 Urea	2.5	10117.0	1.000	76.00 lb/ac	0.10 ton	0.100	ton	84.000
LRC-AS-Sheep Barn Pastures	12-Mar-20	Full	46-0-0 Urea	2.54	10278.8	1.000	76.00 lb/ac	0.10 ton	0.100	ton	84.000
LRC-AS-Sheep Barn Pastures	12-Mar-20	Full	46-0-0 Urea	2.76	11169.1	1.000	76.00 lb/ac	0.10 ton	0.100	ton	84.000
LRC-AS-Sheep Barn Pastures	12-Mar-20	Full	46-0-0 Urea	2.33	9429.0	1.000	76.00 lb/ac	0.09 ton	0.090	ton	75.600
LRC-AS-Sheep Barn Pastures	12-Mar-20	Full	46-0-0 Urea	2.55	10319.3	1.000	76.00 lb/ac	0.10 ton	0.100	ton	84.000
LRC-AS-Sheep Barn Pastures	12-Mar-20	Full	46-0-0 Urea	2.39	9671.8	1.000	76.00 lb/ac	0.09 ton	0.090	ton	75.600
LRC-AS-Sheep Barn Pastures	12-Mar-20	Full	46-0-0 Urea	2.58	10440.7	1.000	76.00 lb/ac	0.10 ton	0.100	ton	84.000
LRC-AS-Sheep Barn Pastures	12-Mar-20	Full	46-0-0 Urea	3.43	13880.5	1.000	76.00 lb/ac	0.13 ton	0.130	ton	109.200
LRC-AS-E	16-Mar-20	No	46-0-0 Urea	12.12	49047.0	0.000	109.00 lb/ac	0.66 ton	0.000	ton	0.000
LRC-AS-E	16-Mar-20	Partial	46-0-0 Urea	23.25	94087.7	0.038	109.00	1.27 ton	0.049	ton	40.993

94

							lb/ac				
LRC-AS-G	16-Mar-20	Partial	46-0-0 Urea	41.67	168629.4	0.902	109.00 lb/ac	2.27 ton	2.047	ton	1719.582
LRC-AS-Sheep Barn Pastures	16-Mar-20	Full	46-0-0 Urea	2.94	11897.5	1.000	76.00 lb/ac	0.11 ton	0.110	ton	92.400
LRC-AS-Sheep Barn Pastures	16-Mar-20	Full	46-0-0 Urea	2.92	11816.6	1.000	109.00 lb/ac	0.16 ton	0.160	ton	134.400
LRC-AS-Sheep Barn Pastures	16-Mar-20	Full	46-0-0 Urea	2.86	11573.8	1.000	109.00 lb/ac	0.16 ton	0.160	ton	134.400
LRC-CKF-I	16-Mar-20	Full	46-0-0 Urea	8.78	35530.7	1.000	109.00 lb/ac	0.48 ton	0.480	ton	403.200
LRC-CKF-I	16-Mar-20	Full	46-0-0 Urea	5.51	22297.8	1.000	109.00 lb/ac	0.30 ton	0.300	ton	252.000
LRC-CKF-K1	16-Mar-20	Full	46-0-0 Urea	3.93	15903.8	1.000	109.00 lb/ac	0.21 ton	0.210	ton	176.400
LRC-CKF-Lake field	16-Mar-20	Full	46-0-0 Urea	4.67	18898.5	1.000	109.00 lb/ac	0.25 ton	0.250	ton	210.000
LRC-CKF-Lake hillside	16-Mar-20	Full	46-0-0 Urea	10	40467.8	1.000	109.00 lb/ac	0.54 ton	0.540	ton	453.600
LRC-CKF-M	16-Mar-20	Full	46-0-0 Urea	5.66	22904.8	1.000	109.00 lb/ac	0.31 ton	0.310	ton	260.400
LRC-CKF-Salad bowl	16-Mar-20	Full	46-0-0 Urea	7.59	30715.1	1.000	109.00 lb/ac	0.41 ton	0.410	ton	344.400
LRC-CKF-Springhouse	16-Mar-20	Full	46-0-0 Urea	3.55	14366.1	1.000	109.00 lb/ac	0.19 ton	0.190	ton	159.600

LRC-CKF-Uppercreek	16-Mar-20	Full	46-0-0 Urea	9.83	39779.9	1.000	109.00 lb/ac	0.54 ton	0.540	ton	453.600
LRC-J-Waterway	16-Mar-20	Full	46-0-0 Urea	7.17	29015.4	1.000	109.00 lb/ac	0.39 ton	0.390	ton	327.600
LRC-Sheep-Desert	16-Mar-20	Full	46-0-0 Urea	2.62	10602.6	1.000	109.00 lb/ac	0.14 ton	0.140	ton	117.600
LRC-Sheep-Desert	16-Mar-20	Full	46-0-0 Urea	2.57	10400.2	1.000	109.00 lb/ac	0.14 ton	0.140	ton	117.600
LRC-Sheep-Desert	16-Mar-20	Full	46-0-0 Urea	2.58	10440.7	1.000	109.00 lb/ac	0.14 ton	0.140	ton	117.600
LRC-Sheep-Desert	16-Mar-20	Full	46-0-0 Urea	2.5	10117.0	1.000	109.00 lb/ac	0.14 ton	0.140	ton	117.600
LRC-Sheep-Desert	16-Mar-20	Full	46-0-0 Urea	2.78	11250.1	1.000	109.00 lb/ac	0.15 ton	0.150	ton	126.000
LRC-Sheep-Desert	16-Mar-20	Full	46-0-0 Urea	2.95	11938.0	1.000	109.00 lb/ac	0.16 ton	0.160	ton	134.400
LRC-Sheep-Desert	16-Mar-20	Full	46-0-0 Urea	1.84	7446.1	1.000	109.00 lb/ac	0.10 ton	0.100	ton	84.000
LRC-Sheep-Desert	16-Mar-20	Full	46-0-0 Urea	1.32	5341.8	1.000	109.00 lb/ac	0.07 ton	0.070	ton	58.800
LRC-Sheep-Desert	16-Mar-20	Full	46-0-0 Urea	1.43	5786.9	1.000	109.00 lb/ac	0.08 ton	0.080	ton	67.200
LRC-Sheep-Desert	16-Mar-20	Full	46-0-0 Urea	1.51	6110.6	1.000	109.00 lb/ac	0.08 ton	0.080	ton	67.200
LRC-AS-G	18-Mar-20	Partial	32-0-0 UAN	38.05	153980.0	0.902	10.08 gal/ac	383.70 gal	346.027	gal	1228.533
LRC-VS-Big Field	18-Mar-20	Partial	46-0-0 Urea	16.41	66407.7	0.983	86.00 lb/ac	0.71 ton	0.698	ton	586.135

LRC-VS-Creek Field	18-Mar-20	Full	46-0-0 Urea	9.58	38768.2	1.000	86.00 lb/ac	0.41 ton	0.410	ton	344.400
LRC-VS-Shed Field	18-Mar-20	Partial	46-0-0 Urea	12.04	48723.2	0.970	86.00 lb/ac	0.52 ton	0.504	ton	423.565
LRC-CKF-L	3-Apr-20	Full	32-0-0 UAN	31.25	126461.9	1.000	10.07 gal/ac	314.80 gal	314.800	gal	1110.614
LRC-CKF-M	3-Apr-20	Full	32-0-0 UAN	26.32	106511.3	1.000	10.02 gal/ac	263.70 gal	263.700	gal	930.334
LRC-CKF-P	22-Apr-20	Full	32-0-0 UAN	49	198292.3	1.000	10.01 gal/ac	490.60 gal	490.600	gal	1730.837
LRC-CKF-K	12-May-20	Full	46-0-0 Urea	49.73	201246.4	1.000	347.39 lb/ac	8.64 ton	8.640	ton	7257.600
LRC-CKF-K	12-May-20	Full	Agrotain Advanced	49.73	201246.4	1.000	0.28 qt/ac	3.47 gal	3.470	gal	0.000
LRC-CKF-M	12-May-20	Full	46-0-0 Urea	6.4	25899.4	1.000	347.39 lb/ac	1.11 ton	1.110	ton	932.400
LRC-CKF-M	12-May-20	Full	Agrotain Advanced	6.4	25899.4	1.000	0.28 qt/ac	0.45 gal	0.450	gal	0.000
LRC-CKF-J	14-May-20	Full	46-0-0 Urea	24	97122.7	1.000	347.39 lb/ac	4.17 ton	4.170	ton	3502.800
LRC-CKF-J	14-May-20	Full	Agrotain Advanced	24	97122.7	1.000	0.28 qt/ac	1.68 gal	1.680	gal	0.000
LRC-CKF-K1	14-May-20	Full	46-0-0 Urea	49.13	198818.3	1.000	347.39 lb/ac	8.53 ton	8.530	ton	7165.200
LRC-CKF-K1	14-May-20	Full	Agrotain Advanced	49.13	198818.3	1.000	0.28 qt/ac	3.43 gal	3.430	gal	0.000
LRC-CKF-M	14-May-20	Full	46-0-0 Urea	6.4	25899.4	1.000	347.39 lb/ac	1.11 ton	1.110	ton	932.400

LRC-CKF-M	14-May-20	Full	Agrotain Advanced	6.4	25899.4	1.000	0.28 qt/ac	0.45 gal	0.450	gal	0.000
LRC-CKF-M	14-May-20	Full	46-0-0 Urea	25	101169.5	1.000	347.39 lb/ac	4.34 ton	4.340	ton	3645.600
LRC-CKF-M	14-May-20	Full	Agrotain Advanced	25	101169.5	1.000	0.28 qt/ac	1.75 gal	1.750	gal	0.000
LRC-CKF-Q	1-Jun-20	Partial	46-0-0 Urea	18	72842.1	0.086	347.39 lb/ac	3.13 ton	0.270	ton	227.168
LRC-CKF-Q	1-Jun-20	Partial	Agrotain Advanced	18	72842.1	0.086	0.28 qt/ac	1.26 gal	0.109	gal	0.000
LRC-CKF-R	2-Jun-20	No	46-0-0 Urea	9.24	37392.3	0.000	347.39 lb/ac	1.60 ton	0.000	ton	0.000
LRC-CKF-R	2-Jun-20	No	Agrotain Advanced	9.24	37392.3	0.000	0.28 qt/ac	0.65 gal	0.000	gal	0.000
LRC-CKF-R	4-Jun-20	Partial	46-0-0 Urea	31.6	127878.3	0.245	347.39 lb/ac	5.49 ton	1.346	ton	1130.985
LRC-CKF-R	4-Jun-20	Partial	Agrotain Advanced	31.6	127878.3	0.245	0.28 qt/ac	2.21 gal	0.542	gal	0.000
LRC-CKF-J	4-Mar-21	Full	32-0-0 UAN	22.6	91457.2	1.000	20.26 gal/ac	457.90 gal	457.900	gal	1615.471
LRC-CKF-M	4-Mar-21	Full	32-0-0 UAN	6.8	27518.1	1.000	20.28 gal/ac	137.90 gal	137.900	gal	487.173
LRC-CKF-M	4-Mar-21	Full	32-0-0 UAN	22.4	90647.9	1.000	20.19 gal/ac	452.20 gal	452.200	gal	1597.532
LRC-CKF-Q	4-Mar-21	Partial	32-0-0 UAN	17.7	71628.0	0.086	20.27 gal/ac	358.70 gal	30.992	gal	109.490
LRC-CKF-R	4-Mar-21	Partial	32-0-0 UAN	31.1	125854.9	0.245	20.27 gal/ac	630.50 gal	154.629	gal	546.273

LRC-CKF-R	4-Mar-21	No	32-0-0 UAN	6	24280.7	0.000	20.23 gal/ac	121.40 gal	0.000	gal	0.000
LRC-AS-Sheep Barn Pastures	18-Mar-21	Full	46-0-0 Urea	2.83	11452.4	1.000	76.00 lb/ac	0.11 ton	0.110	ton	92.400
LRC-AS-Sheep Barn Pastures	18-Mar-21	Full	46-0-0 Urea	2.97	12018.9	1.000	76.00 lb/ac	0.11 ton	0.110	ton	92.400
LRC-AS-Sheep Barn Pastures	18-Mar-21	Full	46-0-0 Urea	3.02	12221.3	1.000	76.00 lb/ac	0.11 ton	0.110	ton	92.400
LRC-AS-Sheep Barn Pastures	18-Mar-21	Full	46-0-0 Urea	2.92	11816.6	1.000	76.00 lb/ac	0.11 ton	0.110	ton	92.400
LRC-AS-Sheep Barn Pastures	18-Mar-21	Full	46-0-0 Urea	2.94	11897.5	1.000	76.00 lb/ac	0.11 ton	0.110	ton	92.400
LRC-AS-Sheep Barn Pastures	18-Mar-21	Full	46-0-0 Urea	3.28	13273.4	1.000	76.00 lb/ac	0.12 ton	0.120	ton	100.800
LRC-AS-Sheep Barn Pastures	18-Mar-21	Full	46-0-0 Urea	2.98	12059.4	1.000	76.00 lb/ac	0.11 ton	0.110	ton	92.400
LRC-AS-Sheep Barn Pastures	18-Mar-21	Full	46-0-0 Urea	3.03	12261.7	1.000	76.00 lb/ac	0.12 ton	0.120	ton	100.800
LRC-AS-Sheep Barn Pastures	18-Mar-21	Full	46-0-0 Urea	2.88	11654.7	1.000	76.00 lb/ac	0.11 ton	0.110	ton	92.400
LRC-AS-	18-Mar-21	Full	46-0-0 Urea	3	12140.3	1.000	76.00	0.11 ton	0.110	ton	92.400

							lb/ac				
Sheep Barn Pastures											
LRC-AS-Sheep Barn Pastures	18-Mar-21	Full	46-0-0 Urea	3.1	12545.0	1.000	76.00 lb/ac	0.12 ton	0.120	ton	100.800
LRC-AS-Sheep Barn Pastures	18-Mar-21	Full	46-0-0 Urea	3.2	12949.7	1.000	76.00 lb/ac	0.12 ton	0.120	ton	100.800
LRC-AS-Sheep Barn Pastures	18-Mar-21	Full	46-0-0 Urea	3.82	15458.7	1.000	76.00 lb/ac	0.15 ton	0.150	ton	126.000
LRC-CKF-Lake field	18-Mar-21	Full	46-0-0 Urea	4.67	18898.5	1.000	76.00 lb/ac	0.18 ton	0.180	ton	151.200
LRC-Sheep-Desert	18-Mar-21	Full	46-0-0 Urea	4.89	19788.8	1.000	76.00 lb/ac	0.19 ton	0.190	ton	159.600
LRC-Sheep-Desert	18-Mar-21	Full	46-0-0 Urea	2.62	10602.6	1.000	76.00 lb/ac	0.10 ton	0.100	ton	84.000
LRC-Sheep-Desert	18-Mar-21	Full	46-0-0 Urea	2.57	10400.2	1.000	76.00 lb/ac	0.10 ton	0.100	ton	84.000
LRC-Sheep-Desert	18-Mar-21	Full	46-0-0 Urea	2.58	10440.7	1.000	76.00 lb/ac	0.10 ton	0.100	ton	84.000
LRC-Sheep-Desert	18-Mar-21	Full	46-0-0 Urea	2.5	10117.0	1.000	76.00 lb/ac	0.09 ton	0.090	ton	75.600
LRC-Sheep-Desert	18-Mar-21	Full	46-0-0 Urea	2.78	11250.1	1.000	76.00 lb/ac	0.11 ton	0.110	ton	92.400
LRC-Sheep-Desert	18-Mar-21	Full	46-0-0 Urea	2.95	11938.0	1.000	76.00 lb/ac	0.11 ton	0.110	ton	92.400
LRC-Sheep-	18-Mar-21	Full	46-0-0 Urea	1.84	7446.1	1.000	76.00 lb/ac	0.07 ton	0.070	ton	58.800

Desert								lb/ac			
LRC-Sheep-Desert	18-Mar-21	Full	46-0-0 Urea	1.32	5341.8	1.000	76.00 lb/ac	0.05 ton	0.050	ton	42.000
LRC-Sheep-Desert	18-Mar-21	Full	46-0-0 Urea	1.43	5786.9	1.000	76.00 lb/ac	0.05 ton	0.050	ton	42.000
LRC-Sheep-Desert	18-Mar-21	Full	46-0-0 Urea	1.51	6110.6	1.000	76.00 lb/ac	0.06 ton	0.060	ton	50.400
LRC-AS-Beef-Research Pastures	22-Mar-21	Partial	46-0-0 Urea	7.59	30715.1	0.748	131.00 lb/ac	0.50 ton	0.374	ton	314.299
LRC-AS-Beef-Research Pastures	22-Mar-21	Partial	46-0-0 Urea	7.49	30310.4	0.974	131.00 lb/ac	0.49 ton	0.477	ton	401.062
LRC-AS-Beef-Research Pastures	22-Mar-21	Full	46-0-0 Urea	7.42	30027.1	1.000	131.00 lb/ac	0.49 ton	0.490	ton	411.600
LRC-AS-Beef-Research Pastures	22-Mar-21	Full	46-0-0 Urea	7.61	30796.0	1.000	131.00 lb/ac	0.50 ton	0.500	ton	420.000
LRC-AS-Beef-Research Pastures	23-Mar-21	Partial	46-0-0 Urea	7.48	30269.9	0.035	109.00 lb/ac	0.41 ton	0.015	ton	12.220
LRC-AS-Beef-Research	23-Mar-21	No	46-0-0 Urea	7.47	30229.5	0.000	109.00 lb/ac	0.41 ton	0.000	ton	0.000

Pastures											
LRC-AS-Beef-Research Pastures	23-Mar-21	Partial	46-0-0 Urea	7.67	31038.8	0.355	109.00 lb/ac	0.42 ton	0.149	ton	125.358
LRC-AS-Beef-Research Pastures	23-Mar-21	Full	46-0-0 Urea	7.46	30189.0	1.000	131.00 lb/ac	0.49 ton	0.490	ton	411.600
LRC-AS-Beef-Research Pastures	23-Mar-21	Full	46-0-0 Urea	7.49	30310.4	1.000	131.00 lb/ac	0.49 ton	0.490	ton	411.600
LRC-AS-Beef-Research Pastures	23-Mar-21	No	46-0-0 Urea	7.49	30310.4	0.000	109.00 lb/ac	0.41 ton	0.000	ton	0.000
LRC-AS-Beef-Research Pastures	23-Mar-21	No	46-0-0 Urea	7.43	30067.6	0.000	109.00 lb/ac	0.40 ton	0.000	ton	0.000
LRC-AS-E	23-Mar-21	Partial	46-0-0 Urea	15.22	61592.0	0.153	109.00 lb/ac	0.83 ton	0.127	ton	106.946
LRC-AS-G	23-Mar-21	Partial	46-0-0 Urea	41.67	168629.4	0.902	109.00 lb/ac	2.27 ton	2.047	ton	1719.582
LRC-AS-Sheep Barn Pastures	23-Mar-21	Full	46-0-0 Urea	3.18	12868.8	1.000	152.00 lb/ac	0.24 ton	0.240	ton	201.600
LRC-AS-Sheep Barn	23-Mar-21	Full	46-0-0 Urea	2.92	11816.6	1.000	152.00 lb/ac	0.22 ton	0.220	ton	184.800

Pastures											
LRC-AS-Sheep Barn Pastures	23-Mar-21	Full	46-0-0 Urea	2.86	11573.8	1.000	152.00 lb/ac	0.22 ton	0.220	ton	184.800
LRC-CKF-I	23-Mar-21	Full	46-0-0 Urea	8.78	35530.7	1.000	152.00 lb/ac	0.67 ton	0.670	ton	562.800
LRC-CKF-I	23-Mar-21	Full	46-0-0 Urea	5.51	22297.8	1.000	152.00 lb/ac	0.42 ton	0.420	ton	352.800
LRC-CKF-K1	23-Mar-21	Full	46-0-0 Urea	3.93	15903.8	1.000	109.00 lb/ac	0.21 ton	0.210	ton	176.400
LRC-CKF-Lake field	23-Mar-21	Full	46-0-0 Urea	4.67	18898.5	1.000	109.00 lb/ac	0.25 ton	0.250	ton	210.000
LRC-CKF-M	23-Mar-21	Full	46-0-0 Urea	5.66	22904.8	1.000	109.00 lb/ac	0.31 ton	0.310	ton	260.400
LRC-CKF-N	23-Mar-21	Full	46-0-0 Urea	24.21	97972.6	1.000	152.00 lb/ac	1.84 ton	1.840	ton	1545.600
LRC-CKF-P	23-Mar-21	Full	46-0-0 Urea	6.38	25818.5	1.000	152.00 lb/ac	0.48 ton	0.480	ton	403.200
LRC-CKF-R	23-Mar-21	Full	46-0-0 Urea	7.75	31362.6	1.000	152.00 lb/ac	0.59 ton	0.590	ton	495.600
LRC-CKF-Salad bowl	23-Mar-21	Full	46-0-0 Urea	7.59	30715.1	1.000	109.00 lb/ac	0.41 ton	0.410	ton	344.400
LRC-CKF-Uppercreek	23-Mar-21	Full	46-0-0 Urea	9.83	39779.9	1.000	152.00 lb/ac	0.75 ton	0.750	ton	630.000
LRC-J-Waterway	23-Mar-21	Full	46-0-0 Urea	7.17	29015.4	1.000	109.00 lb/ac	0.39 ton	0.390	ton	327.600
LRC-Sheep-Research	23-Mar-21	Full	46-0-0 Urea	1.42	5746.4	1.000	76.00 lb/ac	0.05 ton	0.050	ton	42.000

Pastures											
LRC-Sheep-Research Pastures	23-Mar-21	Full	46-0-0 Urea	1.27	5139.4	1.000	76.00 lb/ac	0.05 ton	0.050	ton	42.000
LRC-Sheep-Research Pastures	23-Mar-21	Full	46-0-0 Urea	1.32	5341.8	1.000	76.00 lb/ac	0.05 ton	0.050	ton	42.000
LRC-Sheep-Research Pastures	23-Mar-21	Full	46-0-0 Urea	1.27	5139.4	1.000	76.00 lb/ac	0.05 ton	0.050	ton	42.000
LRC-Sheep-Research Pastures	23-Mar-21	Full	46-0-0 Urea	1.31	5301.3	1.000	76.00 lb/ac	0.05 ton	0.050	ton	42.000
LRC-Sheep-Research Pastures	23-Mar-21	Full	46-0-0 Urea	1.34	5422.7	1.000	76.00 lb/ac	0.05 ton	0.050	ton	42.000
LRC-CKF-M	29-Mar-21	Full	32-0-0 UAN	6.85	27720.4	1.000	10.00 gal/ac	68.50 gal	68.500	gal	243.531
LRC-CKF-M	29-Mar-21	Full	32-0-0 UAN	22.9	92671.3	1.000	10.00 gal/ac	229.00 gal	229.000	gal	813.042
LRC-CKF-Q	29-Mar-21	Partial	32-0-0 UAN	17.7	71628.0	0.086	10.00 gal/ac	177.00 gal	15.293	gal	54.126
LRC-CKF-R	29-Mar-21	Partial	32-0-0 UAN	31.4	127068.9	0.245	10.00 gal/ac	314.00 gal	77.008	gal	273.039
LRC-CKF-R	29-Mar-21	No	32-0-0 UAN	5.85	23673.7	0.000	10.00 gal/ac	58.50 gal	0.000	gal	0.000
LRC-CKF-J	18-May-21	Full	46-0-0 Urea	23.18	93804.4	1.000	347.39 lb/ac	4.03 ton	4.030	ton	3385.200

LRC-CKF-J	18-May-21	Full	Agrotain Advanced	23.18	93804.4	1.000	0.28 qt/ac	1.62 gal	1.620	gal	0.000
LRC-CKF-L	18-May-21	Full	46-0-0 Urea	38	153777.7	1.000	347.39 lb/ac	6.60 ton	6.600	ton	5544.000
LRC-CKF-L	18-May-21	Full	Agrotain Advanced	38	153777.7	1.000	0.28 qt/ac	2.66 gal	2.660	gal	0.000
LRC-CKF-M	18-May-21	Full	46-0-0 Urea	26.9	108858.4	1.000	347.39 lb/ac	4.67 ton	4.670	ton	3922.800
LRC-CKF-M	18-May-21	Full	Agrotain Advanced	26.9	108858.4	1.000	0.28 qt/ac	1.88 gal	1.880	gal	0.000
LRC-CKF-P	18-May-21	Full	46-0-0 Urea	49.4	199911.0	1.000	347.39 lb/ac	8.58 ton	8.580	ton	7207.200
LRC-CKF-P	18-May-21	Full	Agrotain Advanced	49.4	199911.0	1.000	0.28 qt/ac	3.45 gal	3.450	gal	0.000

Appendix C: Organic fertilizer applied to the watershed during the monitoring period.

Swine

Date	Location Field	Acres	Application	Source	Start Depth	Stop Depth	Gallons
3/8/2018	P	48	One Injected	Tank 2	14.9	10.5	88140
10/4/2018	P	48	One Injected	Tank 2	10.5	6.2	86468
10/5/2018	P	48	One Injected	Tank 2	6.2	2.5	74928
10/23/2018	K	53	One Injected	Tank 1/Tank 2	19	15	160538
10/24/2018	K	53	One Injected	Tank1/Tank 2	15	10	200224
10/25/2018	K	53	One Injected	Tank 1/Tank 2	10	5.9	164942
4/11/2019	K	53	One Injected	Tank1/Tank 2	16.2	13.2	121400
7/24/2019	Beef 24	7.62	One irrigated	Tank 3	16.7	15.7	21328
7/25/2019	Beef 24	7.62	One irrigated	Tank 3	15.7	13.9	36114
7/26/2019	Beef 24	7.62	One irrigated	Tank 3	13.9	11.1	56732
7/28/2019	Beef 24	7.62	One irrigated	Tank 3	11.1	8.2	58467
7/30/2019	Beef 24	7.62	One irrigated	Tank 3	8.2	5.8	48011
7/31/2019	Beef 24	7.62	One irrigated	Tank 3	5.8	3.8	40981
8/23/2019	H	27.12	One irrigated	Tank1/Tank 2	16.3	10	252242

8/29/2019	H	27.12	One irrigated	Tank1/Tank 2	13.3	10	132160
9/4/2019	H	27.12	One irrigated	Tank1/Tank 2	10	8.5	61840
9/12/2019	H	27.12	One irrigated	Tank1/Tank 2	8.5	7.2	53440
9/17/2019	H	27.12	One irrigated	Tank1/Tank 2	7.2	5.3	88720
9/18/2019	H	27.12	One irrigated	Tank1/Tank 2	5.3	3.8	60440
9/22/2019	H	27.12	One irrigated	Tank1/Tank 2	4.2	2.9	52230
9/26/2019	H	27.12	One irrigated	Tank1/Tank 2	5.9	3.8	84188
4/8/2020	R	32	One Injected	Tank1/Tank 2	17.9	16.5	57422
4/9/2020	R	32	One Injected	Tank1/Tank 2	16.5	14.4	84166
5/8/2020	R	32	One Injected	Tank1/Tank 2	14.4	10.3	165329
5/13/2020	R	32	One Injected	Tank1/Tank 2	10.3	5.3	200652
5/15/2020	R	32	One Injected	Tank1/Tank 2	5.3	2.3	120020
5/20/2020	R	32	One Injected	Tank1/Tank 2	15.5	10.2	213067
5/21/2020	R	32	One Injected	Tank 3	10.2	5.1	102241
6/1/2020	R	32	One Injected	Tank 3	5.1	2.1	60740
6/4/2020	Beef 24	7.67	One Irrigated	Tank 3	14.8	12.4	48658
6/7/2020	Beef 24	7.67	One Irrigated	Tank 3	12.4	12.2	4688
7/22/2020	Beef 24	7.67	One Irrigated	Tank 3	12.2	8	84548
7/24/2020	Beef 24	7.67	One Irrigated	Tank 3	8	5.4	52219
7/27/2020	Beef 24	7.67	One Irrigated	Tank 3	5.4	3.5	38671

10/14/2020	R	32	One Injected	Tank 3	19.6	10.9	174083
10/15/2020	R	32	One Injected	Tank 3	17.1	12.6	91337
10/16/2020	R	32	One Injected	Tank 3	12.6	6.9	114188
10/19/2020	R	32	One Injected	Tank 3	6.8	2.5	86219
10/22/2020	R	32	One Injected	Tank 1/Tank2	8.4	5.4	123426
10/23/2020	R	32	One Injected	Tank1/Tank 2	5.4	2.5	117356
3/15/2021	K	53	One Injected	Tank1/Tank 2	10.7	8.3	113,112
3/16/2021	K	53	One Injected	Tank1/Tank 2	8.3	5.1	119258
3/23/2021	K	53	One Injected	Tank1/Tank 2	5.1	1.6	107124

Dairy

Date	Location Field	Acres	Application	Start Depth	Depth from Top	Gallons	Gallons/Acre
3/26/2019	Lake Barn	24	One Injected	2.5'	5'	302500	12604
3/27/2019	Lake Barn	24	One Injected	5' ~	6.5'	181500	7563
3/28/2019	Lake Barn	24	One Injected	6.5' ~	8' ~	181500	7563
2/10/2020	Lake Barn	24	Two Injected	Full	2' ~	242000	10083
2/12/2020	Lake Barn	24	Two Injected	2' ~	4' ~	242000	10083
2/21/2020	Lake Barn	24	Two Injected	4' ~	7' ~	363000	15125
2/24/2020	Lake Barn	24	Two Injected	7' ~	10' ~	363000	15125
2/26/2020	Lake Barn	24	Two Injected	10' ~	14'	484000	20167
3/9/2020	Lake Barn	24	Two Injected	Full	2' ~	242000	10083
3/12/2020	Lake Barn	24	Two Injected	2' ~	5' ~	363000	15125
3/19/2020	Lake Barn	24	Two Injected	5' ~	8' ~	363000	15125
3/26/2020	Lake Barn	24	Two Injected	8' ~	12' ~	484000	20167
3/27/2020	Lake Barn	24	Two Injected	12' ~	14'	242000	10083

Appendix D: Report on the physical properties of 32-0-0 UAN fertilizer. Used for determining weight of nitrogen applied in aqueous fertilizer.

Nutrien
Feeding the Future™

FERTILIZER PRODUCTS

Source: Augusta, GA / Geismar, LA
Alternate Names: Urea-Ammonium Nitrate (UAN) Solution, URAN

page 1 of 1

CHEMICAL DATA	TYPICAL	GUARANTEED
Total Nitrogen, Wt. %		32.0 ± 0.2
Ammonia Nitrate, Wt. %	45.1	42.1 - 47.6
Urea, Wt. %	34.8	32.9 - 37.0
Alkalinity, as Ammonia, Wt. %	0.03	0.01 - 1.05
Inhibitor: ENDCOR, UAN, ppm	60	
Water, Wt. %	20.1	

PHYSICAL DATA	TYPICAL	GUARANTEED
Appearance		Clear with a slight tint
Specific Gravity @ 60°/60°F	1.326	
Viscosity, cps @ 60°F	5.5	
Salting-out temperature, °F	29	
Freezing point, °F	-16	
Equivalent acidity, lbs CaCo$_3$, Equivalent per 100 lbs Product	57.6	

FORMULATION AND HANDLING FACTORS, 60°F	
Pounds/Gallon	11.04
Gallons/Ton	181.2
Pounds/Cubic Feet	82.6
Pounds N/Gallon	3.53
Pounds/Unit N	62.5
Gallons/Unit N	5.66

PLANT FOOD NITROGEN CONTENT	
Total Nitrogen, Wt. %	32.0
Ammoniacal Nitrogen, Wt. %	7.9
Nitrate Nitrogen, Wt. %	7.9
Urea Nitrogen, Wt. %	16.2

DENSITY (POUNDS PER GALLON) AS A FACTOR OF TEMPERATURE						
30°F	40°F	50°F	60°F	70°F	80°F	90°F
11.13	11.11	11.08	11.04	11.01	10.98	10.94

Note: All of the above properties are based on the analysis of a composite sample from a bulk shipment.
Grab samples or individual car samples may fall outside of the specified typical.

Nutrien™

Appendix E: Calibration Report for Optical Dissolved Oxygen sensor from May 6, 2021.

Calibration Worksheet

KOR

Optical DO 18D102138

	UTC Time	Eastern Standard Time
Start Date/Time	5/6/2021 08:38:57 PM	5/6/2021 03:38:57 PM
End Date/Time	5/6/2021 08:39:41 PM	5/6/2021 03:39:41 PM
Previous Calibration Date/Time	3/1/2021 10:25:01 PM	3/1/2021 05:25:01 PM

Sensor Type	Optical DO	Sonde Type	EXO2 Sonde
Sensor SN	18D102138	Sonde SN	18E100393
Sensor Firmware Version	3.0.0	Sonde Firmware Version	1.0.55
Calibration Parameter	ODO % sat	Sonde ID	Sonde 18E100393

✓ QC Score

	Cal Point 1	Cal Point 2	Cal Point 3
Standard	Air Saturated		
Pre Calibration Value	92.20 % sat		
Post Calibration Value	97.20 % sat		
Raw Value (ODO % RAW)	91.26		
Temperature	23.25 ° C		
Additional Input 1 (Baro mmHg)	738.77		
Additional Input 2 (N/A)			
Additional Input 3 (N/A)			
Type	Air-Saturated		
Manufacturer	lab		
Lot Number	lab		
Calibration Point Accepted	YES		
Stability Achieved	YES		

Completed	YES	**Additional Post Calibration Info:**
Applied	YES	Membrane SN: 18C105446
Valid	YES	Membrane Info Last Updated: 04/30/2018 11:29:23
Sensor Removed	NO	ODO Gain: 1.06
Uncalibrated	NO	

Hardware	EXO Desktop
KOR Version	1.0.12
Worksheet Version	1

Appendix F: Summary of the results from model tuning.

Run #	# of Layers	# of Neurons	MSE after 5000 epoch	Avg MSE
Run 4	1	40	Failed at 469	
Run 7	1	40	Failed at 507	
Run 1	1	40	Failed at 255	
Run 2	1	40	Failed at 270	
Run 3	1	40	Failed at 408	
Run 2	1	50	0.000103	
Run 3	1	50	0.000075	0.000081
Run 4	1	50	Failed at 280	
Run 5	1	50	0.000066	
Run 1	1	80	Failed at 356	
Run 2	1	80	Failed at 225	
Run 3	1	80	0.00007	0.000063
Run 4	1	80	0.000058	
Run 5	1	80	0.000058	
Run 6	1	80	0.000066	
Run 8	1	100	0.00008	
Run 9	1	100	0.000091	0.000075
Run 10	1	100	Failed after 199	
Run 6	1	100	0.000053	
Run 1	2	40	0.000084	
Run 2	2	40	Failed at 577	
Run 3	2	40	missed epoch 5000	
Run 1	2	40	0.000093	0.000079
Run 5	2	40	Failed at 255	
Run 6	2	40	0.00006	
Run 7	2	40	failed at 566	
Run 1	2	50	0.000056	
Run 2	2	50	Failed after 286 epoch	
Run 3	2	50	0.000054	
Run 4	2	50	0.000047	
Run 5	2	50	0.000054	
Run 6	2	50	0.000048	0.000051625
Run 1	2	50	Failed after 359 epoch	
Run 2	2	50	0.000053	
Run 3	2	50		
Run 1	2	50	0.000057	
Run 2	2	50	0.000044	
Run 5	2	60	0.000047	
Run 1	2	60	0.000075	
Run 2	2	60	Failed after 476	
Run 3	2	60	Failed at 512	
Run 4	2	60	0.000051	0.00005625
Run 5	2	60	0.000046	
Run 6	2	60	0.000061	
Run 7	2	60	0.000048	
Run 8	2	60	0.000074	
Run 9	2	60	0.000048	
Run 4	2	100	0.00008	
Run 8	2	100	Failed at 297	0.000067
Run 9	2	100	0.00005	
Run 10	2	100	0.000072	

Appendix G: Soil moisture variations measured during the monitoring period.
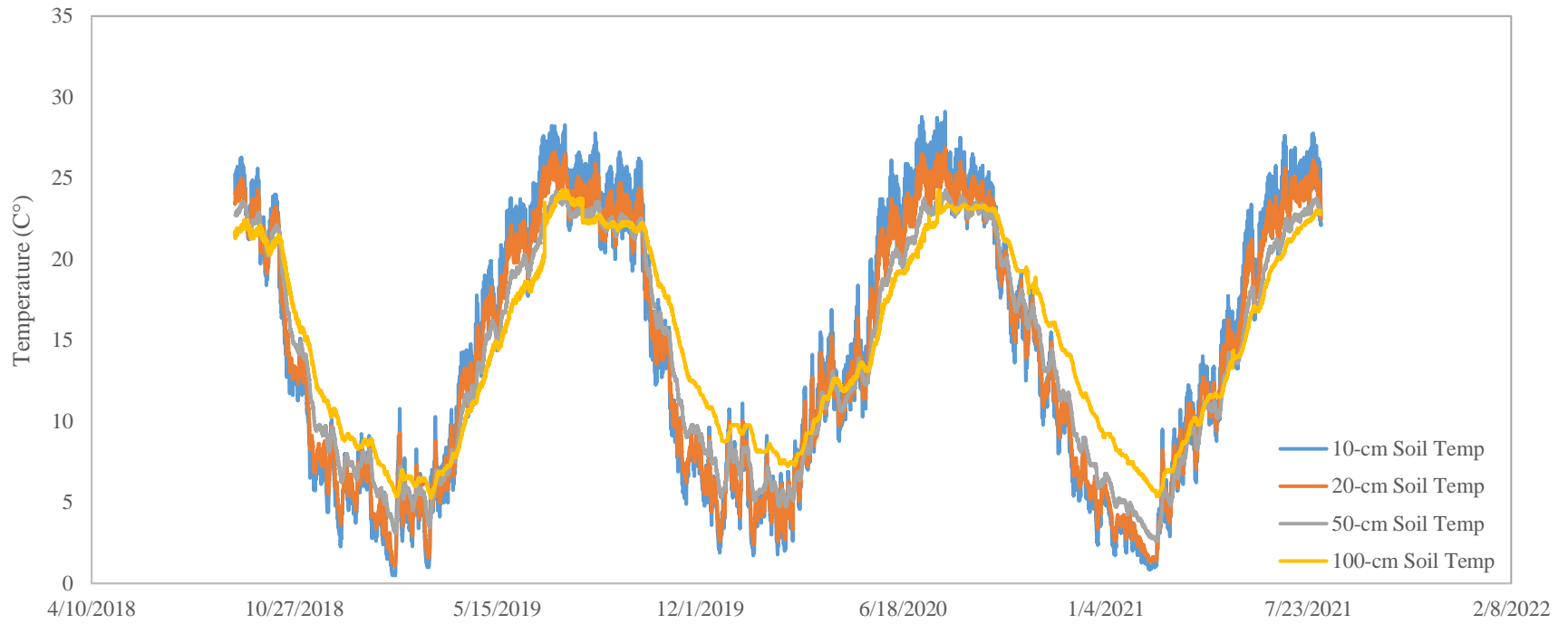
Appendix H: Field Notes

Feb 28, 2020 -1.75ft on wall

          -Deployment started 10:59, swapped 11:20am

May 30, 2020 -18.9in at YSI

          -Deployed 2:25pm

June 30, 2020 -Algae growth has really started

          -Deployed 0383 1:23pm

          -Depth 1.05ft on wall

          -Lowest flow I had seen

          -Removed 1274

July 10th, 2020-Algae growth continued

          -Deployed SUNA about 2pm

          -Depth: Wall 28.3cm

               Center 28.3cm

               YSI 28.3

July 29th, 2020-Deploy YSI 1274 1:30-1:45pm

          -0.975ft on wall

          -Low Flow

August 8th, 2020 -Attempted to deploy bottles for ISCO Sampling but refrigerator
          compartment was about 1/5-1/6 full of water (2-3L). Tubing also fell into
          stream. Not prepared and must repair early next week

August 11th, 2020 -Returned to site to deploy ISCO bottles

-Used small container and shammy to remove water

-Appears to be a drain in bottom of ISCO

-Pulled Tubing up using scuba spool

August 18th, 2020 -Arrived to discover several power failures during the past week

11:35am-1:15pm -Noticed the solar panel was shaded by tree from behind at approximately noon

-Cut back several branches to allow solar view and tilted panel to face more skyward (to midday sun)

-Recovered 6 Samples

-Samples deposited starting with 1 on Aug 19 at 00:00

August 25th, 2020 -ISCO appears to have maintained power for the week

11:45am   -Filled bottle 14 while onsite

Sept 1, 2020   -Swapped YSI yesterday, August 31st about 1:40pm

-Troll handheld computer is dead

-Raining off and on for the last 1.5 days or so

-Downloaded SUNA Data

-Water Level 1.05ft 11:25

-Swapped Bottles

-Snakes in water when I arrived

-Crawfish eating a dead fish

Sept 8, 2020   -ISCO seems to have worked properly; a few samples missing; needs new battery

-Power failure on bottles 3, 5, 7, 9

-12:38pm Downloading Troll Data, approximately 20 minutes, big file

Sept 15, 2020   -Power failure on bottles 3, 7, 11

                 -Center of Channel Depth: 29.5cm

                 -YSI Depth: 29cm

Sept 19, 2020   -Power Failure on bottle 3 (sept 17 00:00)

                 -Between bottles 2 and 4 the distributor became misaligned resulting in
                 bad samples

Sept 26, 2020   -Swapped ISCO bottles 10am

                 -Distributor Error and only samples 1 and 2 are good

Sept 30, 2020   -Swapped YSI about 11 am

                 -Depth Center: 24.4

                 -Depth YSI: 25cm

                 -Depth Wall: 0.8ft

Nov 6, 2020   -Placed YSI in channel for cross-over point at 7:34am

                 -Cross-over point at 7:45am

                 -Time not updated on YSI for time change

Nov 13, 2020   -Removed SUNA for dirty read at 12:35pm

                 -dirty read 0.10mgN/L

                 -clean read 0.06mgN/L

                 -Reference Spectrum updated 13:36

Dec 10, 2020   -Swapped YSI: 1274 going in

                 -Depth: meter stick center 37cm

                 -crossover point 1:30

Jan 5, 2021   -Arrived 8:40am

-Misty and wet

-Center Channel: 55.8cm meter stick

-Depth at YSI: 56cm

-Crossover: 9-9:15am

-38°F feels like 30°F

-fDOM not calibrated

-Downloaded troll 9:15-9:25

-Downloaded SUNA 9:38-9:40

Jan 14, 2021   -Arrived 12:28pm

-Approach from opposite end of culvert

-pool at sensor murky

-obtained grab sample between 12:31 and 12:32

-Forgot filter at lab, filtered at 13:20 once back to lab

-Depth YSI: 44.5cm

-Depth center: 45cm

Jan 26, 2021   -Arrived onsite 10:15

-Water level highest I've seen

-Not comfortable with entering channel while being the only person onsite

-About 2.4 on scale on wall

-Grab sample collected at 10:30

-Very turbid, difficult to filter full sample with one filter, slow drip at end

Feb 2, 2021   -Placed YSI in channel for crossover at 13:05, crossover time 13:15

-Grab sample collected at 13:10

-depth center: 60-61cm

-Depth cage: 59.8-60cm

-downloaded SUNA data 13:40-13:45

-SUNA removed for reference spectrum update 13:50

-Replaced SUNA about 14:45

Feb 10, 2021   -Grab Sample collected 13:20-13:25

-Forecasted to get ice and snow this evening into night

-Tomorrow is supposed to be nasty

-About 30 degrees and is supposed to drop to single digits

Mar 5, 2021   -Swapped YSI about 13:30 local time

-Water level much lower than Monday

-Center of channel 59-59.5cm

-Cage: 58.5-59cm

-Tube/Strainer 23-24cm from the bed

-grab sample 13:30-13:35

Mar 26, 2021   -12:15 grab sample

Apr 5, 2021   -13:39 placed YSI for swap

-14:30 Dirty Read

-SUNA replaced 14:54 edt

-Removed about 14:00

Apr 23, 2021   -Grab Sample 12:25

-Depth Center: 37-37.5cm

-Depth YSI: 37.5cm

May 11, 2021   -12:27 EDT deployed YSI for next interval at 12:30

-Updated the time on sonde because it was 7-8 minutes fast

-Placed in channel 12:36 for next read at 12:45

-Depth Center: 47.5-48cm

-Depth YSI: 47.5cm

-Placed in cage after crossover 12:52

-Deployment stopped 13:06

June 1, 2021   -Grab sample collected 9:12

-39cm center

-38cm YSI

-9:30 EDT crossover point

-SUNA removed from channel between 9:40 and 9:45edt

-Returned to channel about 10:30-11

July 6, 2021   -11:50edt placed YSI on Channel for crossover at 12edt

-SUNA replaced and old YSI removed at 12:48 edt

-Center channel 38.5-39cm

-YSI side 39-39.5cm

-Grab Sample 7.6.21.12.50

August 4, 2021 -Placed YSI in channel 12:50edt

-Cluster of a day, tried deploying NitraLED but the calibration was off, didn't have everything for site specific correction, wiper wasn't installed after calibration so Emma and Vanessa went back to lab

- reference spectrum update on SUNA

-Removed YSI 2:15edt

-Wiper had fallen off

CHAPTER 7. REFERENCES

Acharya, N., Shrivastava, N. A., Panigrahi, B. K., & Mohanty, U. C. (2014). Development of an artificial neural network based multi-model ensemble to estimate the northeast monsoon rainfall over south peninsular India: an application of extreme learning machine. *Climate Dynamics*, *43*(5), 1303-1310. https://doi.org/10.1007/s00382-013-1942-2

Agostinelli, F., Hoffman, M., Sadowski, P., & Baldi, P. (2014). Learning Activation Functions to Improve Deep Neural Networks.

Alexander, R. B., Böhlke, J. K., Boyer, E. W., David, M. B., Harvey, J. W., Mulholland, P. J., . . . Wollheim, W. M. (2009). Dynamic modeling of nitrogen losses in river networks unravels the coupled effects of hydrological and biogeochemical processes. *Biogeochemistry*, *93*(1), 91-116. https://doi.org/10.1007/s10533-008-9274-8

Alexander, R. B., Smith, R. A., Schwarz, G. E., Boyer, E. W., Nolan, J. V., & Brakebill, J. W. (2008). Differences in Phosphorus and Nitrogen Delivery to The Gulf of Mexico from the Mississippi River Basin. *Environmental science & technology*, *42*(3), 822-830. https://doi.org/10.1021/es0716103

Aquilina, L., Ladouche, B., & Dörfliger, N. (2006). Water storage and transfer in the epikarst of karstic systems during high flow periods. *Journal of Hydrology*, *327*(3), 472-485. https://doi.org/10.1016/j.jhydrol.2005.11.054

Arango, C. P., & Tank, J. L. (2008). Land use influences the spatiotemporal controls on nitrification and denitrification in headwater streams. *Journal of the North American Benthological Society*, *27*(1), 90-107. https://doi.org/10.1899/07-024.1

Aubert, A. H., & Breuer, L. (2016). New Seasonal Shift in In-Stream Diurnal Nitrate Cycles Identified by Mining High-Frequency Data. *PloS one*, *11*(4), e0153138. https://doi.org/10.1371/journal.pone.0153138

Bakalowicz, M. (2005). Karst groundwater: a challenge for new resources. *Hydrogeology journal*, *13*(1), 148-160. https://doi.org/10.1007/s10040-004-0402-9

Baker, E. B., & Showers, W. J. (2019). Hysteresis analysis of nitrate dynamics in the Neuse River, NC. *The Science of the total environment*, *652*, 889-899. https://doi.org/10.1016/j.scitotenv.2018.10.254

Banerjee, C., Mukherjee, T., & Pasiliao, E. (2020). Feature representations using the reflected rectified linear unit (RReLU) activation. *Big Data Mining and Analytics*, *3*(2), 102-120. https://doi.org/10.26599/BDMA.2019.9020024

Baran, N., Lepiller, M., & Mouvet, C. (2008). Agricultural diffuse pollution in a chalk aquifer (Trois Fontaines, France): Influence of pesticide properties and hydrodynamic constraints. *Journal of hydrology (Amsterdam)*, *358*(1), 56-69. https://doi.org/10.1016/j.jhydrol.2008.05.031

Barzegar, R., Asghari Moghaddam, A., Adamowski, J., & Ozga-Zielinski, B. (2018). Multi-step water quality forecasting using a boosting ensemble multi-wavelet extreme learning machine model. *Stochastic Environmental Research and Risk Assessment*, *32*(3), 799-813. https://doi.org/10.1007/s00477-017-1394-z

Barzegar, R., Moghaddam, A. A., Deo, R., Fijani, E., & Tziritis, E. (2018). Mapping groundwater contamination risk of multiple aquifers using multi-model ensemble of machine learning algorithms. *Science of The Total Environment*, *621*, 697-712. https://doi.org/https://doi.org/10.1016/j.scitotenv.2017.11.185

Basu, N. B., Destouni, G., Jawitz, J. W., Thompson, S. E., Loukinova, N. V., Darracq, A., . . . Rao, P. S. C. (2010). Nutrient loads exported from managed catchments reveal emergent biogeochemical stationarity. *Geophysical Research Letters*, *37*(23). https://doi.org/https://doi.org/10.1029/2010GL045168

Basu, N. B., Jindal, P., Schilling, K. E., Wolter, C. F., & Takle, E. S. (2012). Evaluation of analytical and numerical approaches for the estimation of groundwater travel time distribution. *Journal of Hydrology*, *475*, 65-73. https://doi.org/https://doi.org/10.1016/j.jhydrol.2012.08.052

Bell, J. E., Palecki, M. A., Baker, C. B., Collins, W. G., Lawrimore, J. H., Leeper, R. D., . . . Diamond, H. J. (2013). U.S. Climate Reference Network Soil Moisture and Temperature Observations. *Journal of Hydrometeorology*, *14*(3), 977-988. https://doi.org/10.1175/JHM-D-12-0146.1

Bernhardt, E. S., Likens, G. E., Hall, R. O., Buso, D. C., Fisher, S. G., Burton, T. M., . . . Lowe, W. H. (2005). Can't See the Forest for the Stream? In-stream Processing and Terrestrial Nitrogen Exports. *BioScience*, *55*(3), 219-230. https://doi.org/10.1641/0006-3568(2005)055[0219:ACSTFF]2.0.CO;2

Bishop, C. M., Bishop, P. N. C. C. M., Hinton, G., & Oxford University, P. (1995). *Neural Networks for Pattern Recognition*. Clarendon Press.

Blaen, P. J., Khamis, K., Lloyd, C., Comer-Warner, S., Ciocca, F., Thomas, R. M., . . . Krause, S. (2017). High-frequency monitoring of catchment nutrient exports reveals highly variable storm event responses and dynamic source zone activation. *Journal of geophysical research. Biogeosciences*, *122*(9), 2265-2281. https://doi.org/10.1002/2017jg003904

Boyer, D. G., & Pasquarell, G. C. (1995). NITRATE CONCENTRATIONS IN KARST SPRINGS IN AN EXTENSWELY GRAZED AREA. *Journal of the American*

Water Resources Association, *31*(4), 729-736. https://doi.org/10.1111/j.1752-1688.1995.tb03397.x

Boyer, D. G., & Pasquarell, G. C. (1996). AGRICULTURAL LAND USE EFFECTS ON NITRATE CONCENTRATIONS IN A MATURE KARST AQUIFER1. *JAWRA Journal of the American Water Resources Association*, *32*(3), 565-573. https://doi.org/https://doi.org/10.1111/j.1752-1688.1996.tb04054.x

Buda, A. R., & DeWalle, D. R. (2009). Dynamics of stream nitrate sources and flow pathways during stormflows on urban, forest and agricultural watersheds in central Pennsylvania, USA. *Hydrological processes*, *23*(23), 3292-3305. https://doi.org/10.1002/hyp.7423

Bunnell, N. L. (2020). QUANTIFYING NITROGEN FATE IN KARST AGROECOSYSTEM STREAMS OF CENTRAL KENTUCKY: DEVELOPMENT AND APPLICATION OF NUMERICAL MODELING AND INSIGHT FROM HIGH-RESOLUTION SENSORS. In.

Burns, D. A., Pellerin, B. A., Miller, M. P., Capel, P., Tesoriero, A. J., & Duncan, J. M. (2019). Monitoring the Riverine Pulse: Applying high-frequency nitrate data to advance integrative understanding of biogeochemical and hydrological processes. *WIREs Water*. https://doi.org/10.1002/wat2.1348

Captum: Model Interpretability for PyTorch. (2021). Retrieved 12/08/2021 from https://captum.ai/

Carey, R. O., Wollheim, W. M., Mulukutla, G. K., & Mineau, M. M. (2014). Characterizing Storm-Event Nitrate Fluxes in a Fifth Order Suburbanizing Watershed Using In Situ Sensors. *Environmental science & technology*, *48*(14), 7756-7765. https://doi.org/10.1021/es500252j

Chen, R.-C., Dewi, C., Huang, S.-W., & Caraka, R. E. (2020). Selecting critical features for data classification based on machine learning methods. *Journal of Big Data*, *7*(1), 52. https://doi.org/10.1186/s40537-020-00327-4

Chen, W., Li, M., Nie, J., Li, D., & Xie, Z. (2021). Experimental study on macropore flow effects in unsaturated soil on subsurface drainage and soil desalination*. *Irrigation and Drainage*. https://doi.org/10.1002/ird.2579

Clare, E. (2019). DECOMPOSING A WATERSHED'S NITRATE SIGNAL USING SPATIAL SAMPLING AND CONTINUOUS SENSOR DATA. In.

Cornell. (2021). *Deep Learning and Neural Networks*. Cornell University. Retrieved April 25, 2021 from https://ecornell.cornell.edu/courses/technology/deep-learning-and-neural-networks/

De Neve, S., Hartmann, R., & Hofman, G. (2003). Temperature effects on N mineralization: Changes in soil solution composition and determination of temperature coefficients by TDR. *European Journal of Soil Science*, *54*, 49-62. https://doi.org/10.1046/j.1365-2389.2003.00521.x

Devry. (2021). *Learn About Machine Learning with PyTorch*. Retrieved April 25, 2021 from https://www.devry.edu/online-programs/courses/machine-learning-with-pytorch.html

Diamond, H. J., Karl, T. R., Palecki, M. A., Baker, C. B., Bell, J. E., Leeper, R. D., . . . Thorne, P. W. (2013). U.S. Climate Reference Network after One Decade of Operations: Status and Assessment. *Bulletin of the American Meteorological Society*, *94*(4), 485-498. https://doi.org/10.1175/BAMS-D-12-00170.1

Donner, S. D., Kucharik, C. J., & Foley, J. A. (2004). Impact of changing land use practices on nitrate export by the Mississippi River: MISSISSIPPI LAND USE AND NITRATE EXPORT. *Global biogeochemical cycles*, *18*(1), n/a. https://doi.org/10.1029/2003GB002093

Doucette, R., & Peterson, E. (2014). Identifying water sources in a karst aquifer using thermal signatures. *Environmental Earth Sciences*, *72*. https://doi.org/10.1007/s12665-014-3387-2

EPA. (2007). *Determination of Inorganic Anions by Ion Chromatography*. Retrieved from https://www.epa.gov/hw-sw846/sw-846-test-method-9056a-determination-inorganic-anions-ion-chromatography

Eriksson, P. (2001). Interaction Effects of Flow Velocity and Oxygen Metabolism on Nitrification and Denitirification in Biofilms on Submerged Macrophytes. *Biogeochemistry*, *55*. https://doi.org/10.1023/A:1010679306361

Ewusi, A., Ahenkorah, I., & Aikins, D. (2021). Modelling of total dissolved solids in water supply systems using regression and supervised machine learning approaches. *Applied water science*, *11*(2), 1-16. https://doi.org/10.1007/s13201-020-01352-7

Feng, Y., Gong, D., Mei, X., & Cui, N. (2016). Estimation of maize evapotranspiration using extreme learning machine and generalized regression neural network on the China Loess Plateau. *Hydrology Research*, *48*(4), 1156-1168. https://doi.org/10.2166/nh.2016.099

Fijani, E., Barzegar, R., Deo, R., Tziritis, E., & Skordas, K. (2019). Design and implementation of a hybrid model based on two-layer decomposition method coupled with extreme learning machines to support real-time environmental monitoring of water quality parameters. *Science of The Total Environment*, *648*, 839-853. https://doi.org/https://doi.org/10.1016/j.scitotenv.2018.08.221

Fleury, P., Plagnes, V., & Bakalowicz, M. (2007). Modelling of the functioning of karst aquifers with a reservoir model: Application to Fontaine de Vaucluse (South of France). *Journal of Hydrology*, *345*(1), 38-49. https://doi.org/https://doi.org/10.1016/j.jhydrol.2007.07.014

Ford, D. (1989). *Karst geomorphology and hydrology*. London ; Boston : Unwin Hyman.

Ford, W., Fox, J., & Pollock, E. (2017). Reducing equifinality using isotopes in a process-based stream nitrogen model highlights the flux of algal nitrogen from agricultural streams. *Water Resources Research*, *53*. https://doi.org/10.1002/2017WR020607

Ford, W., III, Williams, M. R., Young, M. B., King, K. W., & Fischer, E. (2018). Assessing Intra-Event Phosphorus Dynamics in Drainage Water Using Phosphate Stable Oxygen Isotopes. *61*(4). https://doi.org/10.13031/trans.12804

Ford, W. I., Husic, A., Fogle, A., & Taraba, J. (2019). Long-term assessment of nutrient flow pathway dynamics and in-stream fate in a temperate karst agroecosystem watershed. *Hydrological Processes*, *33*(11), 1610-1628. https://doi.org/10.1002/hyp.13427

Gazoni, E., & Clark, C. (2021). *openpyxl - A Python library to read/write Excel 2010 xlsx/xlsm files*. Retrieved 12/08/2021 from https://openpyxl.readthedocs.io/en/stable/

Geonor. (2016). T-200B Series Precipitation Gauge. In (Vol. Rev 10.10).

Germer, K., & Braun, J. (2015). Macropore–Matrix Water Flow Interaction around a Vertical Macropore Embedded in Fine Sand—Laboratory Investigations. *Vadose Zone Journal*, *14*(7). https://doi.org/10.2136/vzj2014.03.0030

Green, C. T., Liao, L., Nolan, B. T., Juckem, P. F., Shope, C. L., Tesoriero, A. J., & Jurgens, B. C. (2018). Regional Variability of Nitrate Fluxes in the Unsaturated Zone and Groundwater, Wisconsin, USA. *Water Resources Research*, *54*(1), 301-322. https://doi.org/https://doi.org/10.1002/2017WR022012

Griffiths, N. A., Tank, J. L., Royer, T. V., Roley, S. S., Rosi-Marshall, E. J., Whiles, M. R., . . . Johnson, L. T. (2013). Agricultural land use alters the seasonality and magnitude of stream metabolism. *Limnology and oceanography*, *58*(4), 1513-1529. https://doi.org/10.4319/lo.2013.58.4.1513

Guntiñas, M. E., Leirós, M. C., Trasar-Cepeda, C., & Gil-Sotres, F. (2012). Effects of moisture and temperature on net soil nitrogen mineralization: A laboratory study. *European Journal of Soil Biology*, *48*, 73-80. https://doi.org/https://doi.org/10.1016/j.ejsobi.2011.07.015

Hansen, A., & Singh, A. (2018). High-Frequency Sensor Data Reveal Across-Scale Nitrate Dynamics in Response to Hydrology and Biogeochemistry in Intensively Managed Agricultural Basins. *Journal of geophysical research. Biogeosciences*, *123*(7), 2168-2182. https://doi.org/10.1029/2017JG004310

Hartmann, A. (2017). Experiences in calibrating and evaluating lumped karst hydrological models.

Hartmann, A., Barberá, J. A., & Andreo, B. (2017). On the value of water quality data and informative flow states in karst modelling. *Hydrol. Earth Syst. Sci.*, *21*(12), 5971-5985. https://doi.org/10.5194/hess-21-5971-2017

Hartmann, A., Goldscheider, N., Wagener, T., Lange, J., & Weiler, M. (2014). Karst water resources in a changing world: Review of hydrological modeling approaches: KARST WATER RESOURCES PREDICTION. *Reviews of geophysics (1985)*, *52*(3), 218-242. https://doi.org/10.1002/2013RG000443

Hartmann, A., Wagener, T., Rimmer, A., Lange, J., Brielmann, H., & Weiler, M. (2013). Testing the realism of model structures to identify karst system processes using water quality and quantity signatures. *Water Resources Research*, *49*(6), 3345-3358. https://doi.org/10.1002/wrcr.20229

Heffernan, J. B., Cohen, M. J., Frazer, T. K., Thomas, R. G., Rayfield, T. J., Gulley, J., . . . Graham, W. D. (2010). Hydrologic and biotic influences on nitrate removal in a subtropical spring-fed river. *Limnology and Oceanography*, *55*(1), 249-263. https://doi.org/https://doi.org/10.4319/lo.2010.55.1.0249

Hinton, G. E., Srivastava, N., Krizhevsky, A., Sutskever, I., & Salakhutdinov, R. R. (2012). Improving neural networks by preventing co-adaptation of feature detectors.

Huang, G., Huang, G.-B., Song, S., & You, K. (2015). Trends in extreme learning machines: A review. *Neural Networks*, *61*, 32-48. https://doi.org/https://doi.org/10.1016/j.neunet.2014.10.001

Huang, G., Zhou, H., Ding, X., & Zhang, R. (2012). Extreme Learning Machine for Regression and Multiclass Classification. *IEEE Transactions on Systems, Man, and Cybernetics, Part B (Cybernetics)*, *42*(2), 513-529. https://doi.org/10.1109/TSMCB.2011.2168604

Hunter, J., Dale, D., Firing, E., & Droettboom, M. (2021). *Matplotlib: Visualization with Python*. Retrieved 12/08/2021 from https://matplotlib.org/

Husic, A., Fox, J., Adams, E., Ford, W., Agouridis, C., Currens, J., & Backus, J. (2019). Nitrate Pathways, Processes, and Timing in an Agricultural Karst System:

Development and Application of a Numerical Model. *Water Resources Research*, *55*(3), 2079-2103. https://doi.org/10.1029/2018WR023703

Igbal, M. Z., & Krothe, N. C. (1995). Infiltration mechanisms related to agricultural waste transport through the soil mantle to karst aquifers of southern Indiana, USA. *Journal of Hydrology*, *164*(1), 171-192. https://doi.org/https://doi.org/10.1016/0022-1694(94)02573-T

Incorporated, Y. (2014). Exo User Manual-Advanced Water Quality Monitoring Platform. In (Vol. Revision D): Xylem Inc.

Jackson, L., & Polk, J. S. (2020). Seasonal δ13CDIC sourcing and geochemical flux in telogenetic epikarst of south-central Kentucky. *Earth surface processes and landforms*, *45*(4), 785-799. https://doi.org/10.1002/esp.4768

Jensen, A. K., & Ford, W. I. (2019). Quantifying Nitrate Dynamics of a Confluence Floodplain Wetland in a Disturbed Appalachian Watershed: High-Resolution Sensing and Modeling. *Transactions of the ASABE*, *62*(6), 1545-1565. https://doi.org/10.13031/trans.13278

Jin, X., Xu, C., Feng, J., Wei, Y., Xiong, J., & Yan, S. (2015). Deep Learning with S-shaped Rectified Linear Activation Units.

Johnson, H. M., & Stets, E. G. (2020). Nitrate in Streams During Winter Low-Flow Conditions as an Indicator of Legacy Nitrate. *Water resources research*, *56*(11), n/a. https://doi.org/10.1029/2019WR026996

Jones, W. K. (2013). Physical Structure of the Epikarst. *Acta Carsologica*, *42*(2-3). https://doi.org/10.3986/ac.v42i2-3.672

Katz, B. G., White, W. B., Culver, D. C., & Pipan, T. (2019). Chapter 91 - Nitrate contamination in karst groundwater. In *Encyclopedia of Caves (Third Edition)* (pp. 756-760). Academic Press. https://doi.org/https://doi.org/10.1016/B978-0-12-814124-3.00091-1

Kennedy, C. D., Bataille, C., Liu, Z., Ale, S., VanDeVelde, J., Roswell, C. R., . . . Bowen, G. J. (2012). Dynamics of nitrate and chloride during storm events in agricultural catchments with different subsurface drainage intensity (Indiana, USA). *Journal of Hydrology*, *466-467*, 1-10. https://doi.org/https://doi.org/10.1016/j.jhydrol.2012.05.002

King, K., Williams, M., Macrae, M., Fausey, N. R., Frankenberger, J., Smith, D., . . . Brown, L. (2015). Phosphorus Transport in Agricultural Subsurface Drainage: A Review. *Journal of Environmental Quality*, *44*. https://doi.org/10.2134/jeq2014.04.0163

Klaus, J., Zehe, E., Elsner, M., Külls, C., & McDonnell, J. J. (2013). Macropore flow of old water revisited: experimental insights from a tile-drained hillslope. *Hydrol. Earth Syst. Sci.*, *17*(1), 103-118. https://doi.org/10.5194/hess-17-103-2013

Kogovšek, J., & Petrič, M. (2012). Characterization of the vadose flow and its influence on the functioning of karst springs: Case study of the karst system near Postojna, Slovenia. *Acta carsologica*, *41*(1). https://doi.org/10.3986/ac.v41i1.51

Kunz, J. V., Hensley, R., Brase, L., Borchardt, D., & Rode, M. (2017). High frequency measurements of reach scale nitrogen uptake in a fourth order river with contrasting hydromorphology and variable water chemistry (Weiße Elster, Germany). *Water Resources Research*, *53*(1), 328-343. https://doi.org/https://doi.org/10.1002/2016WR019355

Kurylyk, B. L., Irvine, D. J., Carey, S. K., Briggs, M. A., Werkema, D. D., & Bonham, M. (2017). Heat as a groundwater tracer in shallow and deep heterogeneous media: Analytical solution, spreadsheet tool, and field applications. *Hydrological Processes*, *31*(14), 2648-2661. https://doi.org/10.1002/hyp.11216

Körner, S., & Vermaat, J. E. (1998). The relative importance of Lemna gibba L., bacteria and algae for the nitrogen and phosphorus removal in duckweed-covered domestic wastewater. *Water Research*, *32*(12), 3651-3661. https://doi.org/https://doi.org/10.1016/S0043-1354(98)00166-3

Lai, J., Wang, X., Li, R., Song, Y., & Lei, L. (2020). BD-ELM: A Regularized Extreme Learning Machine Using Biased DropConnect and Biased Dropout. *Mathematical Problems in Engineering*, *2020*, 3604579. https://doi.org/10.1155/2020/3604579

Lary, D. J., Alavi, A. H., Gandomi, A. H., & Walker, A. L. (2016). Machine learning in geosciences and remote sensing. *Geoscience Frontiers*, *7*(1), 3-10. https://doi.org/https://doi.org/10.1016/j.gsf.2015.07.003

Li, Y., Chen, B.-M., Wang, Z.-G., & Peng, S.-L. (2011). Effects of temperature change on water discharge, and sediment and nutrient loading in the lower Pearl River basin based on SWAT modelling. *Hydrological Sciences Journal*, *56*(1), 68-83. https://doi.org/10.1080/02626667.2010.538396

Liu, W., Birgand, F., Tian, S., & Chen, C. (2021). Event-scale hysteresis metrics to reveal processes and mechanisms controlling constituent export from watersheds: A review☆. *Water Research*, *200*, 117254. https://doi.org/https://doi.org/10.1016/j.watres.2021.117254

Liu, Z., Li, Q., Sun, H., & Wang, J. (2007). Seasonal, diurnal and storm-scale hydrochemical variations of typical epikarst springs in subtropical karst areas of SW China: Soil CO2 and dilution effects. *Journal of Hydrology*, *337*(1), 207-223. https://doi.org/https://doi.org/10.1016/j.jhydrol.2007.01.034

MacIntyre, G., Plache, B., Lewis, M. R., Andrea, J., Feener, S., McLean, S. D., . . . Jannasch, H. W. (2009). ISUS/SUNA nitrate measurements in networked ocean observing systems. In (pp. 1-7): IEEE.

Mahoney, D. T., Fox, J. F., & Al Aamery, N. (2018). Watershed erosion modeling using the probability of sediment connectivity in a gently rolling system. *Journal of Hydrology*, *561*, 862-883. https://doi.org/https://doi.org/10.1016/j.jhydrol.2018.04.034

Maryland. (2021). *Deep Learning with Python and PyTorch*. University of Maryland. Retrieved April 25, 2021 from https://umd.uloop.com/online-courses/view.php/1366833689/Deep-Learning-with-Python-and-PyTorch

McCuen, R. H., Knight, Z., & Cutter, A. G. (2006). Evaluation of the Nash–Sutcliffe Efficiency Index. *Journal of hydrologic engineering*, *11*(6), 597-602. https://doi.org/10.1061/(ASCE)1084-0699(2006)11:6(597)

Mehdi, B., Schürz, C., Grath, B., & Schulz, K. (2021). Storm event impacts on in-stream nitrate concentration and discharge dynamics: A comparison of high resolution in-situ measured data with model simulations. *Science of The Total Environment*, *755*, 143406. https://doi.org/https://doi.org/10.1016/j.scitotenv.2020.143406

Meng, L., Ding, W., & Cai, Z. (2005). Long-term application of organic manure and nitrogen fertilizer on N2O emissions, soil quality and crop production in a sandy loam soil. *Soil Biology and Biochemistry*, *37*(11), 2037-2045. https://doi.org/https://doi.org/10.1016/j.soilbio.2005.03.007

Miche, Y., van Heeswijk, M., Bas, P., Simula, O., & Lendasse, A. (2011). TROP-ELM: A double-regularized ELM using LARS and Tikhonov regularization. *Neurocomputing*, *74*(16), 2413-2421. https://doi.org/https://doi.org/10.1016/j.neucom.2010.12.042

Miller, K. S., & Geisseler, D. (2018). Temperature sensitivity of nitrogen mineralization in agricultural soils. *Biology and Fertility of Soils*, *54*(7), 853-860. https://doi.org/10.1007/s00374-018-1309-2

Moreido, V., Gartsman, B., Solomatine, D. P., & Suchilina, Z. (2021). How Well Can Machine Learning Models Perform without Hydrologists? Application of Rational Feature Selection to Improve Hydrological Forecasting. *Water*, *13*(12). https://doi.org/10.3390/w13121696

MRCC. (2021). *Sub-Daily Data Between Two DatesLEXINGTON BLUEGRASS AP (KY)93820*

Mulholland, P. J., Helton, A. M., Poole, G. C., Hall, R. O., Hamilton, S. K., Peterson, B. J., . . . Thomas, S. M. (2008). Stream denitrification across biomes and its response to anthropogenic nitrate loading. *Nature*, *452*(7184), 202-205. https://doi.org/10.1038/nature06686

N. Moriasi, D., G. Arnold, J., W. Van Liew, M., L. Bingner, R., D. Harmel, R., & L. Veith, T. (2007). Model Evaluation Guidelines for Systematic Quantification of Accuracy in Watershed Simulations. *Transactions of the ASABE*, *50*(3), 885-900. https://doi.org/https://doi.org/10.13031/2013.23153

N. Moriasi, D., W. Gitau, M., Pai, N., & Daggupati, P. (2015). Hydrologic and Water Quality Models: Performance Measures and Evaluation Criteria. *Transactions of the ASABE*, *58*(6), 1763-1785. https://doi.org/https://doi.org/10.13031/trans.58.10715

NAE. (2017). *14 Grand Challenges for Engineering in the 21st Century*. E. The National Academies of Sciences, and Medicine. http://www.engineeringchallenges.org/challenges.aspx

NOAA. (2021a). *Instruments*. Retrieved May 5, 2021 from https://www.ncdc.noaa.gov/crn/instruments.html

NOAA. (2021b, Feb 26, 2021). *What is a dead zone?* Retrieved March 3, 2021 from https://oceanservice.noaa.gov/facts/deadzone.html

NumPy: The fundamental package for scientific computing with Python. (2005). Retrieved 12/08/2021 from https://numpy.org/about/

Ollivier, C., Mazzilli, N., Olioso, A., Chalikakis, K., Carrière, S. D., Danquigny, C., & Emblanch, C. (2020). Karst recharge-discharge semi distributed model to assess spatial variability of flows. *Science of The Total Environment*, *703*, 134368. https://doi.org/https://doi.org/10.1016/j.scitotenv.2019.134368

Opsahl, S. P., Musgrove, M., & Slattery, R. N. (2017). New insights into nitrate dynamics in a karst groundwater system gained from in situ high-frequency optical sensor measurements. *Journal of Hydrology*, *546*, 179-188. https://doi.org/10.1016/j.jhydrol.2016.12.038

pandas. (2021). Retrieved 12/8/2021 from https://pandas.pydata.org/

Pellerin, B., Saraceno, J., Shanley, J., Sebestyen, S., Aiken, G., Wollheim, W., & Bergamaschi, B. (2012). Taking the pulse of snowmelt: In situ sensors reveal seasonal, event and diurnal patterns of nitrate and dissolved organic matter variability in an upland forest stream. *Biogeochemistry*, *108*, 183-198. https://doi.org/10.1007/s10533-011-9589-8

Pellerin, B. A., Bergamaschi, B. A., Downing, B. D., Saraceno, J. F., Garrett, J. D., & Olsen, L. D. (2013). Optical Techniques for the Determination of Nitrate in Environmental Waters: Guidelines for Instrument Selection, Operation, Deployment, Maintenance, Quality Assurance, and Data Reporting. In. USGS Techniques and Methods 1-D5 USGS.

Pellerin, B. A., Bergamaschi, B. A., Gilliom, R. J., Crawford, C. G., Saraceno, J., Frederick, C. P., . . . Murphy, J. C. (2014). Mississippi River Nitrate Loads from High Frequency Sensor Measurements and Regression-Based Load Estimation. *Environmental science & technology*, *48*(21), 12612-12619. https://doi.org/10.1021/es504029c

Peterson, B., Bahr, M., & Kling, G. (1997). A tracer investigation of nitrogen cycling in a pristine tundra river. *Canadian Journal of Fisheries and Aquatic Sciences*, *54*, 2361-2367. https://doi.org/10.1139/f97-142

Prasad, R., Deo, R. C., Li, Y., & Maraseni, T. (2018). Soil moisture forecasting by a hybrid machine learning technique: ELM integrated with ensemble empirical mode decomposition. *Geoderma*, *330*, 136-161. https://doi.org/https://doi.org/10.1016/j.geoderma.2018.05.035

PyTorch: End to end machine learning framework. (2021). Retrieved 12/08/2021 from https://pytorch.org/features/

Qu, B. Y., Lang, B. F., Liang, J. J., Qin, A. K., & Crisalle, O. D. (2016). Two-hidden-layer extreme learning machine for regression and classification. *Neurocomputing*, *175*, 826-834. https://doi.org/https://doi.org/10.1016/j.neucom.2015.11.009

Radcliff, C., Ford, W. I., Nazari, S., & Shepard, C. (2021). Impact of water source dynamics on dissolved reactive phosphorus loadings in heterogenous karst agroecosystems with phosphatic limestones. *Hydrological processes*, *35*(11), n/a. https://doi.org/10.1002/hyp.14422

Ransom, K. M., Nolan, B. T., Stackelberg, P. E., Belitz, K., & Fram, M. S. (2021). Machine learning predictions of nitrate in groundwater used for drinking supply in the conterminous United States. *Science of The Total Environment*, 151065. https://doi.org/https://doi.org/10.1016/j.scitotenv.2021.151065

Ravinesh, C. D., & Mehmet, S. (2016). An extreme learning machine model for the simulation of monthly mean streamflow water level in eastern Queensland. *Environmental monitoring and assessment*, *188*(2), 1. https://doi.org/10.1007/s10661-016-5094-9

Reed, T. M., Todd McFarland, J., Fryar, A. E., Fogle, A. W., & Taraba, J. L. (2010). Sediment discharges during storm flow from proximal urban and rural karst springs, central Kentucky, USA. *Journal of Hydrology*, *383*(3), 280-290. https://doi.org/https://doi.org/10.1016/j.jhydrol.2009.12.043

Rezaie-Balf, M., & Kisi, O. (2017). New formulation for forecasting streamflow: evolutionary polynomial regression vs. extreme learning machine. *Hydrology Research*, *49*(3), 939-953. https://doi.org/10.2166/nh.2017.283

Robert, J. D., & Rutger, R. (2008). Spreading Dead Zones and Consequences for Marine Ecosystems. *Science (American Association for the Advancement of Science)*, *321*(5891), 926-929. https://doi.org/10.1126/science.1156401

Robertson, D. M., & Saad, D. A. (2021). Nitrogen and Phosphorus Sources and Delivery from the Mississippi/Atchafalaya River Basin: An Update Using 2012 SPARROW Models. *JAWRA Journal of the American Water Resources Association*, *57*(3), 406-429. https://doi.org/https://doi.org/10.1111/1752-1688.12905

Rode, M., Wade, A. J., Cohen, M. J., Hensley, R. T., Bowes, M. J., Kirchner, J. W., . . . Jomaa, S. (2016). Sensors in the Stream: The High-Frequency Wave of the Present. *Environmental Science & Technology*, *50*(19), 10297-10307. https://doi.org/10.1021/acs.est.6b02155

Roushangar, K., Alizadeh, F., & Nourani, V. (2017). Improving capability of conceptual modeling of watershed rainfall–runoff using hybrid wavelet-extreme learning machine approach. *Journal of Hydroinformatics*, *20*(1), 69-87. https://doi.org/10.2166/hydro.2017.011

Rusjan, S., Brilly, M., & Mikoš, M. (2008). Flushing of nitrate from a forested watershed: An insight into hydrological nitrate mobilization mechanisms through seasonal high-frequency stream nitrate dynamics. *Journal of hydrology (Amsterdam)*, *354*(1), 187-202. https://doi.org/10.1016/j.jhydrol.2008.03.009

Russo, D., Laufer, A., Shapira, R. H., & Kurtzman, D. (2013). Assessment of solute fluxes beneath an orchard irrigated with treated sewage water: A numerical study. *Water Resources Research*, *49*(2), 657-674. https://doi.org/https://doi.org/10.1002/wrcr.20085

Salerno, F., & Tartari, G. (2009). A coupled approach of surface hydrological modelling and Wavelet Analysis for understanding the baseflow components of river discharge in karst environments. *Journal of Hydrology*, *376*(1), 295-306. https://doi.org/https://doi.org/10.1016/j.jhydrol.2009.07.042

Salim, H., & Ozgur, K. (2017). Extreme learning machines: a new approach for modeling dissolved oxygen (DO) concentration with and without water quality variables as

predictors. *Environmental science and pollution research international*, *24*(20), 16702. https://doi.org/10.1007/s11356-017-9283-z

Scientific, S.-B. (2019). *UCI 2.0.3*. Retrieved May 4, 2021 from https://www.seabird.com/static/list-items/uci-2-0-3-en.jsp

scikit-learn: Machine Learning in Python. (2019). Retrieved 12/08/2021 from https://scikit-learn.org/stable/

Sebilo, M., Mayer, B., Nicolardot, B., Pinay, G., & Mariotti, A. (2013). Long-term fate of nitrate fertilizer in agricultural soils. *Proceedings of the National Academy of Sciences*, *110*(45), 18185. https://doi.org/10.1073/pnas.1305372110

Seybold, E., Gold, A. J., Inamdar, S. P., Adair, C., Bowden, W. B., Vaughan, M. C. H., . . . Schroth, A. W. (2019). Influence of land use and hydrologic variability on seasonal dissolved organic carbon and nitrate export: insights from a multi-year regional analysis for the northeastern USA. *Biogeochemistry*, *146*(1), 31-49. https://doi.org/10.1007/s10533-019-00609-x

Shen, C. (2018). A Transdisciplinary Review of Deep Learning Research and Its Relevance for Water Resources Scientists. *Water Resources Research*, *54*(11), 8558-8593. https://doi.org/https://doi.org/10.1029/2018WR022643

Snyder, L., Potter, J. D., & McDowell, W. H. (2018). An Evaluation of Nitrate, fDOM, and Turbidity Sensors in New Hampshire Streams. *Water Resources Research*, *54*(3), 2466-2479. https://doi.org/https://doi.org/10.1002/2017WR020678

Soylu, D. (2021). *CS224N: PyTorch Tutorial (Winter '21)*. Stanford University. Retrieved April 25, 2021 from http://web.stanford.edu/class/cs224n/materials/CS224N_PyTorch_Tutorial.html

Staff, S. S. (2005). *Irrigation Guide*. Natural Resources Conservation Service: USDA Retrieved from https://www.nrcs.usda.gov/Internet/FSE_DOCUMENTS/nrcs141p2_017640.pdf

Steppa, C., & Holch, T. L. (2019). HexagDLy—Processing hexagonally sampled data with CNNs in PyTorch. *SoftwareX*, *9*, 193-198. https://doi.org/10.1016/j.softx.2019.02.010

Stevens. (2019). HydraProbe: Reliable Soil Insight. In.

Sundararajan, M., Taly, A., & Yan, Q. (2017). Axiomatic Attribution for Deep Networks.

Tian, S., Youssef, M., Richards, R., Liu, J., Baker, D., & Liu, Y. (2015). Different seasonality of nitrate export from an agricultural watershed and an urbanized watershed in Midwestern USA.

torch.nn.Module. (2019). Retrieved 12/08/2021 from https://pytorch.org/docs/stable/generated/torch.nn.Module.html

Tritz, S., Guinot, V., & Jourde, H. (2011). Modelling the behaviour of a karst system catchment using non-linear hysteretic conceptual model. *Journal of Hydrology*, *397*(3-4), 250-262. https://doi.org/10.1016/j.jhydrol.2010.12.001

Tzoraki, O., & Nikolaidis, N. P. (2007). A generalized framework for modeling the hydrologic and biogeochemical response of a Mediterranean temporary river basin. *Journal of Hydrology*, *346*(3), 112-121. https://doi.org/https://doi.org/10.1016/j.jhydrol.2007.08.025

van Beynen, P. E. (2011). *Karst Management* (1st ed. 2011. ed.). Springer Netherlands. https://doi.org/10.1007/978-94-007-1207-2

Wang, F., Chen, H., Lian, J., Fu, Z., & Nie, Y. (2018). Preferential Flow in Different Soil Architectures of a Small Karst Catchment. *Vadose Zone Journal*, *17*(1), 180107. https://doi.org/https://doi.org/10.2136/vzj2018.05.0107

Weary, D., & Doctor, D. (2014). Karst in the United States: A Digital Map Compilation and Database. https://doi.org/10.3133/ofr20141156

Webster, J., Mulholland, P., Tank, J., Valett, H., Dodds, W., Peterson, B., . . . Wollheim, W. (2003). Factors Affecting Ammonium Uptake in Streams—An Inter Biome Perspective. *Freshwater Biology*, *48*, 1329-1352. https://doi.org/10.1046/j.1365-2427.2003.01094.x

White, W. B. (2002). Karst hydrology: recent developments and open questions. *Engineering Geology*, *65*(2), 85-105. https://doi.org/https://doi.org/10.1016/S0013-7952(01)00116-8

Williams, P. W. (1983). *The role of the subcutaneous zone in karst hydrology*. Elsevier Scientific Publishing Company.

Wunsch, A., Liesch, T., Cinkus, G., Ravbar, N., Chen, Z., Mazzilli, N., . . . Goldscheider, N. (2021). Karst spring discharge modeling based on deep learning using spatially distributed input data. *Hydrol. Earth Syst. Sci. Discuss.*, *2021*, 1-26. https://doi.org/10.5194/hess-2021-403

Yang, P., Wang, Y., Wu, X., Chang, L., Ham, B., Song, L., & Groves, C. (2020). Nitrate sources and biogeochemical processes in karst underground rivers impacted by

different anthropogenic input characteristics. *Environmental Pollution*, *265*, 114835. https://doi.org/https://doi.org/10.1016/j.envpol.2020.114835

Yang, S., Wang, Y., Liu, R., Zhang, A., & Yang, Z. (2017). Effect of Nitrate Leaching Caused by Swine Manure Application in Fields of the Yellow River Irrigation Zone of Ningxia, China. *Scientific Reports*, *7*(1), 13693. https://doi.org/10.1038/s41598-017-12953-9

Yaseen, Z. M., Sulaiman, S. O., Deo, R. C., & Chau, K.-W. (2019). An enhanced extreme learning machine model for river flow forecasting: State-of-the-art, practical applications in water resource engineering area and future research direction. *Journal of Hydrology*, *569*, 387-408. https://doi.org/https://doi.org/10.1016/j.jhydrol.2018.11.069

Yevenes, M. A., & Mannaerts, C. M. (2011). Seasonal and land use impacts on the nitrate budget and export of a mesoscale catchment in Southern Portugal. *Agricultural Water Management*, *102*(1), 54-65. https://doi.org/https://doi.org/10.1016/j.agwat.2011.10.006

Ying, X. (2019). An Overview of Overfitting and its Solutions. *Journal of Physics: Conference Series*, *1168*, 022022. https://doi.org/10.1088/1742-6596/1168/2/022022

Yue, F.-J., Waldron, S., Li, S.-L., Wang, Z.-J., Zeng, J., Xu, S., . . . Oliver, D. M. (2019). Land use interacts with changes in catchment hydrology to generate chronic nitrate pollution in karst waters and strong seasonality in excess nitrate export. *Science of The Total Environment*, *696*, 134062. https://doi.org/https://doi.org/10.1016/j.scitotenv.2019.134062

Zhang, J. B., Zhu, T. B., Cai, Z. C., Qin, S. W., & Müller, C. (2012). Effects of long-term repeated mineral and organic fertilizer applications on soil nitrogen transformations. *European Journal of Soil Science*, *63*(1), 75-85. https://doi.org/https://doi.org/10.1111/j.1365-2389.2011.01410.x

Zhang, Z., Chen, X., Cheng, Q., Li, S., Yue, F., Peng, T., . . . Soulsby, C. (2020). Coupled hydrological and biogeochemical modelling of nitrogen transport in the karst critical zone. *Science of The Total Environment*, *732*, 138902. https://doi.org/https://doi.org/10.1016/j.scitotenv.2020.138902

Zhao, W. L., Gentine, P., Reichstein, M., Zhang, Y., Zhou, S., Wen, Y., . . . Qiu, G. Y. (2019). Physics-Constrained Machine Learning of Evapotranspiration. *Geophysical Research Letters*, *46*(24), 14496-14507. https://doi.org/https://doi.org/10.1029/2019GL085291

Zhu, B., Feng, Y., Gong, D., Jiang, S., Zhao, L., & Cui, N. (2020). Hybrid particle swarm optimization with extreme learning machine for daily reference

evapotranspiration prediction from limited climatic data. *Computers and Electronics in Agriculture*, *173*, 105430. https://doi.org/https://doi.org/10.1016/j.compag.2020.105430

Zhu, B., Wang, T., Kuang, F., Luo, Z., Tang, J., & Xu, T. (2009). Measurements of Nitrate Leaching from a Hillslope Cropland in the Central Sichuan Basin, China. *Soil Science Society of America journal*, *73*(4), 1419-1426. https://doi.org/10.2136/sssaj2008.0259

CHAPTER 8. Vita

1. University of Kentucky – Bachelor of Science
   Major: Biosystems and Agricultural Engineering
2. Graduate Research Assistant – University of Kentucky
3. Timothy A. McGill Jr.